Application of single-wavelength radiation thermometry and high-speed laser polarimetry to thermophysical property measurements on pulse-heated metals

Dissertation

by

Dipl.-Ing. Konstantinos Boboridis

carried out at the

NATIONAL INSTITUTE OF STANDARDS AND TECHNOLOGY
GAITHERSBURG, MARYLAND 20899, USA

in cooperation with the

INSTITUT FÜR EXPERIMENTALPHYSIK
DER TECHNISCHEN UNIVERSITÄT GRAZ, AUSTRIA

MAY 2001

dedicated to the memory of

Ared Cezairliyan (1934-1997)

SYNOPSIS

A microsecond-resolution technique was used to measure the heat of fusion, specific heat capacity, and electrical resistivity of niobium and titanium in the temperature ranges 1600 to 3200 K and 1500 to 2200 K, respectively. The method was based on rapid resistive self-heating of a wire-shaped specimen by a large current pulse from a capacitor-discharge system. Measured quantities were the current through the specimen, the voltage across the specimen, the radiance temperature of the specimen at 656.3 nm, and its normal spectral emittance at 677 nm, as functions of time. Radiance temperature was obtained by means of single-wavelength radiation thermometry. Normal spectral emittance was measured using high-speed laser polarimetry. Combined, radiance temperature and normal spectral emittance yielded the thermodynamic temperature of the specimen at each instance.

KURZFASSUNG

In einem Entladungskreis mit kapazitiver Energiespeicherung werden drahtförmige, elektrisch leitende Proben durch ohmsche Pulsheizung schnell erhitzt. Der Strom durch die Probe, der Spannungsabfall an der Probe, ihre Strahlungstemperatur bei 656.3 nm und ihr normaler spektraler Emissionskoeffizient bei 677 nm werden zeitaufgelöst gemessen. Daraus bestimmt man die Schmelzwärme, die spezifische Wärmekapazität bei konstantem Druck und den spezifischen elektrischen Widerstand der Proben. In der vorliegenden Dissertation werden Untersuchungen zur Bestimmung thermophysikalischer Daten von Niob und Titan im Temperaturbereich 1600 bis 3200 K, bzw. 1500 bis 2200 K beschrieben. Die Strahlungstemperatur der Proben wurde mit einem Einwellenlängen-Pyrometer bestimmt. Der normale spektrale Emissionskoeffizient wurde mittels Photopolarimetrie gemessen. Diese beiden Größen zusammen ergeben die wahre Temperatur der Proben.

Table of contents

1 INTRODUCTION

Pulse-heating techniques for the determination of thermophysical properties of metals and alloys have been in use for many years. Compared to steady-state or quasi-steady-state techniques, they have a number of advantages to offer, particularly at higher temperatures and in the liquid state. This is where problems such as increased heat transfer, chemical reactions, evaporation, loss of mechanical strength, etc. may have a significant impact on the quality of the acquired data. These limitations can be overcome when the measurement duration is short enough.

The quality of the measured thermophysical properties strongly depends on the accuracy of the temperature measurement. Radiation thermometry, also known as pyrometry, has been the temperature measurement technique of choice when high temperatures and high heating rates are involved, because of its contactless character and fast response time. Radiation thermometry relates the radiance (§2.1.1) emitted by a specimen to the temperature of a blackbody that would emit the same amount of radiance. This is called the radiance temperature of the specimen and will be different than the true (thermodynamic) temperature if the specimen is not a blackbody. The two temperatures are related through the emittance of the specimen. If this quantity is unknown an error is introduced in the temperature measurement, which generally increases with increasing temperature.

The most direct way to solve this problem is to have the specimen itself incorporate a blackbody cavity. A radiation thermometer looking at this cavity will measure the true specimen temperature, as follows from the definition of radiance temperature. This has been done in the past [1, 2][1], and is widely considered the most accurate method. Limitations of this approach are its inapplicability to specimens that are too small or inaccessible for the inclusion of a blackbody cavity and also to liquid materials.

Another approach is to combine the radiance temperature measurement with emittance data from literature. Nevertheless, such data for many materials at high temperatures show considerable disagreement, perhaps because of differences in specimen preparation since the emittance depends on surface roughness and contamination. This disagreement adversely

---

[1] Figures in square brackets indicate the literature references at the end of this dissertation.

affects the accuracy of the temperature determination.

Emittance is generally a function of wavelength. If the shape of the emittance vs. wavelength curve is known and measurements of radiance are performed at more than one wavelengths, the true temperature can be computed without explicit knowledge of the emittance values at those wavelengths. This is the principle upon which multi-wavelength radiation thermometry is based. However, the wavelength dependence of emittance is in most cases unknown and some assumption has to be made. Consequently, the accuracy of the temperature measurement will depend on the validity of this assumption.

The above discussion suggests that it is preferable to measure emittance in-situ, simultaneously with radiance temperature. In recent years, two methods for the measurement of emittance have successfully been applied to pulse-heating experiments for the determination of thermophysical properties of electrically conducting materials. The reflectometry method utilizes an integrating sphere to measure the spectral normal-hemispherical reflectance of the specimen, from which the normal spectral emittance is deduced [3]. The laser-polarimetry method is based on the measurement of the change in the polarization state of a laser beam upon reflection off the specimen surface (§3.8).

Both techniques have been used in conjunction with pulse-calorimeters designed for the determination of properties in the solid phase and up to the melting range of the investigated materials. These systems are commonly referred to as “millisecond-resolution” pulse-heating systems, a term stemming from the sampling rate of the data acquisition originally used with these systems.

The Subsecond Thermophysics Laboratory of the Metallurgy Division at the National Institute of Standards and Technology (NIST) in Maryland, USA, has been one of the major centers, worldwide, for the development of dynamic measurement techniques at high temperatures. Particular importance has always been given to highly accurate temperature measurements. The laboratory operates two pulse-heating systems: a millisecond-resolution system, and a faster microsecond-resolution system for measurements on liquid metals and alloys. Some years ago the group acquired, and helped further develop, a laser polarimeter for use with the millisecond system. The applicability of this instrument to thermophysical property measurements, in conjunction with a pulse-heating technique, has since been established [4]. More recently, in 1998, a prototype high-speed laser polarimeter was added to the laboratory's microsecond-resolution system, allowing for the first time true temperature measurements to be performed with sub-microsecond resolution. The goal of the present work was to apply this new laser polarimeter to the measurement of thermophysical properties of electrically conducting materials in their liquid phase. As a validation of the technique thermophysical properties of two metals, niobium and titanium, were determined in the temperature ranges 1600 to 3200 K and 1500 to 2200 K, respectively. These particular materials were chosen, because thermophysical property data that had been measured in the past by the same laboratory at NIST, were available for direct comparison.

Niobium was chosen for an additional reason. In 1999, an enhanced version of the microsecond-resolution laser polarimeter was acquired by the Subsecond Thermophysics Group of the Department of Experimental Physics at the Technical University of Graz, Austria. Both groups worked independently towards validating this instrument and determining its accuracy. Niobium was investigated by the group in Austria, as well, and served as a basis for comparison between the two laboratories.

2 BACKGROUND

2.1 Basic Concepts

2.1.1 Radiance

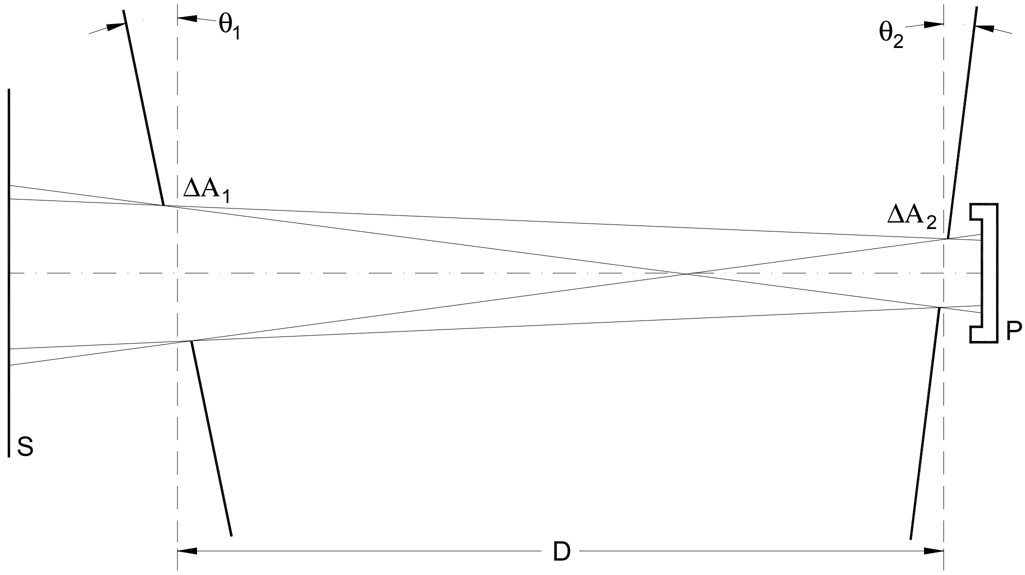

Fig. 2.1: Experiment to develop the concept of radiance (adapted from [5]). S light source, P photodetector.

One of the most basic radiometric quantities is radiance. It allows us to explicitly characterize the distribution of radiant power from point to point and direction to direction throughout a beam of optical radiation. A simple way to introduce this quantity is to consider an experiment with a large-area source that emits light uniformly and isotropically in all directions, two black screens each having a small aperture, and a photodetector next to the second screen (fig. 2.1). The photodetector responds to all radiant power reaching it from the source through both apertures. It is assumed that the medium between the source and the detector is perfectly transparent, so that the loss of radiant power by scattering or absorption is negligible. By varying the aperture areas ΔA_1 and ΔA_2, the distance D between the centers of the two apertures, and the angles of tilt θ_1 and θ_2, it is found that the measured power $\Delta\Phi$ is approximately proportional to the quantity:

$$\frac{\Delta A_1 \cdot \cos\theta_1 \cdot \Delta A_2 \cdot \cos\theta_2}{D^2} \tag{2.1}$$

The proportionality constant has to be a quantity that corresponds to the brightness of the source. We call it radiance and denote it by the letter L. The expression for $\Delta\Phi$ becomes:

$$\Delta\Phi \approx L \cdot \frac{\Delta A_1 \cdot \cos\theta_1 \cdot \Delta A_2 \cdot \cos\theta_2}{D^2} \tag{2.2}$$

The proportionality becomes more exact as the aperture areas ΔA_1 and ΔA_2 decrease relative to the distance D. In the limit of vanishingly small apertures, there remains only a single ray through both of them. The radiance L, so defined, is associated with an elementary beam collapsed to just a single ray:

$$L = \lim_{\substack{\Delta A_1 \to 0 \\ \Delta A_2 \to 0}} \frac{\Delta\Phi}{\left(\Delta A_1 \cdot \cos\theta_1 \cdot \Delta A_2 \cdot \cos\theta_2\right)/D^2} = \frac{d^2\Phi}{\left(dA_1 \cdot \cos\theta_1 \cdot dA_2 \cdot \cos\theta_2\right)/D^2} \tag{2.3}$$

Recognizing that $(dA_2 \cdot \cos\theta_2)/D^2 = d\omega_{12}$ is the solid angle subtended at dA_1 by dA_2, eq. (2.3) becomes:

$$L = \frac{d^2\Phi}{dA \cdot \cos\theta \cdot d\omega} \tag{2.4}$$

In this more general form, L is defined at a single point in the direction of a ray through that point, rather than between two points, and the assumption of a perfectly transparent medium between the two points is not necessary anymore. Expressed in words, eq. (2.4) defines the radiance at a point on a surface in the direction of a ray through that point as the radiant power per unit projected-area-perpendicular-to-the-ray-at-the-point and unit-solid-angle-in-the-direction-of-the-ray-at-the-point.

In practice, it is impossible to reduce the aperture sizes and/or increase the distance D beyond the point where there is not enough power in the beam reaching the photocell to make a measurement. Even before that point is reached, the geometrical-optics model of propagation along rays may not be adequate to describe the situation because of diffraction effects. Thus, only average values of radiance over finite intervals of area and solid angle can ever be measured. Nevertheless, keeping this limitation in mind, the concept of radiance, introduced here under the assumption of an underlying continuous distribution of flux among the rays of a beam, is still very useful.

2.1.2 Spectral Radiance

Optical radiation emitted by most sources, the propagation over many paths, and the responsivity of many detectors, all can vary greatly with wavelength. It is necessary to extend the concept of radiance so that it not only covers the distribution of radiant power with respect to position and direction, but also with respect to wavelength. Spectral radiance is the spectral distribution of radiance, defined as:

$$L_\lambda = \frac{dL}{d\lambda} = \frac{d^3\Phi}{dA \cdot \cos\theta \cdot d\omega \cdot d\lambda} \tag{2.5}$$

Spectral radiance, like radiance, is defined at a point on a surface in the direction of a ray trough that point.

2.1.3 Self-exitance

The spectral self-exitance[1] M_λ of a surface element dA at a wavelength λ is defined as the radiant power per unit area associated with emission into the hemispheric space above dA, i.e. in all possible directions, within an infinitesimal wavelength interval $d\lambda$ around λ. It may be determined by integration of eq. (2.5), if the directional distribution of the spectral radiance L_λ is known:

$$M_\lambda(\lambda) = \frac{d^2\Phi}{dA \cdot d\lambda} = \int_{\varphi=0}^{2\pi} \int_{\theta=0}^{\pi/2} L_\lambda(\lambda,\theta,\phi) \cdot \cos\theta \cdot \sin\theta \cdot d\theta \cdot d\phi \tag{2.6}$$

The total self-exitance M of a surface element dA is defined as the radiant power per unit area emitted by dA in all possible directions and over all wavelengths. It may be determined by integration of eq. (2.6), if the directional and spectral distributions of the spectral radiance L_λ are known:

$$M = \frac{d\Phi}{dA} = \int_{\lambda=0}^{\infty} M_\lambda(\lambda) \cdot d\lambda = \int_{\lambda=0}^{\infty} \int_{\varphi=0}^{2\pi} \int_{\theta=0}^{\pi/2} L_\lambda(\lambda,\theta,\phi) \cdot \cos\theta \cdot \sin\theta \cdot d\theta \cdot d\phi \cdot d\lambda \tag{2.7}$$

In the case of an isotropically diffuse emitter (also referred to as a lambertian emitter) the radiance of the emitted radiation is independent of direction. In this special case L_λ can be removed from the integrals in eqs. (2.6) and (2.7). Performing the integration over all directions results in

---

[1] Exitance refers to radiation leaving a surface element both due to emission and reflection from the surface. The term self-exitance refers to emitted radiation only.

$$M_\lambda(\lambda) = \pi \cdot L_\lambda(\lambda) \tag{2.8}$$

and

$$M = \pi \cdot L, \tag{2.9}$$

respectively[1].

2.1.4 Irradiance

If the radiation is incident on a surface (instead of exitent from the surface) the foregoing concepts can be adapted to the definition of spectral irradiance E_λ and total irradiance E. Equations (2.6) - (2.9) then become:

$$E_\lambda(\lambda) = \frac{d^2\Phi}{dA \cdot d\lambda} = \int_{\varphi=0}^{2\pi} \int_{\theta=0}^{\pi/2} L_\lambda(\lambda,\theta,\phi) \cdot \cos\theta \cdot \sin\theta \cdot d\theta \cdot d\phi \tag{2.10}$$

$$E = \frac{d\Phi}{dA} = \int_{\lambda=0}^{\infty} E_\lambda(\lambda) \cdot d\lambda = \int_{\lambda=0}^{\infty} \int_{\varphi=0}^{2\pi} \int_{\theta=0}^{\pi/2} L_\lambda(\lambda,\theta,\phi) \cdot \cos\theta \cdot \sin\theta \cdot d\theta \cdot d\phi \cdot d\lambda \tag{2.11}$$

$$E_\lambda(\lambda) = \pi \cdot L_\lambda(\lambda) \tag{2.12}$$

$$E = \pi \cdot L \tag{2.13}$$

The last two expressions reflect the special case when the surface element dA is irradiated isotropically (L_λ is independent of direction).

2.1.5 Blackbodies

A blackbody is a surface (material or geometrical) that absorbs all radiant flux of all wavelengths and polarizations incident upon it from all possible directions. For a prescribed temperature and wavelength, no surface can emit more thermal radiation than a blackbody. Furthermore, a blackbody is an isotropically diffuse (lambertian) emitter, i.e. the radiation emitted by it is independent of direction.

Although there is no real surface that precisely has these properties, the concept of a blackbody is useful in describing the radiative characteristics of real surfaces. The closest

---

[1] The constant π appearing in the above expressions has the unit steradian (sr) of a solid angle.

approximation to a blackbody surface is given by the aperture of a cavity (an opaque enclosure) whose inner surface is at a uniform temperature.

2.1.6 The Planck law

Planck's radiation law relates the spectral distribution of the radiance $L_{\lambda,b}$ emitted by a blackbody to its temperature T. In terms of the ‘local’ wavelength λ in a medium with refractive index n it takes the form:

$$L_{\lambda,b}(\lambda,T)=\frac{c_{1L}}{n^2\cdot\lambda^5}\cdot\left[\exp\left(\frac{c_2}{n\cdot\lambda\cdot T}\right)-1\right]^{-1} \tag{2.14}$$

where $c_{1L}=2\cdot h\cdot c_0^2$ is the first radiation constant[1] (for radiance L) and $c_2=h\cdot c_0\cdot k_B^{-1}$ is the second radiation constant. c_0 is the speed of light in vacuum, h is Planck's constant of action, and k_B is the Boltzmann constant.

2.1.7 The Wien displacement law

The wavelength λ_{max}, in a medium with refractive index n, at which the spectral distribution of the radiance emitted by a blackbody at temperature T has its maximum is given by Wien's displacement law:

$$n\cdot\lambda_{max}\cdot T=2897.8\,\mu m\cdot K \tag{2.15}$$

Accordingly, as the temperature increases the maximum of the emitted blackbody radiance shifts to shorter wavelengths.

2.1.8 The Wien approximation to the Planck law

If $n\cdot\lambda\cdot T<<c_2$ the unit in the denominator of Planck's law can be neglected compared to the exponential, resulting in Wien's approximation for short wavelengths and low temperatures:

$$L_{\lambda,b}(\lambda,T)=\frac{c_{1L}}{n^2\cdot\lambda^5}\cdot\left[\exp(\frac{c_2}{n\cdot\lambda\cdot T})\right]^{-1} \tag{2.16}$$

This expression is accurate to better than 1% if $n\cdot\lambda\cdot T\leq 3100$ μm·K. Wien's approximation is very useful whenever derivatives of $L_{\lambda,b}$ are involved, e.g. in propagation-of-error equations.

---

[1] The first radiation constant c_1 (for exitance) usually encountered in literature, is related to c_{1L} by $c_1=\pi\cdot c_{1L}$.

2.1.9 Emittance

As already mentioned, a blackbody is an ideal surface that can only be approximated. The emittance of a real surface is a measure of its ability to emit thermal radiation, as compared to that of a blackbody at the same temperature. In general it will depend on direction and wavelength. The spectral-directional emittance of a surface at the temperature T, the wavelength λ, and in the direction (θ, ϕ) is given by

$$\varepsilon(\lambda,\theta,\phi,T) = \frac{L_\lambda(\lambda,\theta,\phi,T)}{L_{\lambda,b}(\lambda,T)} \tag{2.17}$$

The spectral-hemispherical emittance of a surface at the temperature T and wavelength λ is defined as the ratio of its spectral self-exitance to that of a blackbody at the same temperature and wavelength:

$$\varepsilon(\lambda,2\pi,T) = \frac{M_\lambda(\lambda,T)}{M_{\lambda,b}(\lambda,T)} \tag{2.18}$$

Similarly, the total-hemispherical emittance of a surface at the temperature T is given by the ratio of its total self-exitance to that of a blackbody at the same temperature:

$$\varepsilon(t,2\pi,T) = \frac{M(T)}{M_b(T)} = \frac{\int_0^\infty M_\lambda(\lambda,T)\cdot d\lambda}{\int_0^\infty M_{\lambda,b}(\lambda,T)\cdot d\lambda} = \frac{\int_0^\infty \varepsilon(\lambda,2\pi,T)\cdot M_{\lambda,b}(\lambda,T)\cdot d\lambda}{\int_0^\infty M_{\lambda,b}(\lambda,T)\cdot d\lambda} \tag{2.19}$$

For an isotropically diffuse emitter it follows from eqs. (2.8), (2.17), and (2.18), that $\varepsilon(\lambda,\theta,\phi,T) = \varepsilon(\lambda,2\pi,T)$. If, in addition, the surface is gray, that is, if its spectral-directional emittance is independent of wavelength, then $\varepsilon(\lambda,\theta,\phi,T) = \varepsilon(\lambda,2\pi,T) = \varepsilon(t,2\pi,T)$.

For a blackbody, of course, $\varepsilon(\lambda,\theta,\phi,T) = \varepsilon(\lambda,2\pi,T) = \varepsilon(t,2\pi,T) = 1$.

2.1.10 Absorptance

As in the case of emittance, we define a spectral-directional, a spectral-hemispherical, and a total-hemispherical quantity. The spectral-directional absorptance of a surface element is given by:

$$\alpha(\lambda,\theta,\phi,T) = \frac{L_{\lambda,a}(\lambda,\theta,\phi,T)}{L_{\lambda,i}(\lambda,\theta,\phi)} \tag{2.20}$$

where $L_{\lambda,i}$ is the spectral radiance at the wavelength λ incident on the surface element from the direction (θ, ϕ) and $L_{\lambda,a}$ is the part thereof that is absorbed by the surface element. The modifier T in the brackets indicates that this property is, in general, temperature-dependent.

The spectral-hemispherical absorptance of a surface element is defined as the fraction of the spectral irradiance at the surface element that is absorbed by it:

$$\alpha(\lambda,2\pi,T)=\frac{E_{\lambda,a}(\lambda,T)}{E_{\lambda}(\lambda)} \tag{2.21}$$

This property represents a weighted average of $\alpha(\lambda,\theta,\phi,T)$ over all directions above the surface element and depends on the directional distribution of the incident radiance, which has to be specified when reporting this property.

Similarly, the total-hemispherical absorptance of a surface element is defined as the fraction of the total irradiance at the surface element that is absorbed by it:

$$\alpha(t,2\pi,T)=\frac{E_a(T)}{E}=\frac{\int\limits_0^\infty E_{\lambda,a}(\lambda,T)\cdot d\lambda}{\int\limits_0^\infty E_{\lambda}(\lambda)\cdot d\lambda}=\frac{\int\limits_0^\infty \alpha(\lambda,2\pi,T)\cdot E_{\lambda}(\lambda)\cdot d\lambda}{\int\limits_0^\infty E_{\lambda}(\lambda)\cdot d\lambda} \tag{2.22}$$

This property depends both on the directional and spectral distributions of the incident radiance.

2.1.11 Reflectance

Reflection is the process by which radiant flux incident on a stationery surface leaves that surface from the incident side without change in frequency. Reflectance is the fraction of incident flux that is reflected. However, its specific definition may take several different forms, because this property is inherently bidirectional. That is, it depends on the direction of the incident and the reflected radiation.

The spectral directional-hemispherical reflectance is the fraction of the incident flux at a wavelength λ and from a specific direction (θ,ϕ) that is reflected into the hemisphere above the surface. It can be written as:

$$\rho(\lambda,\theta,\phi,2\pi,T)=\frac{M_{\lambda,r}(\lambda,T)}{E_{\lambda}(\lambda,\theta,\phi)} \tag{2.23}$$

where $M_{\lambda,r}$ is the spectral exitance (due to reflected spectral irradiance) and E_λ is the spectral irradiance in the incident direction. The modifier T in the brackets indicates the temperature dependence of this property.

2.1.12 Transmittance

Transmission through a semitransparent medium is, like the reflectance, a bidirectional property. For this reason transmittance (which, due to interreflections, may depend on the thickness of the material as well as on its optical properties) may take various forms. The spectral directional-hemispherical transmittance is defined as the fraction of the incident flux at a wavelength λ and from a specific direction (θ,ϕ) that is transmitted through the medium into the hemisphere surrounding the exitent surface:

$$\tau(\lambda,\theta,\phi,2\pi,T)=\frac{M_{\lambda,t}(\lambda,T)}{E_\lambda(\lambda,\theta,\phi)} \tag{2.24}$$

where E_λ is the spectral irradiance in the incident direction at the front surface and $M_{\lambda,t}$ is the spectral exitance (due to transmitted spectral irradiance) at the back surface. The modifier T in the brackets indicates the temperature dependence of this property.

2.1.13 The Kirchhoff law

In its most general form, Kirchhoff's law states that the spectral-directional emittance and the spectral-directional absorptance of a surface are equal. This equality can be written as

$$\varepsilon(\lambda,\theta,\phi,T)=\alpha(\lambda,\theta,\phi,T) \tag{2.25}$$

and is valid for any surface without restrictions. There are other forms of this law that are valid under certain conditions.

If the surface is an isotropically diffuse emitter or the surface irradiation is isotropically diffuse, it follows from eq. (2.25) that

$$\varepsilon(\lambda,2\pi,T)=\alpha(\lambda,2\pi,T) \tag{2.26}$$

In this case and if, in addition, the surface is gray or the spectral irradiance at the surface is proportional to the spectral exitance of a blackbody at the surface temperature T, Kirchhoff's law is valid for the total-hemispherical emittance and absorptance:

$$\varepsilon(t,2\pi,T)=\alpha(t,2\pi,T) \tag{2.27}$$

2.1.14 Energy balance

From energy balance considerations it follows readily that

$$\rho(\lambda,\theta,\phi,2\pi,T)+\alpha(\lambda,\theta,\phi,T)+\tau(\lambda,\theta,\phi,2\pi,T)=1 \tag{2.28}$$

For opaque materials, $\tau = 0$ and eq. (2.28) becomes:

$$\rho(\lambda,\theta,\phi,2\pi,T)+\alpha(\lambda,\theta,\phi,T)=1 \tag{2.29}$$

The reflection and absorption processes may then be treated as surface phenomena. Combining this expression with Kirchhoff's law we obtain

$$\rho(\lambda,\theta,\phi,2\pi,T)+\varepsilon(\lambda,\theta,\phi,T)=1 \tag{2.30}$$

and for normal incidence - emission

$$\rho_{n,h}(\lambda,T)+\varepsilon_n(\lambda,T)=1 \tag{2.31}$$

where $\rho_{n,h}(\lambda,T)$ and $\varepsilon_n(\lambda,T)$ are the spectral normal-hemispherical reflectance and normal spectral emittance, respectively.

2.2 Radiation Thermometry

Temperature determination by radiation thermometry is based on the fact that the radiance emitted by an object is a function of its temperature. If the object is a blackbody its temperature can be inferred from the emitted radiance using Planck's law (eq. 2.14). In the case of a non-blackbody, knowledge of the object's emittance is required to obtain its temperature.

2.2.1 The International Temperature Scale of 1990 (ITS-90)

According to the ITS-90 [6], above the freezing point of silver the temperature T is defined by the equation:

$$\frac{L_{\lambda,b}(\lambda_0,T)}{L_{\lambda,b}(\lambda_0,T_0)}=\frac{\exp(c_2/\lambda_0T_0)-1}{\exp(c_2/\lambda_0T)-1} \tag{2.32}$$

where T_0 refers to any one of the silver (T_{Ag} = 1234.93 K), the gold (T_{Au} = 1337.33 K) or the copper ($T_{Cu} = 1357.77$ K) freezing points. $L_{\lambda,b}(\lambda_0,T)$ and $L_{\lambda,b}(\lambda_0,T_0)$ denote the blackbody spectral radiance at the wavelength (in vacuum) λ_0 and at the temperatures T and at T_0, respectively. $c_2 = 0.014388$ m·K is the second radiation constant.

2.2.2 Radiance temperature

The (spectral) radiance temperature at a wavelength λ of a surface at a temperature T is the temperature T_λ at which a blackbody emits the same amount of spectral radiance at λ as does the surface[1]. Since no surface can emit more thermal radiation than a blackbody it follows that T_λ is always lower than T. For a blackbody of course, $T_\lambda = T$. According to the definition of radiance temperature and eq. (2.17),

$$L_{\lambda,b}(\lambda,T_\lambda) = L_\lambda(\lambda,\theta,\phi,T) = \varepsilon(\lambda,\theta,\phi,T)\cdot L_{\lambda,b}(\lambda,T) \ , \tag{2.33}$$

which, combined with Planck's law, leads to the following expression relating the two temperatures:

$$T = \frac{c_2}{n\cdot\lambda}\cdot\left[\ln\left\{1+\varepsilon(\lambda,\theta,\phi,T)\cdot\left[\exp\left(\frac{c_2}{n\cdot\lambda\cdot T_\lambda}\right)-1\right]\right\}\right]^{-1} \tag{2.34}$$

Since the spectral-directional emittance depends, in the most general case, on the wavelength, the direction of emission, and the true temperature of the emitting surface, it follows that the radiance temperature depends on these parameters, as well.

A simpler and in many cases very useful expression can be derived using the Wien approximation (for $n\cdot\lambda\cdot T \leq 3100$ µm·K):

$$\frac{1}{T} = \frac{1}{T_\lambda} + \frac{n\cdot\lambda}{c_2}\cdot\ln\varepsilon(\lambda,\theta,\phi,T) \tag{2.35}$$

Keeping in mind that $\varepsilon_\lambda \leq 1$, it can be seen that $T \geq T_\lambda$, as was mentioned above. The lower the emittance is, the lower the radiance temperature will be. In addition, T_λ decreases with increasing wavelength, if the emittance ε is kept constant.

---

[1] In order to clearly distinguish T from T_λ and avoid ambiguity, the former will usually be called the true or thermodynamic temperature of the surface.

2.2.3 The measurement equation of a radiation thermometer

From equation (2.5), the element of radiant flux $d\Phi(\lambda,x,y,\theta,\phi)$ associated with a ray of spectral radiance $L_\lambda(\lambda,x,y,\theta,\phi)$ through a surface element $dA = dx \cdot dy$ at its point of intersection (x,y) with the ray, within an element of solid angle $d\omega$ about the ray in the direction (θ,ϕ), and within an elemental wavelength interval $d\lambda$ about λ, is:

$$d\Phi(\lambda, x, y, \theta, \phi) = L_\lambda(\lambda, x, y, \theta, \phi) \cdot \cos\theta \cdot d\omega \cdot dA \cdot d\lambda \tag{2.5}$$

Most radiation detectors respond to radiant flux (power). The quantity relating the output signal S of a detector to the incident radiant flux Φ is called the flux responsivity R_Φ of the detector. In general, it will vary with the position and direction of the incoming rays at the receiving aperture and be a function of wavelength[1]:

$$R_\Phi(\lambda, x, y, \theta, \phi) = \frac{dS(\lambda, x, y, \theta, \phi)}{d\Phi(\lambda, x, y, \theta, \phi)} \tag{2.36}$$

When the detector is part of a radiation thermometer the overall instrument responsivity is also determined by (1) the transmittance τ of the optical components (e.g. lenses, filters) and paths internal to the instrument and (2) the electronic processing (e.g. conversion of a photodiode current into a voltage and amplification) that the detector signal undergoes to produce the final instrument output signal.

Combining all the above, an expression for the elemental instrument output signal dS stemming from the element of flux $d\Phi$ along one ray in the beam of radiation incident on the radiation thermometer can be written as:

$$dS(\lambda, x, y, \theta, \phi) = b \cdot \tau(\lambda, x, y, \theta, \phi) \cdot R_\Phi(\lambda, x, y, \theta, \phi) \cdot d\Phi(\lambda, x, y, \theta, \phi) \tag{2.37}$$

with $d\Phi(\lambda,x,y,\theta,\phi)$ from eq. (2.5). The constant b is determined by the electronics that process the detector output signal. The total output signal S of the radiometer is the sum (integral) of all the elemental signals dS for all the rays included in the beam of radiation accepted by the instrument:

$$S(\Delta\lambda, A, \omega) = \int_{\Delta\lambda} \int_{A} \int_{\omega} b \cdot \tau(\lambda, x, y, \theta, \phi) \cdot R_\Phi(\lambda, x, y, \theta, \phi) \cdot L_\lambda(\lambda, x, y, \theta, \phi) \cdot \cos\theta \cdot d\omega \cdot dA \cdot d\lambda \tag{2.38}$$

---

[1] The detector is assumed to be linear over the measurement range of interest. In other words, the responsivity of the detector is assumed to be independent of the magnitude of the flux incident on it.

where $\Delta\lambda$ is the wavelength interval over which the instrument responsivity is significantly non-zero, A is the area of the receiving aperture, and ω is the solid angle enclosed by the extreme rays from the target that converge at a point x,y on the receiving aperture[1]. This is the so called measurement equation [7]. It relates the output signal of the measuring instrument to the incident spectral radiance distribution. In addition, it shows that the output signal S may be regarded as the overall-responsivity-weighted flux in the beam that is received by the instrument.

The range of variation of τ, R_Φ, and L_λ relative to position and direction can be minimized by making A and ω sufficiently small. These quantities can then be taken out of the integrals over A and ω:

$$S(\Delta\lambda, A, \omega) = \int_{\Delta\lambda} R_L(\lambda, A, \omega) \cdot L_\lambda(\lambda) \cdot d\lambda \ , \tag{2.39}$$

where

$$R_L(\lambda, A, \omega) = b \cdot \tau(\lambda) \cdot R_\Phi(\lambda) \cdot \int_A \int_\omega \cos\theta \cdot d\omega \cdot dA \tag{2.40}$$

is the spectral-radiance responsivity of the instrument.

2.2.4 Determination of the temperature of a blackbody

In the case of a strictly monochromatic radiation thermometer the integral in eq. (2.39) is reduced to a simple product. The output signal S is then directly proportional to the spectral radiance emitted by the blackbody and the defining equation of the ITS-90 can be applied without difficulty. However, any observable radiant flux is always associated with a spectral band of finite width and the question arises as to which wavelength within this spectral band to use in eq. (2.32).

The instrument is calibrated in terms of the spectral radiance of a blackbody at the temperature T_0 of a fixed point in the temperature scale, such as the freezing point of gold. The radiometer signal in this case will be:

---

[1] If there is vignetting, ω is a function of the position x,y on the receiving aperture and should be written $\omega(x,y)$.

$$S(T_0) = \int_{\Delta\lambda} R_L(\lambda) \cdot L_{\lambda,b}(\lambda, T_0) \cdot d\lambda \qquad (2.41)$$[1]

When the radiometer is sighted upon a blackbody at an unknown higher temperature T a signal S(T) is generated and the temperature T is then determined by solving the integral equation:

$$\int_{\Delta\lambda} \tau_{nd} \cdot R_L(\lambda) \cdot L_{\lambda,b}(\lambda, T) \cdot d\lambda = \int_{\Delta\lambda} R_L(\lambda) \cdot L_{\lambda,b}(\lambda, T_0) \cdot d\lambda \ , \qquad (2.42)$$

where τ_{nd} is the ratio of $S(T_0)$ to S(T). It can also be interpreted as the transmittance of a neutral density filter[2] that has to be placed in the optical path when viewing the higher temperature blackbody so that the generated signal $\tau_{nd} \cdot S(T)$ is equal to the signal $S(T_0)$ generated by the fixed-point blackbody.

2.2.4.1 The concept of the mean effective wavelength and the limiting effective wavelength

Although solving an integral equation numerically presents no problem to a digital computer, there are situations where it is desirable to have some simpler algorithm available. The equality of the integrals in eq. (2.42) means that the areas under the curves represented by the integrands are equal. The wavelength at which the two curves intersect, in other words the wavelength at which the integrands themselves are equal, is called the mean effective wavelength between the temperatures T_0 and T and is denoted by $\lambda_{T_0\text{-}T}$. It follows that at this wavelength:

$$\tau_{nd} = \frac{S(T_0)}{S(T)} = \frac{L_{\lambda,b}(\lambda_{T_0-T}, T_0)}{L_{\lambda,b}(\lambda_{T_0-T}, T)} = \frac{\exp(c_2/n \cdot \lambda_{T_0-T} \cdot T) - 1}{\exp(c_2/n \cdot \lambda_{T_0-T} \cdot T_0) - 1} \qquad (2.43)$$

This is the working version of the defining equation of the ITS-90 (compare to eq. 2.32) for a radiation thermometer with a finite spectral bandwidth.

The limiting effective wavelength λ_T at the temperature T is defined as:

$$\frac{1}{\lambda_T} = \lim_{T_0 \to T} \frac{1}{\lambda_{T_0-T}} \qquad (2.44)$$

---

[1] For brevity, the parameters Δλ, A, and ω have been omitted from $S(\Delta\lambda, A, \omega, T_0)$ and $R_L(\lambda, A, \omega)$ under the assumption that all measurements, including the calibration, are made under identical conditions. That is to say, the spectral band Δλ and the focusing adjustment and position of the radiation thermometer remain unchanged.

[2] A filter with uniform transmittance (at least) across the spectral band Δλ of the radiometer.

Assuming the applicability of Wien's approximation to Planck's law it can be shown [8, 9] that[1]:

$$\frac{1}{\lambda_{T_0-T}} = \frac{1}{\frac{1}{T}-\frac{1}{T_0}} \cdot \int_{1/T_0}^{1/T} \frac{1}{\lambda_T} \cdot d(\frac{1}{T}) \tag{2.45}$$

and

$$\frac{1}{\lambda_T} = \frac{\int\limits_{\Delta\lambda} \frac{1}{\lambda} \cdot R_L(\lambda) \cdot L_{\lambda,b}(\lambda,T) \cdot d\lambda}{\int\limits_{\Delta\lambda} R_L(\lambda) \cdot L_{\lambda,b}(\lambda,T) \cdot d\lambda} \tag{2.46}$$

According to the last expression, it can be said that the inverse limiting effective wavelength is a weighted average of inverse wavelength over the spectral bandwidth of the radiometer, with the instrument's spectral-radiance responsivity and blackbody spectral-radiance distribution as the weighing factors. In addition, it turns out that the inverse limiting effective wavelength is very nearly a linear function of inverse temperature so that

$$\frac{1}{\lambda_{T_0-T}} \cong \frac{1}{2} \cdot \left(\frac{1}{\lambda_{T_0}} + \frac{1}{\lambda_T} \right), \tag{2.47}$$

which makes it obvious why the name "mean effective wavelength" is used. From eq. (2.46) the limiting effective wavelength of the radiation thermometer when viewing a blackbody can be computed for any temperature. Then, using eq. (2.45) or (2.47), the mean effective wavelength between any two temperatures can be obtained. When one of the temperatures is not known initially (the known temperature usually being the calibration temperature) the mean effective wavelength is approximated by the center wavelength or the wavelength of peak transmission of the wavelength-selecting component (e.g. an interference filter or a monochromator) of the instrument. The unknown temperature is computed with eq. (2.43) and used to obtain a better approximation of the mean effective wavelength, which in turn is used to obtain a better value for the unknown temperature. One such iteration is usually sufficient.

---

[1] An expression for the limiting effective wavelength derived using Planck's law can be found in [10]. The authors show that the error introduced by the use of Wien's approximation is negligible for most purposes.

2.2.5 Determination of the temperature of a non-blackbody

In the case of a non-blackbody at a temperature T, eq. (2.42) becomes

$$\int_{\Delta\lambda} \tau_{nd} \cdot R_L(\lambda) \cdot \varepsilon(\lambda) \cdot L_{\lambda,b}(\lambda, T) \cdot d\lambda = \int_{\Delta\lambda} R_L(\lambda) \cdot L_{\lambda,b}(\lambda, T_0) \cdot d\lambda \qquad (2.48)$$

This integral equation can be solved numerically if the spectral emittance of the non-blackbody is known throughout the passband $\Delta\lambda$. In writing this expression, the implicit assumption has been made that the variation of the emittance with position and direction of the incoming rays at the receiving aperture of the instrument is negligible, so that ε (like τ and R_Φ) can be taken out of the respective integrals in eq. (2.38). This can be achieved by keeping the area A of the receiving aperture and the solid angle ω subtended by the target area at any point on the receiving aperture sufficiently small.

Radiation thermometers are calibrated in terms of blackbody radiation. Thus, in the absence of any knowledge about the emittance, they indicate the target's radiance temperature T_λ, which satisfies the following equation:

$$\int_{\Delta\lambda} \tau_{nd} \cdot R_L(\lambda) \cdot L_{\lambda,b}(\lambda, T_\lambda) \cdot d\lambda = \int_{\Delta\lambda} R_L(\lambda) \cdot L_{\lambda,b}(\lambda, T_0) \cdot d\lambda \qquad (2.49)$$

This expression is identical to eq. (2.42) (with T replaced by T_λ). Thus, it can be solved for T_λ numerically or by applying the concept of the mean effective wavelength:

$$\tau_{nd} = \frac{L_{\lambda,b}(\lambda_{T_0-T_\lambda}, T_0)}{L_{\lambda,b}(\lambda_{T_0-T_\lambda}, T_\lambda)} = \frac{\exp(c_2 / n \cdot \lambda_{T_0-T_\lambda} \cdot T_\lambda) - 1}{\exp(c_2 / n \cdot \lambda_{T_0-T_\lambda} \cdot T_0) - 1} \qquad (2.50)$$

with $\lambda_{T_0\text{-}T_\lambda}$ from eqs. (2.45) and (2.46). Although the same concept may, in principle, be applied to the determination of the true temperature, equations (2.45) and (2.46) may not, since they were derived for blackbodies. However, if it can be assumed that the emittance ε is nearly constant throughout the passband $\Delta\lambda$, then, combining eqs. (2.48) and (2.49), we can write[1]:

$$\int_{\Delta\lambda} \varepsilon \cdot R_L(\lambda) \cdot L_{\lambda,b}(\lambda, T) \cdot d\lambda = \int_{\Delta\lambda} R_L(\lambda) \cdot L_{\lambda,b}(\lambda, T_\lambda) \cdot d\lambda \qquad (2.51)$$

---

[1] A less restrictive condition [8] is that an equivalent graybody temperature T_g and a corresponding graybody emittance ε_g can be found, such that $\varepsilon_g \cdot L_{\lambda,b}(\lambda, T_g) = \varepsilon(\lambda) \cdot L_{\lambda,b}(\lambda, T)$.

This equation just expresses the fact that the radiance temperature T_λ is the temperature of a blackbody that, when viewed through the radiation thermometer, gives rise to the same output signal as the non-blackbody. It is identical to eq. (2.42) if τ_{nd} and T_0 are replaced by ε and T_λ, respectively. Thus, the true temperature T can be determined from T_λ and ε by solving

$$\varepsilon = \frac{L_{\lambda,b}(\lambda_{T_\lambda - T}, T_\lambda)}{L_{\lambda,b}(\lambda_{T_\lambda - T}, T)} = \frac{\exp(c_2 / n \cdot \lambda_{T_\lambda - T} \cdot T) - 1}{\exp(c_2 / n \cdot \lambda_{T_\lambda - T} \cdot T_\lambda) - 1} \tag{2.52}$$

According to its defining equation (2.33), the radiance temperature depends on the wavelength. Equation (2.52) shows that, when viewing a graybody, the wavelength to be associated with the radiance temperature T_λ measured by a finite-bandwidth radiation thermometer is the mean effective wavelength $\lambda_{T_\lambda\text{-}T}$ between T_λ and the target's true temperature T. Looking at the equation used to compute the limiting effective wavelength, it is clear that $\lambda_{T_\lambda\text{-}T}$ will depend on the central wavelength, as well as the shape and width of the spectral passband of the measuring instrument. Thus, two instruments with spectral passbands centered at the same wavelength will measure different radiance temperatures if the shape and/or the width of their passbands are different. In other words, they correspond to monochromatic radiation thermometers operating at different wavelengths.

2.3 Polarimetry

2.3.1 The concept of polarization

Polarization is a property that is common to all types of vector waves. It refers to the behavior with time of one of the field vectors appropriate to that type of wave, observed at a fixed point in space.

In the case of electromagnetic waves the electric-field strength **E** is chosen to define the state of polarization. This choice is based on the fact that when the wave interacts with matter, the force exerted on the electrons by the magnetic component of the field is generally negligible compared to the force exerted by the electric component.

2.3.2 The polarization of monochromatic waves

The word “monochromatic” originates in the greek language and means “consisting of one color”. In the language of physics it, more generally, stands for “consisting of one frequency”.

For a monochromatic wave the variation with time of the electric vector **E** is exactly sinusoidal, in other words it is time-harmonic. Such an idealized wave is of infinite extent.

2.3.2.1 Elliptical polarization

At a fixed point in space the vibration of the electric vector **E** may, in the most general case, be resolved into three independent, linear, harmonic vibrations E_x, E_y, and E_z along three mutually orthogonal directions x, y, and z, respectively:

$$\mathbf{E} = E_x \mathbf{e}^x + E_y \mathbf{e}^y + E_z \mathbf{e}^z \qquad (2.53)^1$$

$$E_i = E_{0i} \cdot \cos(\omega t + \delta_i), \qquad i = x, y, z \qquad (2.54)$$

$\mathbf{e}^x$, $\mathbf{e}^y$, and $\mathbf{e}^z$ are unit vectors along the coordinate axes; ω is the angular frequency of the vibration of **E**; E_{0i} and δ_i denote the real amplitude and initial phase angle, respectively, of the linear vibration along the *i*th coordinate axis.

It can be shown that the endpoint of the instantaneous electric vector **E**, drawn from the fixed observation point as an origin, will trace an ellipse in space. An electromagnetic wave whose electric vector at a fixed point in space traces the same ellipse in a regular repetitive fashion is described as elliptically polarized at that point.

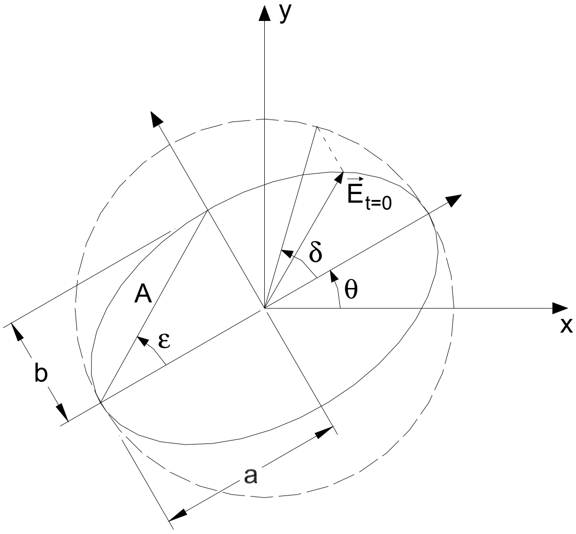

Fig. 2.2: The ellipse of polarization and the four parameters that are required to completely describe it in its plane (adapted from [11]).

---

[1] Bold characters denote vectors or matrices.

Elliptical polarization is the most general state of polarization of a strictly monochromatic electromagnetic field. Six real parameters are required for its complete description. Two of them are necessary to determine the orientation of the plane of the ellipse by means of a unit vector **n** normal to that plane[1]. The other four parameters describe the ellipse of polarization in its plane. In the very important special case of a transverse wave, the plane of vibration of the electric vector is normal to the direction of propagation and **n** is parallel to the wave-vector **k**. In this case only the four parameters describing the ellipse of polarization in its plane are required for a complete specification of the state of polarization (fig. 2.2).

(1) The azimuth θ defines the orientation of the ellipse in its plane. It is the angle between the major axis of the ellipse and the positive direction of the x axis. The range of θ is limited to:

$$-\frac{\pi}{2} \leq \theta < \frac{\pi}{2} \tag{2.55}$$

(2) The ellipticity e describes the shape of the polarization ellipse. It is defined as the ratio of the length b of the semi-minor axis of the ellipse to the length a of its semi-major axis.

$$e = \frac{b}{a} \tag{2.56}$$

It is convenient to incorporate the handedness of the ellipse, i.e. the sense in which it is described, in the definition of e, by allowing it to assume positive and negative values to correspond to right-handed and left-handed polarizations, respectively. We speak of right-handed polarization if the ellipse is traversed in a clockwise sense when looking toward the source of the wave, that is against the direction of propagation. We speak of left-handed polarization if the ellipse is traversed in a counter-clockwise sense when looking against the direction of propagation. The range of e is limited to:

$$-1 \leq e \leq 1 \tag{2.57}$$

An ellipticity angle ε is introduced such that:

$$\tan\varepsilon = e \tag{2.58}$$

---

[1] The direction of this vector is chosen to be that of the average energy flow along the normal to the plane of the ellipse. Because **n** is a unit vector its third coordinate can be determined from the other two.

From eq. (2.57) it follows that:

$$-\frac{\pi}{4} \leq \varepsilon \leq \frac{\pi}{4} \tag{2.59}$$

(3) The amplitude A of the of the polarization ellipse is a measure of its size. The square of A is proportional to the energy density of the electromagnetic wave at the point of observation. It is defined in terms of the lengths a and b of the semi-major and semi-minor axes of the ellipse as:

$$A = \left(a^2 + b^2\right)^{1/2} \tag{2.60}$$

(4) The fourth real quantity needed to fully specify the ellipse of polarization in its plane is the absolute phase angle δ at $t = 0$ (fig. 2.2).

2.3.2.2 Linear and circular polarizations

The linear and circular polarizations are limiting special cases of the more general elliptical polarization state. Linear polarization occurs when the length of the semi-minor axis is negligibly small compared to that of the semi-major axis, that is to say when $e = 0$. Circular polarization occurs in the limit when the length of the semi-minor axis approaches that of the semi-major axis so that $e = \pm 1$. The positive value corresponds to right-handed circular polarization and the negative value to left-handed circular polarization. It is important to note that circular polarizations have indeterminate azimuth.

Any arbitrarily polarized wave can be expressed as the superposition of two linearly polarized waves. In the case of a transverse plane wave we may write:

$$\mathbf{E}(\mathbf{r},t) = \left[E_{01} \cdot \cos(\omega t - \mathbf{k} \cdot \mathbf{r} + \delta_1)\right] \cdot \mathbf{u}_1 + \left[E_{02} \cdot \cos(\omega t - \mathbf{k} \cdot \mathbf{r} + \delta_2)\right] \cdot \mathbf{u}_2 \tag{2.61}$$

$$\mathbf{u}_1 \cdot \mathbf{u}_1 = \mathbf{u}_2 \cdot \mathbf{u}_2 = 1, \quad \mathbf{u}_1 \cdot \mathbf{u}_2 = \mathbf{u}_1 \cdot \mathbf{k} = \mathbf{u}_2 \cdot \mathbf{k} = 0 \tag{2.62}$$

$\mathbf{u}_1$ and $\mathbf{u}_2$ are two orthogonal unit vectors in the wave-front along which the electric vector is resolved into components of amplitudes E_{01} and E_{02} and initial phases δ_1 and δ_2. $\mathbf{k}$ is the constant wave-vector and $\mathbf{r}$ is the position vector.

2.3.3 The polarization of quasi-monochromatic waves

A perfectly monochromatic electromagnetic wave must, by its very nature, be totally polarized. By "totally" polarized it is meant that the electric vector **E** at a fixed point in space will trace an ellipse (linear and circular polarization being limiting special cases) in a regular repetitive fashion. In actuality, light is emitted in wavetrains that are limited both in time and space; they have a beginning and an end. Thus, existing light sources never exactly satisfy the condition of monochromacy. Instead they are "polychromatic", meaning that they emit electromagnetic waves whose Fourier-analyzed spectrum consists of a range of frequencies. A wave whose frequency bandwidth $\Delta\omega$ is very small in comparison with its mean frequency $\overline{\omega}$ is called a quasi-monochromatic wave. At a fixed point in space the vibration of the electric vector for such a wave may be written as:

$$\mathbf{E} = E_x \mathbf{e}^x + E_y \mathbf{e}^y + E_z \mathbf{e}^z \tag{2.63}$$

$$E_i = E_{0i}(t) \cdot \cos[\overline{\omega} t + \delta_i(t)], \qquad i = x, y, z \tag{2.64}$$

The previously introduced equations (2.53) - (2.54) represented a special case. Here, the amplitudes and initial phase angles of the three component-vibrations are functions of time. Their noise-like properties are determined by the source of the quasi-monochromatic radiation. Their frequency bandwidth is of the order of $\Delta\omega/2$[1].

According to eqs. (2.63) and (2.64), the state of polarization of the quasi-monochromatic wave at our fixed point in space will vary with time. The end point of the electric vector will describe a complicated trajectory. Still, during a time interval that is much shorter than $4\pi/\Delta\omega$ the amplitudes E_{0i} and phases δ_i of the component vibrations will remain essentially constant and the end point of the electric vector will describe an ellipse in space. In other words, the short-term polarization is elliptical. Over longer time intervals the direction in space of the unit normal **n** to the plane of the ellipse may change, as may the handedness, size, shape and orientation of the ellipse in its plane.

In the special case of transverse waves the plane of the ellipse remains normal to the direction of propagation. If we choose the z-axis of our Cartesian coordinate system to be parallel to the wave-vector **k** then $E_z = 0$ at all times and we only need consider the two field components E_x and E_y in eq. (2.63). The handedness, size, shape and orientation of the ellipse may still

---

[1] Compare this to the case of the superposition of two waves of slightly different angular frequencies ω_1, ω_2 and the modulation frequency $\omega_m = (\omega_1 - \omega_2)/2$ of the resulting beats.

change over long (≥4π/Δω) time intervals. Depending on the degree of correlation between the time variation of E_x and E_y the wave might show no preference at all to any specific short-term polarization, in which case it is described as natural or unpolarized[1], or it may show some preference to a specific state of polarization, in which case it is described as partially polarized. Evidently the concepts of polarization and coherence are related in a fundamental way. If the ratio $E_{0y}(t) / E_{0x}(t)$ were constant even though both terms varied, and if $\delta_y(t) - \delta_x(t)$ were constant as well, the wave would be totally polarized[2]. These are exactly the conditions that can be imposed on the wave by letting it pass through a polarizer. In other words, it can be said that a polarizer appropriately correlates the wave's components so that the time interval over which the state of polarization remains constant becomes independent of the bandwidth. For that matter, the light could be white (containing all frequencies) and still totally polarized.

2.3.4 The Stokes vector

Up to this point the description of the state of polarization of an electromagnetic wave was based on the trajectory described by the endpoint of the vector of the electric field strength **E** at some fixed point in space. Another way to represent the state of polarization of a transverse plane wave is through the use of four real quantities S_0, S_1, S_2, and S_3, which are called the Stokes parameters. In terms of the Cartesian components of the transverse electric field the Stokes parameters are defined as follows

$$S_0 = \left\langle E_{0x}^2(t) \right\rangle + \left\langle E_{0y}^2(t) \right\rangle \tag{2.65a}$$

$$S_1 = \left\langle E_{0x}^2(t) \right\rangle - \left\langle E_{0y}^2(t) \right\rangle \tag{2.65b}$$

$$S_2 = 2\left\langle E_{0x}(t) \cdot E_{0y}(t) \cdot \cos\left[\delta_y(t) - \delta_x(t)\right] \right\rangle \tag{2.65c}$$

$$S_3 = 2\left\langle E_{0x}(t) \cdot E_{0y}(t) \cdot \sin\left[\delta_y(t) - \delta_x(t)\right] \right\rangle \tag{2.65d}$$

The angled brackets indicate quantities that have been averaged over a time interval Δt that is

---

[1] An unpolarized wave can also be described as randomly polarized, since it is actually composed of a rapidly varying succession of the different polarization states.

[2] The size of the ellipse of polarization, which is proportional to the energy density of the field at the point of observation, would possibly still vary with time, but the shape and orientation of the ellipse in its plane would not.

long enough to make the averages independent of Δt itself. The Cartesian coordinate system is chosen such that the positive z-direction is parallel to the propagation direction of the wave and $E_z = 0$ at all times because of transversality of the wave.

Remembering that the magnitude of the time-averaged Poynting-vector of a transverse electromagnetic wave is proportional to the square of the amplitude of the electric field, it should be fairly obvious that S_0 is proportional to I_0, the total radiant flux per unit area normal to the propagation direction of the wave. Accordingly, it is always positive. Furthermore, S_1 is proportional to the difference between the radiant flux densities[1] I_x and I_y of the x and y linearly-polarized components of the wave. It is a measure of the preference of the wave to the x linear polarization, to the y linear polarization, or to neither one of these two states and can be positive, negative, or zero, respectively.

Through a coordinate rotation the wave can be resolved into two components that are linearly polarized parallel to the +45° and the –45° bisectors of the x-y coordinate system. It can be shown that S_2 is proportional to the difference between the radiant flux densities $I_{+45°}$ and $I_{-45°}$ corresponding to these wave components. A positive S_2 indicates a stronger preference of the wave to the +45° linear polarization, negative values indicate stronger preference to the –45° linear polarization, and a value of zero states that the wave shows no preference to either one of these two polarization states. In a similar fashion, through an appropriate coordinate transformation, it can be shown that S_3 is proportional to the difference between the radiant flux densities I_{rcp} and I_{lcp} of the right-handed and the left-handed circularly-polarized components of the wave. S_3 will be positive, negative, or zero depending on the preference of the wave to a right-handed circular polarization, a left-handed circular polarization, or to neither one of these two polarization states, respectively.

In summary, we can write for the Stokes parameters of a transverse plane wave (apart from a proportionality constant):

$$S_0 = I_0 = I_x + I_y = I_{+45°} + I_{-45°} = I_{rcp} + I_{lcp} \tag{2.66a}$$

---

[1] The term “radiant flux density” is used in this context for brevity instead of the more exact “radiant flux per unit area normal to the propagation direction of the wave”. Normally, radiant flux (surface) density would be equivalent to the radiometric quantities exitance and irradiance as they were defined in §(2.1.3)-(2.1.4). It is important to remember that these quantities are referenced to a unit area of some arbitrary fixed orientation that, in general, is not normal to the propagation direction of the wave.

$$S_1 = I_x - I_y \tag{2.66b}$$

$$S_2 = I_{+45^\circ} - I_{-45^\circ} \tag{2.66c}$$

$$S_3 = I_{rcp} - I_{lcp} \tag{2.66d}$$

I_x, I_y, I_{+45°, I_{-45°, I_{rcp}, and I_{lcp} can be measured by means of a detector and an ideal variable polarizer that can be adjusted to transmit the x, y, +45°, –45° linear polarizations and the right (rcp)- and left (lcp)-circular polarizations. I_0 can be directly measured with the detector. In other words, the Stokes parameters are observables. This description of polarization is clearly advantageous, since direct observation of the vibration of **E** is impossible at optical frequencies. Instead, measurements made in practice always yield averages over comparatively long time intervals.

From the above discussion on the meaning of the Stokes parameters it follows that the values of S_1, S_2, and S_3 depend on the azimuthal orientation of the (x, y) coordinate axes about the z-axis. S_0, of course, is independent of that orientation, since it corresponds to the total radiant flux density of the wave. The four Stokes parameters are usually grouped together in a 4×1 column vector **S**, called the Stokes vector of the wave:

$$\mathbf{S} = \begin{bmatrix} S_0 \\ S_1 \\ S_2 \\ S_3 \end{bmatrix} \tag{2.67}$$

The effect of a coordinate rotation may then be conveniently expressed as a pre-multiplication of the Stokes vector **S** with a 4×4 rotation matrix **R**. Specifically, if the (x, y) coordinate axes are rotated about the z-axis (whose positive direction is parallel to the wave vector **k**) through an angle α in a counter-clockwise sense when looking against the propagation direction, the rotation matrix is given by

$$\mathbf{R}(\alpha) = \begin{bmatrix} 1 & 0 & 0 & 0 \\ 0 & \cos 2\alpha & \sin 2\alpha & 0 \\ 0 & -\sin 2\alpha & \cos 2\alpha & 0 \\ 0 & 0 & 0 & 1 \end{bmatrix} \tag{2.68}$$

and the Stokes vector **S**′ of the wave in the new coordinate system is:

$$\mathbf{S}' = \mathbf{R}(\alpha) \cdot \mathbf{S} \tag{2.69}$$

This operation can also be interpreted as the effect of an optical rotator on the wave, e.g. a medium exhibiting optical activity that rotates the major axis of the polarization ellipse through an angle α in a clockwise sense when looking against the direction of propagation, while leaving the ellipticity (including its sign) unaffected.

It can easily be verified that the rotation matrix has the following properties:

$$\mathbf{R}^{-1}(\alpha) = \mathbf{R}^{\dagger}(\alpha) = \mathbf{R}(-\alpha) \tag{2.70a}$$

$$\mathbf{R}(\alpha_1 + \alpha_2) = \mathbf{R}(\alpha_1) \cdot \mathbf{R}(\alpha_2) \tag{2.70b}$$

where $\mathbf{R}^{\dagger}$ is the Hermitian adjoint of $\mathbf{R}$, defined as the complex conjugate of the transpose of the matrix.

As stated in §(2.3.3), an unpolarized wave shows no preference to any particular polarization state. It follows from the above discussion that for such a wave $S_1 = S_2 = S_3 = 0$ and the Stokes vector of an unpolarized wave is:

$$\mathbf{S}_{\text{un}} = \begin{bmatrix} S_0 \\ 0 \\ 0 \\ 0 \end{bmatrix} \tag{2.71}$$

The Stokes parameters of a totally polarized wave may be expressed in terms of the azimuth θ and the ellipticity angle ε of the polarization ellipse as:

$$\mathbf{S}_{\text{t.p.}} = \begin{bmatrix} S_0 \\ S_0 \cdot \cos 2\theta \cdot \cos 2\varepsilon \\ S_0 \cdot \sin 2\theta \cdot \cos 2\varepsilon \\ S_0 \cdot \sin 2\varepsilon \end{bmatrix} \tag{2.72}$$

It should be noted here that in the Stokes representation of the state of polarization all information about the absolute phase $\delta(t)$ of the wave is lost.

From eq. (2.72) it can be seen that in the case of a totally polarized wave:

$$S_1^2 + S_2^2 + S_3^2 = S_0^2 \tag{2.73}$$

Furthermore, eqs. (2.71) and (2.73) suggest that for a partially polarized wave

$$S_1^2 + S_2^2 + S_3^2 < S_0^2 \tag{2.74}$$

It can be shown [12] that if several independent (incoherent) quasi-monochromatic waves which propagate in the same direction are superimposed, the Stokes vector of the resulting wave will be equal to the sum of the Stokes vectors of the individual waves. As a special case, a partially polarized quasi-monochromatic wave may be treated as the sum of an unpolarized and a totally polarized component, which are independent of each other:

$$\mathbf{S} = \begin{bmatrix} S_0 \\ S_1 \\ S_2 \\ S_3 \end{bmatrix} = \mathbf{S}_{\mathrm{un}} + \mathbf{S}_{\mathrm{t.p.}} = \begin{bmatrix} S_0 - \left(S_1^2 + S_2^2 + S_3^2\right)^{1/2} \\ 0 \\ 0 \\ 0 \end{bmatrix} + \begin{bmatrix} \left(S_1^2 + S_2^2 + S_3^2\right)^{1/2} \\ S_1 \\ S_2 \\ S_3 \end{bmatrix} \tag{2.75}$$

The ratio of the radiant flux density of the totally polarized component to the total radiant flux density of the wave is defined as the degree of polarization P of the wave:

$$P = \frac{\left(S_1^2 + S_2^2 + S_3^2\right)^{1/2}}{S_0} \tag{2.76}$$

Using this definition we can recast eq. (2.75) to read:

$$\mathbf{S} = \begin{bmatrix} S_0 \\ S_1 \\ S_2 \\ S_3 \end{bmatrix} = \mathbf{S}_{\mathrm{un}} + \mathbf{S}_{\mathrm{t.p.}} = \begin{bmatrix} (1-P)\cdot S_0 \\ 0 \\ 0 \\ 0 \end{bmatrix} + \begin{bmatrix} P\cdot S_0 \\ S_1 \\ S_2 \\ S_3 \end{bmatrix} \tag{2.77}$$

Combining eqs. (2.72) and (2.77) the Stokes vector of a partially polarized quasi-monochromatic wave can now be expressed in terms of the degree of polarization P and the azimuth θ and ellipticity angle ε of the polarization ellipse of the totally polarized component of the wave:

$$\mathbf{S} = S_0 \cdot \begin{bmatrix} 1 \\ P\cdot\cos 2\theta\cdot\cos 2\varepsilon \\ P\cdot\sin 2\theta\cdot\cos 2\varepsilon \\ P\cdot\sin 2\varepsilon \end{bmatrix} \tag{2.78}$$

Often the Stokes vector is normalized with respect to S_0, thus disregarding the information about the total radiant flux density of the wave. The state of polarization is then represented by the three Stokes parameters S_1, S_2, and S_3. They can be interpreted as the coordinates of a point in the (S_1, S_2, S_3) vector subspace with the spherical coordinates (P, 2θ, 90°-2ε). In this Stokes polarization subspace:

- The origin $P = 0$ represents the unpolarized state.
- All points on the unit-sphere ($P = 1$) represent totally polarized states. In fact, this unit-sphere is identical to the Poincaré sphere [11, 13].
- All points inside the unit-sphere ($0 < P < 1$) represent partially polarized states. Points outside the unit sphere ($P > 1$) do not represent any physical state of polarization.

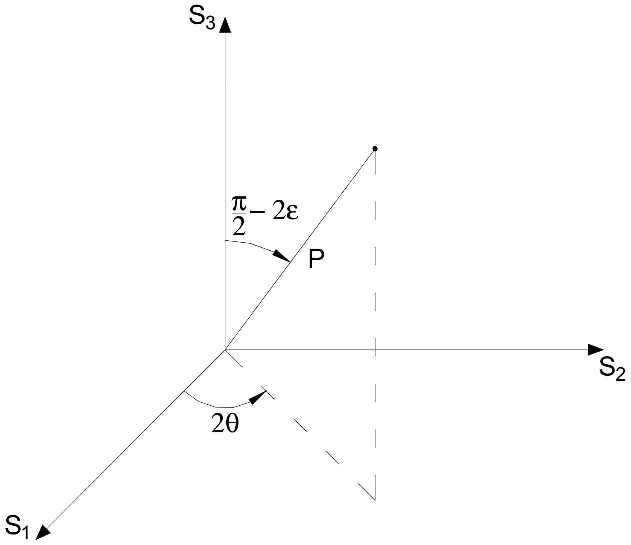

Fig. 2.3: Representation of partially polarized light by a point in the Stokes subspace (S_1, S_2, S_3). P denotes the degree of polarization. θ and ε denote the azimuth and ellipticity angles of the polarization ellipse of the totally polarized component (adapted from [11]).

2.3.5 Propagation of polarized light through an optical system

In this section we consider the interaction of a monochromatic or quasi-monochromatic transverse plane electromagnetic wave with an optical system. Of particular interest is the change in the state of polarization impressed upon the wave by the system. The exact physical mechanism causing this change is of no concern. However, it is presumed that the whole process is linear and frequency-conserving and that the transversality of the wave is preserved throughout.

In the most general case, the wave may be anything from unpolarized to totally polarized. Furthermore, the system may be non-depolarizing or depolarizing. In the case of a non-depolarizing optical system, the degrees of polarization of the incident and outgoing waves, P_i

and P_o respectively, satisfy:

$$P_o \geq P_i \tag{2.79}$$

for all incident states. Consequently, an optical system is depolarizing if the condition

$$P_o < P_i \tag{2.80}$$

is met for at least one incident state of polarization.

The states of polarization of the incident and outgoing waves are represented by two Stokes vectors $\mathbf{S}_i$ and $\mathbf{S}_o$, which are referenced to two space-fixed, right-handed Cartesian coordinate systems (x, y, z) and (x′, y′, z′), respectively. The directions z and z′ are taken parallel to the wave vectors **k** and **k**′ of the incident and outgoing waves. The locations $z = 0$ and $z' = 0$ of the reference coordinate planes are arbitrary, as are the azimuthal orientations of the transverse coordinate axes (x, y) and (x′, y′), along which the incident and outgoing waves are resolved. It is common practice, however, to choose the directions of x and x′ in the plane formed by **k** and **k**′ and the directions of y and y′ parallel to each other. For example, in the case of reflection from a planar boundary between two media the plane formed by the wave vectors of the incident and reflected waves is the plane of incidence (§2.3.6). Accordingly, x and x′ are chosen parallel to the plane of incidence. When there is no angular deviation between the incident and the outgoing wave (**k** and **k**′ are parallel), the two coordinate systems are usually chosen parallel.

Then, in a linear-systems approach the optical system is represented by a real 4×4 matrix **M**, called the Mueller matrix of the optical system. The interaction between the incident wave and the optical system is simply expressed as a pre-multiplication of the input Stokes vector by the system's Mueller matrix:

$$\mathbf{S}_o = \mathbf{M} \cdot \mathbf{S}_i \tag{2.81}$$

In the case of non-depolarizing systems only seven of the sixteen elements of **M** are independent. In the case of depolarizing systems all sixteen elements of the Mueller matrix can be independent [14].

M is, of course, a function of the optical system under consideration. In addition, it depends on:

- the frequency of the incident wave,
- the orientation of the optical system with respect to the direction of the incident wave,
- the locations z = 0 and z′ = 0 of the input and output reference coordinate systems,
- and the azimuthal orientation of the transverse axes (x, y) and (x′, y′) around z and z′.

If the incident wave is split by the optical system into more than one plane waves, each of the emerging waves is associated with its own Mueller matrix.

The effect of a rotation of the input and output coordinate systems on the Mueller matrix **M** can be found by applying eq. (2.69). Let the input coordinate axes (x, y) be rotated through an angle α about the z axis in a counter-clockwise sense when looking against the direction of propagation of the incident wave. At the same time let the output coordinate axes (x′, y′) be rotated through an angle β about the z′ axis in a counter-clockwise sense when looking against the propagation direction of the outgoing wave. If we pre-multiply eq. (2.81) with $\mathbf{R}(\beta)$ and use eq. (2.70a) we can write

$$\mathbf{R}(\beta)\cdot\mathbf{S}_{\mathrm{o}} = [\mathbf{R}(\beta)\cdot\mathbf{M}\cdot\mathbf{R}(-\alpha)]\cdot[\mathbf{R}(\alpha)\cdot\mathbf{S}_{\mathrm{i}}] \qquad (2.82)$$

Recognizing that $\mathbf{R}(\alpha)\cdot\mathbf{S}_{\mathrm{i}}$ is the Stokes vector of the incident wave referenced to the rotated input coordinate system and $\mathbf{R}(\beta)\cdot\mathbf{S}_{\mathrm{o}}$ is the Stokes vector of the outgoing wave referenced to the rotated output coordinate system, it is evident that the new Mueller matrix of the system is given by:

$$\mathbf{M}_{\mathrm{new}} = \mathbf{R}(\beta)\cdot\mathbf{M}\cdot\mathbf{R}(-\alpha) \qquad (2.83)$$

An attractive feature of this approach in describing the interaction of the wave with an optical system is the simplicity with which it can be adapted to multiple-component systems. If the wave passes through a sequence of n optical devices whose Mueller matrices are $\mathbf{M}_1$, $\mathbf{M}_2$,…, $\mathbf{M}_n$, then the combined Mueller matrix $\mathbf{M}_{\mathrm{comb}}$ describing the entire process is simply the product of the individual matrices:

$$\mathbf{M}_{\mathrm{comb}} = \mathbf{M}_{\mathrm{n}}\cdot\mathbf{M}_{\mathrm{n-1}}\cdot\ldots\cdot\mathbf{M}_1 \qquad (2.84)$$

where 1, 2, …,n is the order in which the optical devices are encountered by the wave.

2.3.6 Reflection and refraction of a plane wave at a planar interface between two homogeneous isotropic media

An optical plane wave incident on the planar boundary between two semi-infinite homogeneous optically isotropic media of different optical properties gives rise to a reflected and a refracted (transmitted) wave. It can be shown that the wave-vectors of all three waves lie in the plane of incidence, as specified by the wave-vector of the incident wave and the normal to the boundary. Furthermore, the angle of reflection equals the angle of incidence and the angle of refraction is related to the angle of incidence by:

$$N_1 \cdot \sin\theta_i = N_2 \cdot \sin\theta_t \tag{2.85}$$

where θ_i and θ_t denote the angles of incidence and refraction, respectively, measured from the normal to the interface (fig. 2.4). N_1 is the complex index of refraction of the medium in which the incident and reflected waves propagate, whereas N_2 is the complex index of refraction of the medium in which the refracted wave propagates.

The complex index of refraction N of a medium can be expressed as:

$$N = n - j \cdot k \tag{2.86}$$

where n is the (real) index of refraction and k is the extinction coefficient of the medium. For a transparent (dielectric) medium $k = 0$, whereas for an absorbing medium (conductor) $k \neq 0$.

Let A, R, and T be the complex amplitudes of the electric vectors of the incident, reflected, and transmitted waves, respectively. Each vector is resolved into components parallel (denoted by the subscript p) and perpendicular (denoted by the subscript s) to the plane of incidence. The directions of p and s are chosen such as to form right-handed Cartesian coordinate systems with the direction of propagation, in this order. The Fresnel equations relate the p and s components of the amplitudes of the reflected and transmitted waves to the p and s components of the amplitude of the incident wave:

$$R_p = \frac{N_2\cos\theta_i - N_1\cos\theta_t}{N_2\cos\theta_i + N_1\cos\theta_t} \cdot A_p = \frac{\tan(\theta_i - \theta_t)}{\tan(\theta_i + \theta_t)} \cdot A_p \tag{2.87a}$$

$$R_s = \frac{N_1\cos\theta_i - N_2\cos\theta_t}{N_1\cos\theta_i + N_2\cos\theta_t} \cdot A_s = \frac{-\sin(\theta_i - \theta_t)}{\sin(\theta_i + \theta_t)} \cdot A_s \tag{2.87b}$$

$$T_p = \frac{2 \cdot N_1 \cos\theta_i}{N_1 \cos\theta_t + N_2 \cos\theta_i} \cdot A_p = \frac{2 \cdot \sin\theta_t \cdot \cos\theta_i}{\sin(\theta_i + \theta_t) \cdot \cos(\theta_i - \theta_t)} \cdot A_p \tag{2.87c}$$

$$T_s = \frac{2 \cdot N_1 \cos\theta_i}{N_1 \cos\theta_i + N_2 \cos\theta_t} \cdot A_s = \frac{2 \cdot \sin\theta_t \cdot \cos\theta_i}{\sin(\theta_i + \theta_t)} \cdot A_s \tag{2.87d}$$

In the special case when the incident wave is p-polarized, that is linearly polarized with the plane of vibration parallel to the plane of incidence, the s-component of the electric vector of the incident wave A_s is zero and it follows from eqs. (2.87b) and (2.87d) that the reflected and transmitted waves are also p-polarized. Similarly, when the incident wave is s-polarized the same is true for the reflected and transmitted waves. Thus, the p- and s-polarizations are the eigenpolarizations[1] of reflection and refraction at the planar interface between two optically isotropic media.

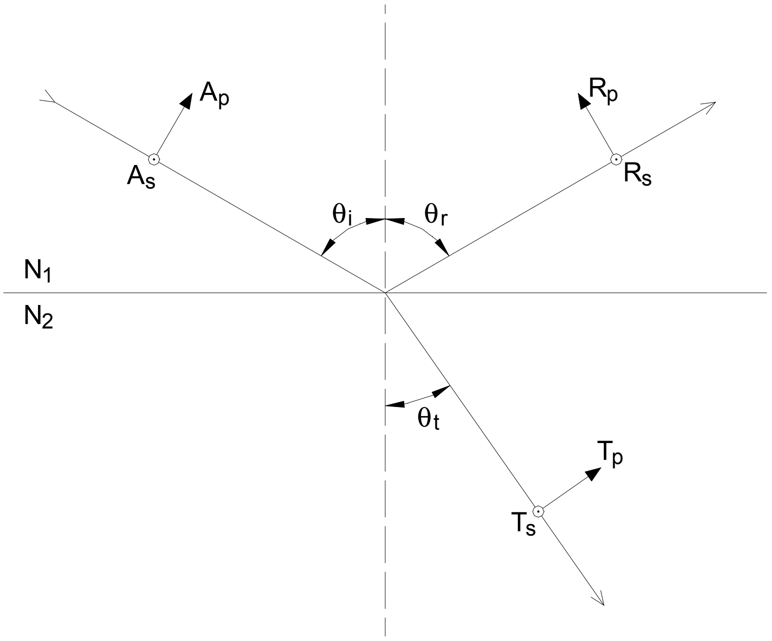

Fig. 2.4: Reflection and refraction of a plane wave at a planar interface. The plane of incidence coincides with the plane of the drawing. The circles with the dot at the center represent vectors pointing out of the plane of the drawing (towards the reader).

When both media are transparent the angles of incidence and of refraction are real (excluding the case of total reflection). It follows then from eqs. (2.87a) - (2.87d) that the phase shifts experienced by the components of the electric vectors of the reflected and transmitted waves are either zero or π. Consequently, if the incident wave is linearly polarized the reflected and

---

[1] The eigenpolarizations of an optical system are the polarizations that pass through the system unchanged. Each linear and non-depolarizing optical system has two eigenpolarizations [14].

transmitted waves are linearly polarized, as well. In general, though, the plane of vibration (azimuth) of the reflected wave will be turned away from the plane of incidence, whereas the plane of vibration of the transmitted wave will be turned toward the plane of incidence, as compared with the incident wave.

When a wave is incident from a dielectric onto an absorbing medium (conductor) it follows from eq. (2.85) that the angle of refraction becomes complex[1]. The phase shifts experienced by the components of the electric vectors of the reflected and transmitted waves will, in general, be different than zero or π. A linearly polarized incident plane wave will then become elliptically polarized upon reflection and refraction at the insulator-conductor interface.

The complex Fresnel reflection coefficients r_p and r_s for the p and s components are defined as:

$$r_p = \frac{R_p}{A_p} = |r_p| \cdot e^{j \cdot \delta_p} \tag{2.88}$$

$$r_s = \frac{R_s}{A_s} = |r_s| \cdot e^{j \cdot \delta_s} \tag{2.89}$$

with

$$|r_p| = \frac{|R_p|}{|A_p|} \quad , \quad \delta_p = \phi_{rp} - \phi_{ip} \tag{2.90}$$

$$|r_s| = \frac{|R_s|}{|A_s|} \quad , \quad \delta_s = \phi_{rs} - \phi_{is} \tag{2.91}$$

$|A_p|$, $|A_s|$, $|R_p|$, $|R_s|$ are the real amplitudes and ϕ_{ip}, ϕ_{is}, ϕ_{rp}, ϕ_{rs} are the initial phase angles of the harmonic vibrations of the electric vectors of the p and s components of the incident and reflected waves.

The ellipsometric angles ψ and Δ are defined in terms of the ratio q of the complex reflection coefficients:

$$q = \frac{r_p}{r_s} = \tan\psi \cdot e^{j \cdot \Delta} \tag{2.92}$$

---

[1] The transmitted wave is then an inhomogeneous wave, because the surfaces of constant amplitude and the surfaces of constant phase will, in general, not coincide [15].

so that

$$\tan\psi = \frac{|r_p|}{|r_s|} = \frac{\dfrac{|R_p|}{|R_s|}}{\dfrac{|A_p|}{|A_s|}} \tag{2.93}$$

and

$$\Delta = \delta_p - \delta_s = (\phi_{rp} - \phi_{rs}) - (\phi_{ip} - \phi_{is}) \tag{2.94}$$

Accordingly, tanψ determines the change in the ratio of the real amplitudes of the orthogonal components (parallel and perpendicular to the plane of incidence) of the electric vector upon reflection. Δ determines the change in the phase difference between the orthogonal components of the electric vector occurring upon reflection of the incident wave at the boundary.

A measurement of ψ and Δ by a suitable technique allows the determination of the complex index of refraction N_2 of the reflecting medium from the complex index of refraction N_1 of the "incident" medium, provided that the angle of incidence θ_i is known [16]. If the medium in which the incident and reflected waves propagate is transparent ($k_1 = 0$), N_2 is related to n_1 by:

$$n_2 - j \cdot k_2 = n_1 \cdot \tan\theta_i \cdot \left[1 - \frac{4q}{(1+q)^2}\sin^2\theta_i\right]^{\frac{1}{2}} \tag{2.95}$$

The complex reflection coefficients r_p and r_s that were defined by eqs. (2.88) and (2.89) are related to the reflectances ρ_p and ρ_s for the p and s polarizations by:

$$\rho_p = \frac{|R_p|^2 \cos\theta_r}{|A_p|^2 \cos\theta_i} = \frac{|R_p|^2}{|A_p|^2} = |r_p|^2 \tag{2.96}$$

$$\rho_s = \frac{|R_s|^2 \cos\theta_r}{|A_s|^2 \cos\theta_i} = \frac{|R_s|^2}{|A_s|^2} = |r_s|^2 \tag{2.97}$$

where θ_r denotes the angle of reflection. ρ_p and ρ_s give the fraction of the energy of the primary wave that is incident upon and reflected off a unit area of the boundary per unit time for the p and s polarizations. Accordingly, the fraction ρ of the total energy of the primary wave that is incident upon and reflected off a unit area of the boundary per unit time is given by:

$$\rho = \frac{\left(|R_p|^2 + |R_s|^2\right)\cdot \cos\theta_r}{\left(|A_p|^2 + |A_s|^2\right)\cdot \cos\theta_i} = \frac{\rho_p \cdot |A_p|^2 + \rho_s \cdot |A_s|^2}{|A_p|^2 + |A_s|^2} \tag{2.98}$$

For normal incidence the distinction between the p and s components disappears and it follows from eqs. (2.87a), (2.87b) and (2.98) that

$$\rho = \rho_p = \rho_s = \left|\frac{N_2 - N_1}{N_2 + N_1}\right|^2 \tag{2.99}$$

For randomly polarized (unpolarized) light it can be shown [17] that

$$\rho_{un} = \frac{1}{2}\left(\rho_p + \rho_s\right) \tag{2.100}$$

For normal incidence, it follows from eqs. (2.99) and (2.100) that

$$\rho_{un} = \rho_p = \rho_s = \left|\frac{N_2 - N_1}{N_2 + N_1}\right|^2 \tag{2.101}$$

When the medium in which the incident and the reflected wave propagate is transparent ($k_1 = 0$) eqs. (2.99) and (2.101) become:

$$\rho_{(un)} = \frac{(n_2 - n_1)^2 + k_2{}^2}{(n_2 + n_1)^2 + k_2{}^2} \tag{2.102}$$

It should be kept in mind that everything that has been mentioned in this section applies exactly only to boundaries that reflect perfectly specularly. Perfectly specular reflection is said to occur when all the reflected flux is concentrated along a single direction that lies in the plane of incidence and satisfies $\theta_i = \theta_r$. In addition, all quantities introduced in this section are frequency-dependent. Consequently, the quantity ρ_{un} that was introduced in eq. (2.100) corresponds to the spectral directional-hemispherical reflectance that was defined in eq. (2.23). The spectral normal-hemispherical reflectance that appears in the energy balance equation for opaque materials (eq. 2.31) corresponds to ρ_{un} for normal incidence in eqs. (2.101) and (2.102).

3 THE MEASUREMENT SYSTEM

3.1 General

The method used in this work was based on rapid resistive self-heating of the wire-shaped specimens by a large current pulse from a capacitor-discharge circuit. Due to the high heating rates achieved in this configuration ($>10^7$ K·s^{-1}) the specimens reached temperatures hundreds of degrees above their melting points before collapsing under the gravitational force, thus allowing the measurement of their liquid properties. Furthermore, because of the short duration of each experiment (less than 100 μs) problems caused by specimen evaporation and by chemical reactions between the specimen and its container were avoided. Heat losses due to heat conduction and radiation could be neglected even at the highest achieved temperatures, making the data analysis much simpler.

A total of seven quantities were measured during each experiment. These were the current through the specimen and the voltage across a defined portion of the specimen, the radiance emitted by the specimen surface, and the four Stokes parameters describing the polarization state of a laser beam that was reflected off the specimen surface. All quantities were measured simultaneously as functions of time. The thermophysical properties finally derived from these measured quantities were the melting point, heat of fusion, electrical resistivity, specific enthalpy, and specific heat capacity of the specimen; the last three properties as functions of temperature.

3.2 The experiment chamber

A new experiment chamber (fig. 3.1), made of 304 stainless steel and capable of holding high vacuum, was designed and built for this work. It was cylindrical in its cross section with an outer diameter of 152.4 mm (6 in), a wall thickness of approximately 3 mm (0.12 in), and an inner height of approximately 347 mm (13.675 in).

It incorporated four viewports, formed by short weld stub flanges that were welded onto the chamber at the appropriate positions. Two of them were used for polarimetry and one for radiation thermometry. The fourth viewport was not used in this work. The two polarimetry-viewports, one for the incident and one for the reflected laser beam, had an inner diameter of approximately 16 mm (0.62 in) and included an angle of 140° (fig. 3.2), as dictated by the requirements for the polarimetric measurement (§3.8). The third and the fourth viewport had a larger diameter of approximately 47.5 mm (1.87 in).

The windows used for polarimetry were made of BK7 optical glass and were 25.4 mm (1 in) in diameter and 3.18 mm (0.125 in) in thickness. The other two windows were cut out of ordinary glass and were approximately 71 mm (2.8 in) in diameter and 3.18 mm (0.125 in) in thickness. Each window was secured between an outer flange and the viewport flange using a hinged clamp with a single wingnut for closure. In order to reduce the mechanical stress introduced into the window material by the tightening of the clamps, elastomer O-rings on both sides of the windows were used for cushioning. This was particularly important for the polarimetry-windows, in order to avoid stress birefringence. At the same time, the inner O-ring (towards the chamber) made the vacuum seal upon compression. The three windows used in the measurements had to be replaced after each experiment, because they were damaged by specimen-debris. The single-wingnut closure of the window clamps facilitated this frequent assembly and disassembly.

A short weld stub flange, similar to the ones that served as viewports, was welded to the chamber near its lower end and was used as the vacuum port. A fine mesh screen installed in this port prevented metal particles produced by the disintegrating pulse-heated specimens from reaching the vacuum line.

Two threaded Swagelok™ tube-fittings were welded onto the top of the chamber. One served as the inlet for the inert gas with which the chamber was filled prior to pulse-heating a specimen (§3.1). A pressure gauge was attached to the other fitting, in order to control the amount of inert gas that was filled in.

The experiment chamber was fastened onto its base using a large banded clamp, which, like the window flanges, was also tightened by means of a single wingnut. The vacuum seal was made by a compressed O-ring. A central high-current feedthrough and two floating-shield, double-ended BNC feedthroughs were welded onto the base, which was permanently attached to the experiment table. The copper conductor of the current feedthrough was separated from the mounting flange (i.e. from the base) by ceramic material that provided electrical insulation. The same applied to the central and the coaxial outside conductors of the BNC feedthroughs. One of the BNC feedthroughs was used for the voltage measurement, whereas the other one was not used in this work.

Access to the specimen holder (fig. 3.3) was gained by removing the chamber from its base. The specimen holder and the specimen itself were at the center of a conducting structure of coaxial geometry (fig. 3.4). The inner conductor of this structure was formed by the current feedthrough, the specimen holder, the specimen, and some additional spacers that completed the connection to a twelve-sided plate at the top. The coaxial outer conductor of the structure was formed by two cylindrical rods and ten bars of rectangular cross section that surrounded the specimen holder. The rods were used to increase the rigidity of the structure. The rods and the bars were attached to the twelve-sided plate at the top and a twelve-sided ring at the bottom. The ring at the bottom was attached to the base of the experiment chamber, which was part of the current path. In a crowbar-mode discharge (§3.4) the current flowed in an upward direction through the base of the chamber and along the bars and rods to the top of this coaxial structure, and returned to the circuit in a downward direction through the specimen and the central current feedthrough.

This geometry was chosen because it offered the advantage of increased symmetry in the electric forces exerted upon the specimen. Since antiparallel currents repel, any small movement of the specimen in a radial direction resulted in a net force back towards the center, where the forces canceled because of the symmetry of the setup. During the experiments, however, three of the surrounding bars were removed because they would otherwise have obstructed the radiometric and polarimetric measurements. A fourth had to be removed to retain the symmetry of the geometry (fig. 3.2). Except, of course, for the specimen, and two supporting rods in the specimen holder that were made of Bakelite, all other components of this coaxial structure were made of brass.

The inner surface of the chamber, as well as the inner surfaces (towards the specimen) of the brass bars surrounding the specimen holder inside the chamber, were sprayed with flat black paint to reduce the impact of internal reflections on the radiometric measurement.

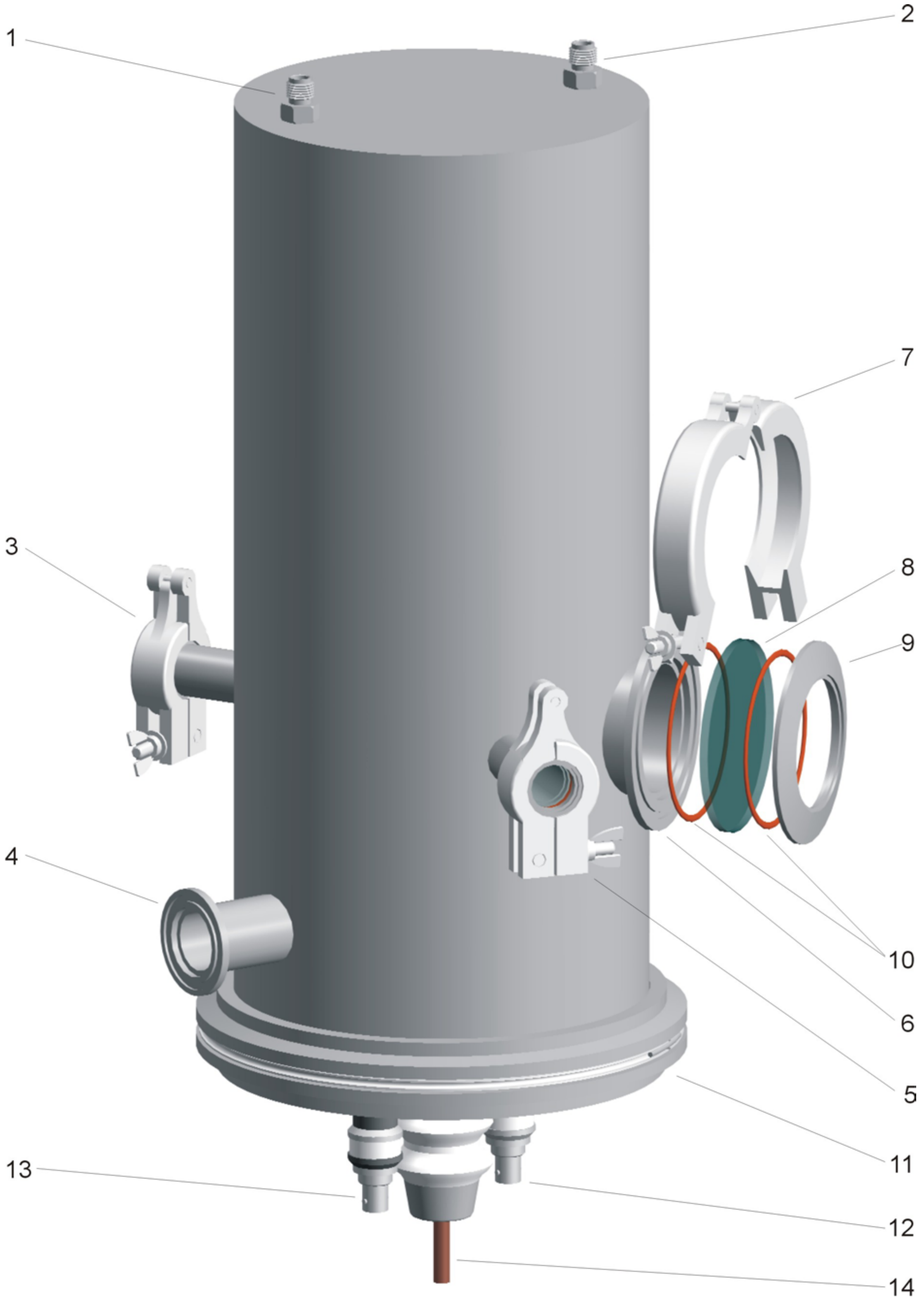

Fig. 3.1: The experiment chamber. 1 port for pressure gauge, 2 gas inlet, 3 polarimetry viewport (incident laser beam), 4 vacuum port, 5 polarimetry viewport (reflected beam), 6 radiometry viewport, 7 hinged clamp, 8 window, 9 outer flange, 10 O-rings, 11 baseplate, 12,13 BNC feedthroughs, 14 current feedthrough.

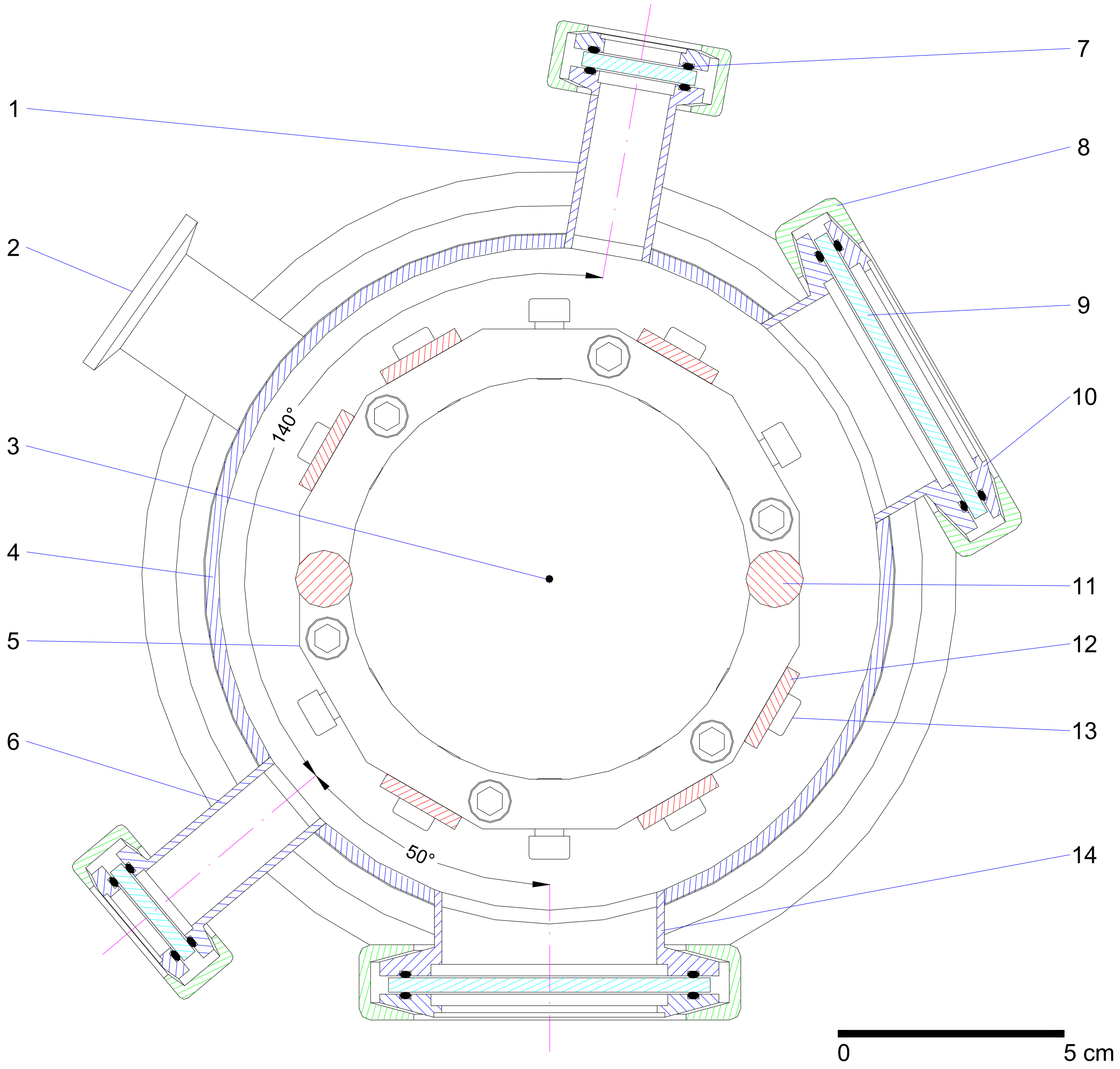

Fig. 3.2: Top view of a cross section through the experiment chamber at the height of the specimen midpoint showing the arrangement of the viewports. 1 polarimetry viewport for the incident laser beam, 2 vacuum port, 3 specimen, 4 chamber, 5 lower twelve-sided ring, 6 polarimetry viewport for the reflected laser beam, 7 elastomer O-ring, 8 viewport clamp, 9 window, 10 outer viewport flange, 11 conducting rod, 12 conducting bar, 13 mounting screw, 14 radiometry viewport. Items 5, 11, and 12 are part of the conducting coaxial structure inside the chamber (§3.2).

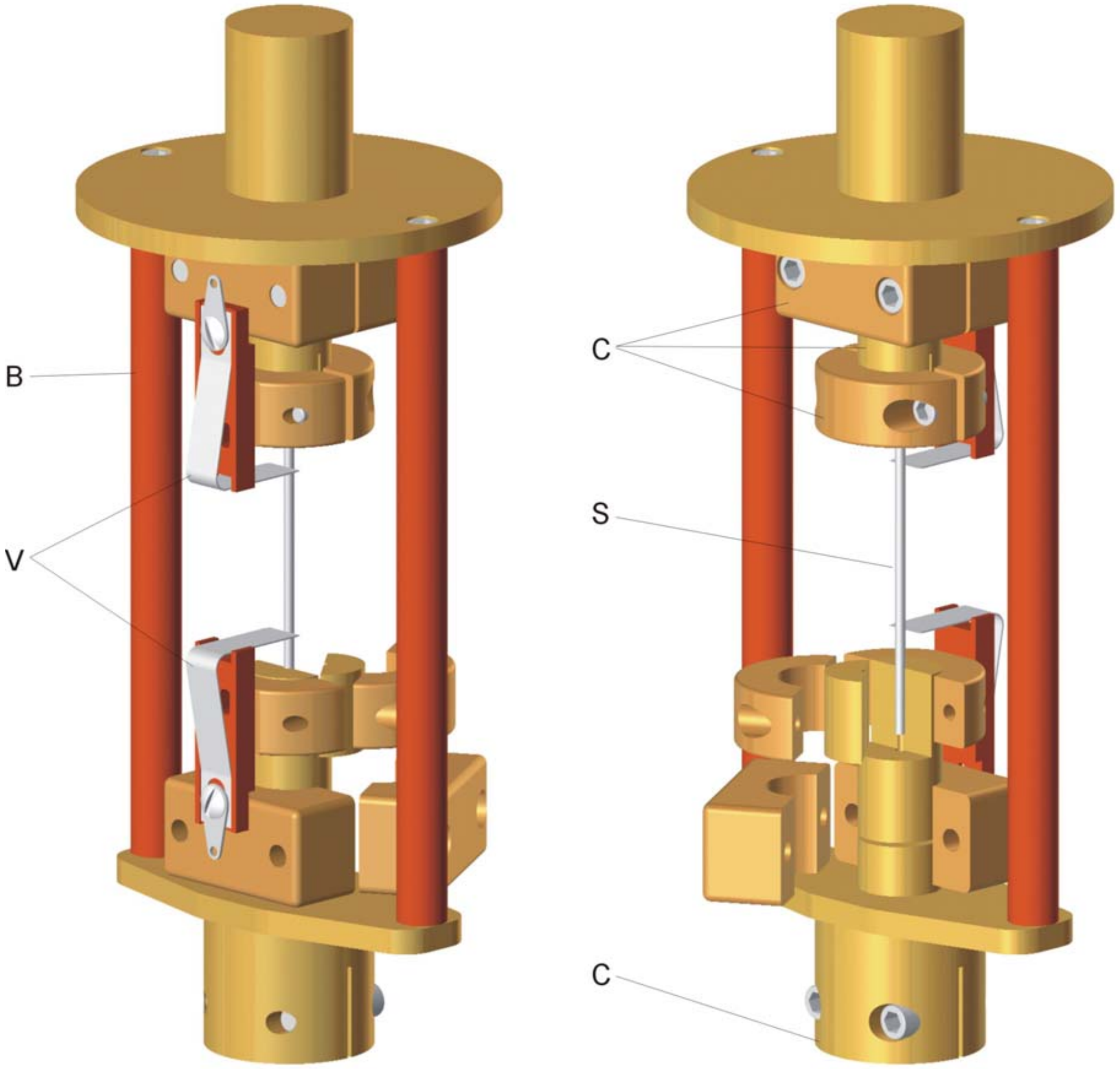

Fig. 3.3: Two views of the specimen holder. B bakelite support rod, V voltage probe, C clamp, S specimen.

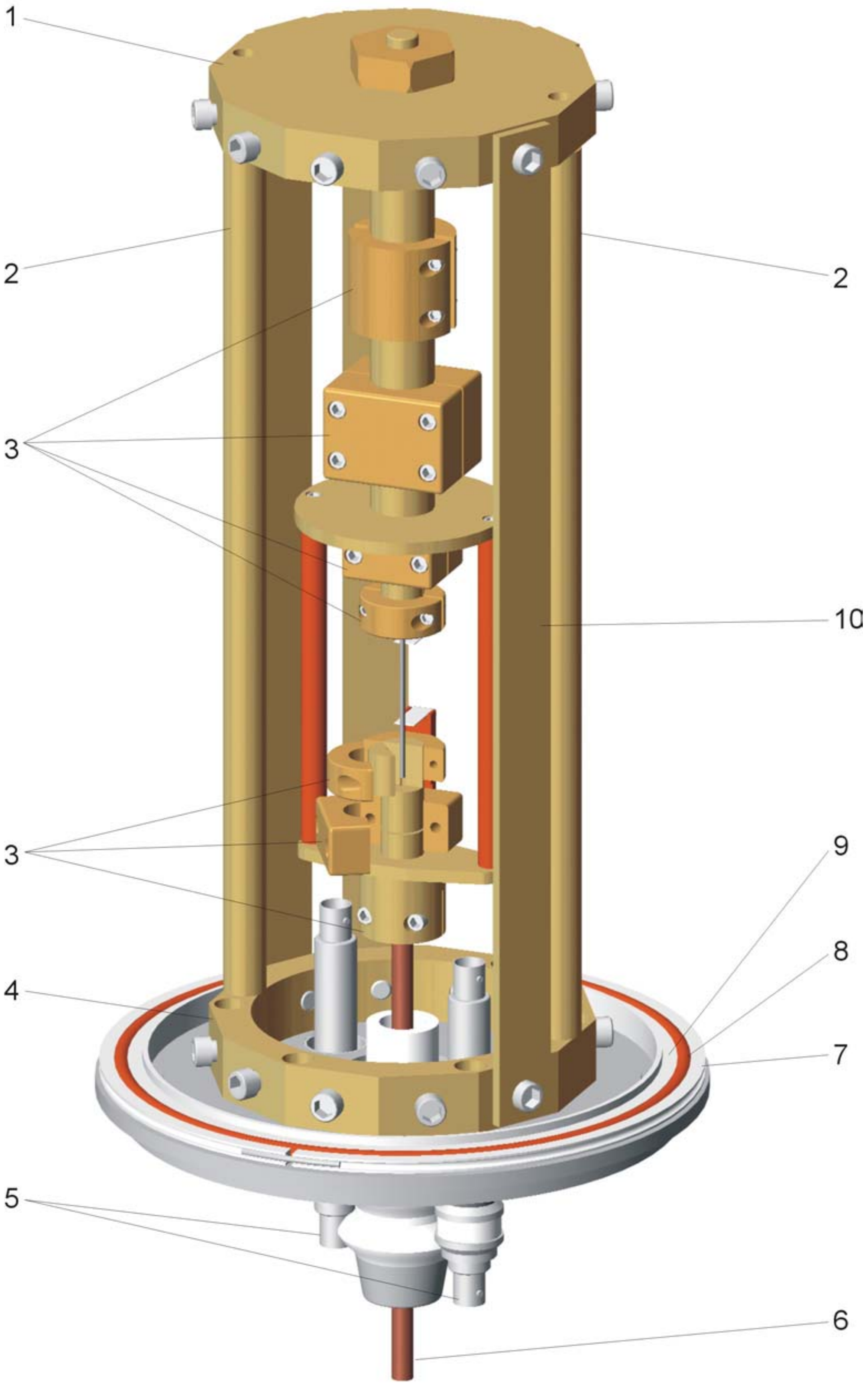

Fig. 3.4: The coaxial geometry inside the experiment chamber. 1 twelve-sided plate, 2 conducting rod, 3 clamp, 4 twelve-sided ring, 5 BNC feedthrough, 6 current feedthrough, 7 retainer ring, 8 O-ring, 9 centering ring, 10 conducting bar.

3.3 The vacuum and inert gas systems

A schematic diagram of the vacuum system is shown in fig. (3.5). A belt-driven, oil-sealed, two-stage, rotary vane high-vacuum pump was used to evacuate the chamber. An exhaust filter was installed to filter oil mist from the pump outlet. On the inlet side of the pump, a coaxial foreline trap with a replaceable steel-wool filter element was used to limit oil-backstreaming into the chamber. From there, a length of thick-walled rubber hose led to a bellows-sealed block valve (V1 in fig. 3.5), and a short piece of rigid PVC tubing connected this valve to the vacuum port of the experiment chamber. A thermocouple vacuum gauge and an up-to-air valve (V4) were mounted on the PVC tubing.

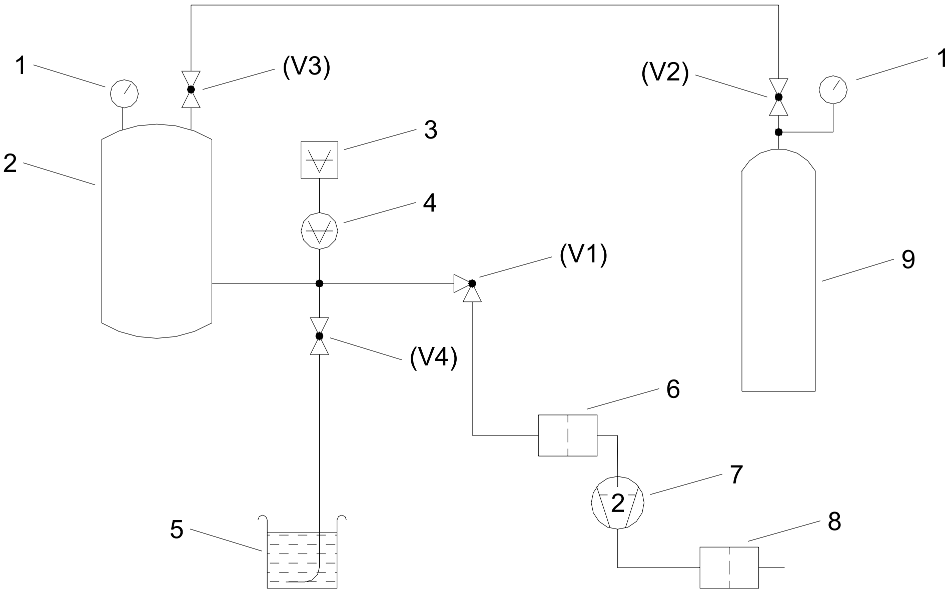

Fig. 3.5: Schematic of the vacuum and inert gas system. 1 pressure gauge, 2 experiment chamber, 3 vacuum gauge readout, 4 thermocouple vacuum gauge, 5 bucket filled with water, 6 foreline trap, 7 two-stage rotary vane pump, 8 exhaust filter, 9 gas cylinder, V1 right-angle valve, V2, V3 inline valves, V4 up-to-air valve.

Once the chamber was evacuated below approximately 0.1 mbar, it was isolated from the pump by closing V1. The chamber was then filled with argon from a pressurized gas cylinder by opening valves V2 at the cylinder and V3 at the top of the chamber. Valve V3 was closed when the pressure gauge at the top of the chamber indicated 1-2 bar above atmospheric pressure. After the specimen was pulse-heated the pressure was released, by opening the up-to-air-valve V4, through a flexible hose whose open end was immersed in water. This way, the finer particles from the disintegrated specimen, which managed to pass through the mesh screen in the vacuum port of the chamber, were filtered from the exiting gas.

3.4 *The discharge circuit*

A functional diagram of the pulse-heating system is shown in fig. (3.6). The capacitor-discharge circuit consisted of a 24 kJ capacitor bank (120 µF, 20 kV), two switches and the specimen. Both switches were high-voltage, mercury-vapor ignitron tubes. The circuit represented an underdamped RLC-circuit with a nominal oscillation frequency of 10 kHz (upper trace of fig. 3.7). To prevent the reversal of the current through the specimen, the circuit was operated in the crowbar-mode. In this mode of operation the switch in parallel with the specimen (Crowbar-ignitron) was closed just after the current reached its first peak, thus creating an electrical short across the specimen. This allowed the energy that had been stored magnetically during the initial rise of the current to be returned to the circuit as unidirectional current through the specimen (lower trace of fig. 3.7).

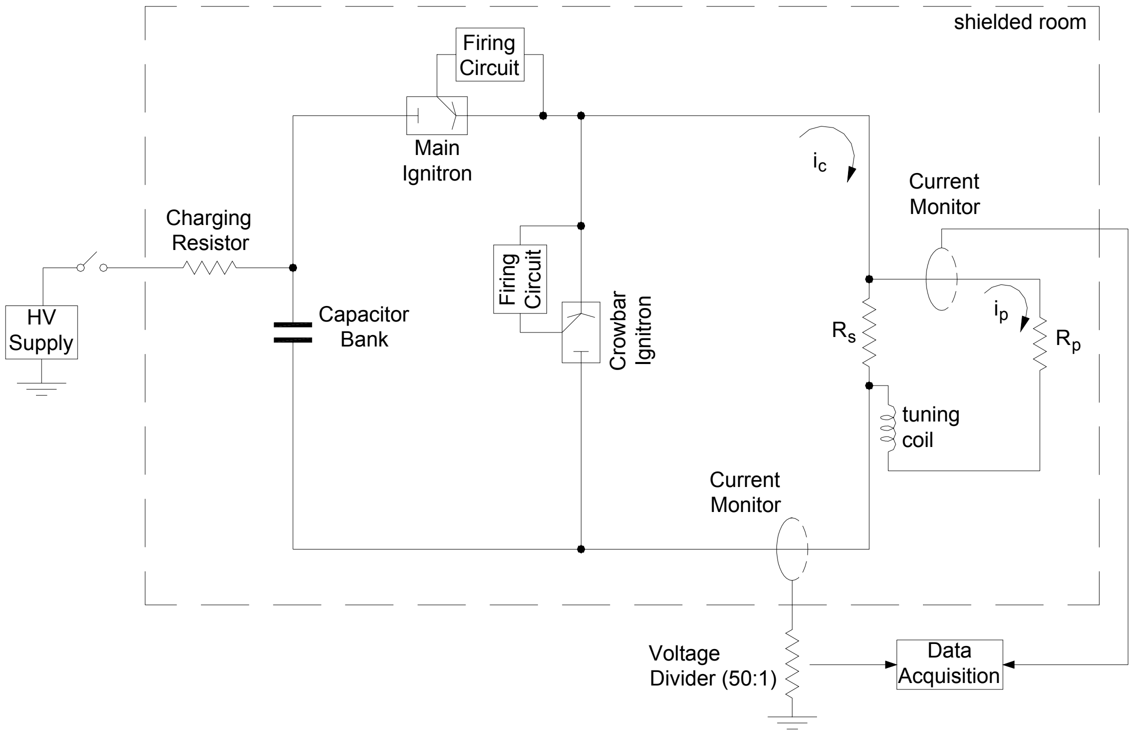

Fig. 3.6: Schematic diagram of the capacitor-discharge circuit including the current and voltage measuring circuits.

High rates of current change (dI/dt) are always associated with electromagnetic noise. To minimize the effects of electromagnetic interference (EMI) on the measurements, the capacitor discharge circuit was located inside a shielded room. Tri-axial cables or coaxial cables inside copper tubes, combined with appropriate feedthroughs, were used to transmit all electrical signals to the data acquisition instrumentation outside the shielded room.

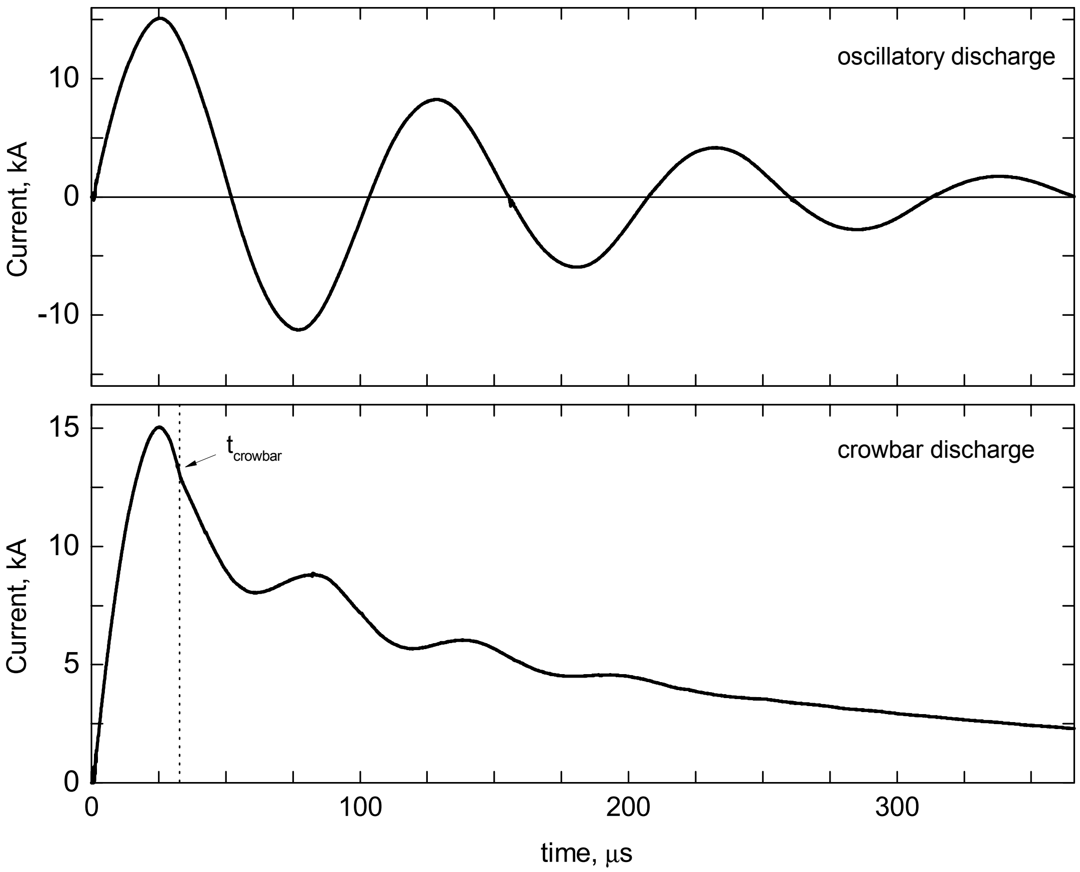

Fig. 3.7: Electrical current vs. time for oscillatory (upper) trace and crowbar (lower trace) capacitor-discharge conditions.

3.5 Current measurement

The current through the specimen was measured using a wide-band current monitor. Such a current monitor comes in form of a loop. The current-carrying conductor passes through the hole of the loop and the output of the monitor is sustained by the changing level of the magnetic flux in its ferromagnetic core. A current monitor is electrically isolated from the circuit being monitored. This isolation provides increased protection to both equipment and personnel, eliminates to a large extent problems associated with ground loops, and minimizes the impact on the current being measured by adding virtually no load to the discharge circuit. In addition, toroidal construction and appropriate shielding makes the current monitor sufficiently immune to stray electromagnetic fields for use near a capacitor-discharge circuit.

Two current-monitor models were used in this work, depending on the peak current to be measured. One was rated to 50 kA, with a nominal sensitivity of 10 $\mathrm{mV \cdot A^{-1}}$, and the other to 100 kA, with a nominal sensitivity of 5 $\mathrm{mV \cdot A^{-1}}$. In both cases, they were terminated at the data acquisition instrumentation with a 50 Ω non-inductive voltage divider of nominal ratio

50:1. Since the equivalent circuit of the current monitors was that of a voltage source in series with a 50 Ω resistor, terminating them with a 50 Ω voltage divider effectively halved their output voltage. Accurate values of their sensitivity and of the divider ratio were obtained by calibration.

3.6 Voltage measurement

The voltage u_s across the specimen consisted of a resistive and several inductive components:

$$u_s = R_s \cdot i_s + L_s \cdot \frac{di_s}{dt} + i_s \cdot \frac{dL_s}{dt} + M \cdot \frac{di_s}{dt} \tag{3.1}$$

i_s denotes the current through the specimen, R_s the specimen resistance, L_s the specimen self-inductance, and M the mutual inductance between the discharge circuit and the voltage-measuring circuit.

According to [18], the self-inductance L (in Henrys) of a solid, round, straight, and nonmagnetic conductor of radius r and length *l* can be approximated by:

$$L = 2\times10^{-7} \cdot l \cdot \left[\ln\frac{2 \cdot l}{r} - \frac{3}{4} \right] \tag{3.2}$$

For l = const., it follows that:

$$|dL| = 2\times10^{-7} \cdot l \cdot \frac{|dr|}{r} \tag{3.3}$$

Differentiation of eq. (3.3) with respect to time yields for the third term on the right side of eq. (3.1):

$$i_s \cdot \frac{|dL_s|}{dt} = 2\times10^{-7} \cdot l \cdot \frac{|dr_s|}{r_s} \cdot \frac{i_s}{dt} \tag{3.4}$$

where r_s is the specimen radius.

In a typical pulse-heating experiment with niobium in which a specimen was heated to 3200 K in 90 µs, the average current through the specimen was approximately 27 kA and the average voltage across a specimen length of 23 mm was 210 V. According to [19], the volume expansion V/V_0 of niobium at 3200 K is 1.18, with V_0 denoting the volume at room temperature. Converting this to a purely radial expansion (see footnote 3 on page 86) we obtain a value of 0.086 for $\Delta r_s/r_{s,0}$ at 3200 K, with $r_{s,0}$ denoting the specimen radius at room temperature. Substitution of these values into eq. (3.4) yields $i_s \cdot |\Delta L_s|/\Delta t = 0.12$ V, which is less than 0.06% of 210 V. Therefore, this voltage component could be neglected without introducing a considerable error.

In actuality, the voltage was not measured across the entire specimen. The above mentioned 23 mm corresponded to the ‘effective’ specimen length, which was defined by two shallow knife marks (grooves) that were made on the middle portion of each specimen. The exact distance of the marks was measured using a traveling microscope. Tantalum strips (6.4 mm wide and 0.25 mm thick), that had been sharpened to a knife-edge on one end, were placed on the knife marks to serve as voltage probes, with the sharp end touching the specimen (fig. 3.3). Some tension was applied to the voltage probes to ensure good electrical contact.

The voltage-measuring circuit was connected in parallel across the specimen (fig. 3.6). It consisted of a resistor in series with a rotatable tuning-coil that was placed below the experiment chamber, near the central current feedthrough. The voltage across this parallel path was equal to the voltage across the specimen. Applying Kirchhoff’s voltage law to the loop formed by the parallel path and the specimen, and using eq. (3.1) for the voltage across the specimen, we can write

$$R_s \cdot (i_c - i_p) + L_s \cdot \frac{d(i_c - i_p)}{dt} + M \cdot \frac{di_c}{dt} = R_p \cdot i_p + L_p \cdot \frac{di_p}{dt} \tag{3.5}$$

where the loop currents i_c and i_p on the discharge-circuit-side and on the parallel-path-side, respectively, have been introduced (fig. 3.6). R_p and L_p are the total resistance and the total self-inductance of the parallel path.

It can be seen from eq. (3.5) that the inductive voltage components cancel if M satisfies

$$(L_s + M) \cdot \frac{di_c}{dt} = (L_s + L_p) \cdot \frac{di_p}{dt} \tag{3.6}$$

In this case we obtain the simple expression

$$R_s \cdot (i_c - i_p) = R_p \cdot i_p \tag{3.7}$$

In other words, the resistive component of the voltage across the specimen $R_s \cdot (i_c - i_p)$ can be determined from i_p and R_p.

If we rearrange terms in eq. (3.7),

$$R_s \cdot i_c = \left(R_s + R_p\right) \cdot i_p \tag{3.8}$$

it becomes apparent that when eq. (3.6) is satisfied, the current i_p in the parallel path "follows" the current i_c in the main discharge circuit; in other words the two currents are in phase.

The mutual inductance M between the voltage-measuring circuit and the discharge circuit was varied by rotating the tuning coil with respect to the direction of the magnetic field produced by the main circuit. This, in effect, changed the magnitude of the voltage that was induced in the coil by changes in the magnetic field, resulting from di_c/dt. The induced voltage was a maximum when the axis of the coil was parallel to the direction of the magnetic field. In order to find the position for which eq. (3.6) was satisfied, each experiment was preceded by a few trial discharges in the oscillatory mode, in which i_c and i_p were recorded. To avoid excessive heating of the specimen the capacitor bank was charged to the lowest possible voltage that still ignited the ignitron-switch. The tuning coil was readjusted after each trial until i_p was in phase with i_c. Usually, one or two trials were sufficient.

Combining eqs. (3.6) and (3.8) we arrive at the following expression for M, when i_c and i_p are in phase:

$$M = \frac{R_s \cdot L_p - R_p \cdot L_s}{R_s + R_p} = \frac{\left(R_s/R_p\right) \cdot L_p - L_s}{\left(R_s/R_p\right) + 1} \approx \frac{R_s}{R_p} \cdot L_p - L_s \tag{3.9}$$

The last step is justified, considering the fact that R_p was approximately 20 Ω, whereas the resistance R_s of the Nb and Ti specimens at the highest temperatures did not exceed 12 mΩ and 20 mΩ, respectively.

Equation (3.9) was used to roughly estimate the effect of R_s on the value of M that was required for i_c and i_p to be in phase. The self-inductance L_s of the specimen was computed using eq. (3.2). The self-inductance L of the tuning coil was obtained from

$$L = 0.001 \cdot F \cdot d \cdot N^2 \tag{3.10}$$

where L is in µHenry, d is the coil-diameter in cm, N is the number of turns, and F is a shape-factor [18]. Assuming that the total self-inductance L_p of the voltage-measuring circuit was determined by the self-inductance of the tuning coil, it was estimated that a six-fold increase in R_s during a typical pulse-heating experiment with niobium caused a change of 4% in M. Similarly, a more than three-fold increase in R_s during a typical pulse-heating experiment with titanium caused a change of 6% in M. Thus, it can be said that M is a relatively weak function of specimen resistance.

The current i_p through the voltage-measuring circuit was measured with a current monitor, similar to the one that was used to measure the current i_c through the main discharge circuit (§3.5). By passing i_p twice through the current monitor the output signal was doubled yielding a nominal sensitivity of 0.2 $V \cdot A^{-1}$. Accurate values for the sensitivity of the current monitor and the resistance of the parallel path were obtained by calibration.

3.7 Radiation thermometry

3.7.1 The radiation thermometer

The radiance temperature of the pulse-heated specimens was measured using a single-wavelength radiation thermometer built by E. Kaschnitz in 1993. Its main components were a pair of identical plano-convex achromatic lenses with a combined effective focal length of 160 mm as the objective, an interference filter as the wavelength-selecting element, and a rectangular field stop of 9.8 mm height and 0.5 mm width. This corresponded exactly to the target size, i.e. the size of the area viewed on the specimen, since the magnification of the instrument was unity. The light from the specimen was coupled into an optical fiber light guide and transmitted to a silicon PIN photodiode. The photodiode and the signal amplifying electronics were contained in a separate box that shielded them against EMI. The amplifying electronics had a low-gain and a high-gain output. The nominal radiance temperature ranges for the two outputs were 1600 to 2800 K and 1400 to 2200 K, respectively. Two coaxial cables inside copper tubes of adequate wall thickness, again for the purpose of shielding against EMI, transferred the output signals to the data acquisition instrumentation outside the shielded room.

3.7.2 Radiance temperature calibration

The radiation thermometer was calibrated in-situ against a gas-filled tungsten-filament reference lamp. The lamp had been previously calibrated against the NIST Photoelectric Pyrometer [20] by the NIST Optical Technology Division and was issued a calibration certificate reporting filament currents for thirteen radiance temperatures at 655.3 nm in the range of 1000 to 2200°C in steps of 100°C[1]. A quadratic function of radiance temperature vs. filament current was fitted to these values in the range of 1800 to 2200°C (fig. 3.8a). The deviation of the fit from the actual values was less than 0.4°C (fig. 3.8b). All temperatures reported in this work are based on the International Temperature Scale of 1990 (§2.2.1).

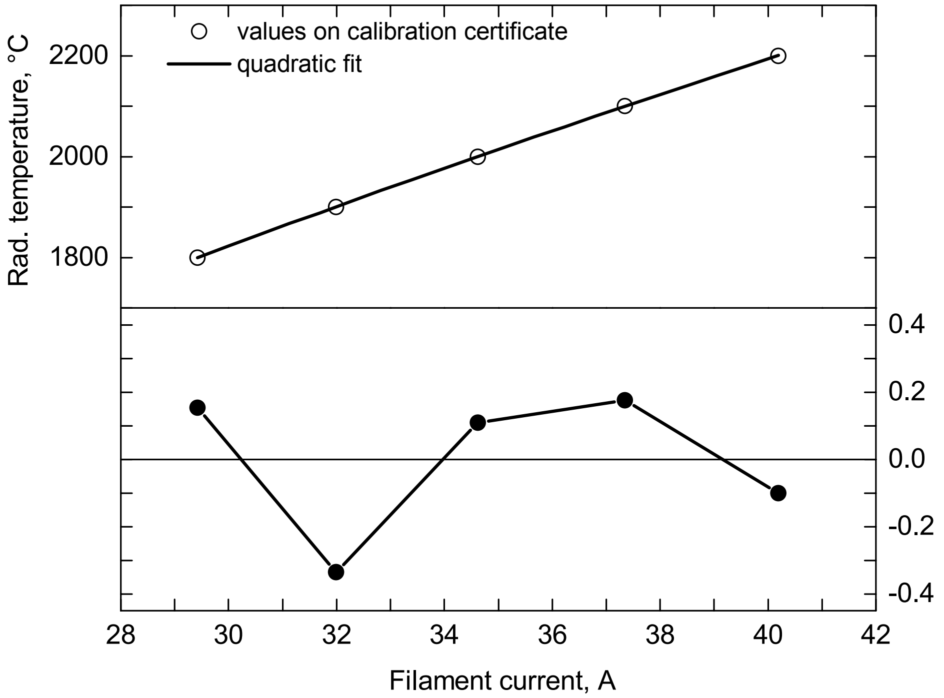

Fig. 3.8: (a) Lamp radiance temperature at 655.3 nm vs. lamp filament current.
(b) Deviation of the quadratic fit from the values reported on the lamp calibration certificate.

The radiation thermometer was calibrated at 2073.15 K and at 2373.15 K in radiance temperature. When the lamp current was not identical to the values corresponding to these two temperatures as specified on the calibration certificate, the actual radiance temperature of the filament was computed using the quadratic fit. It can be seen from fig. (3.8b) that at 1800°C and 2100°C the deviation of the fit from the values on the calibration certificate was less than 0.2°C. The lower-temperature calibration was used for the titanium measurements and the higher-temperature calibration for the niobium measurements. The lamp was aligned according to the procedure outlined in [21]. Since the measurement of specimen temperature

---

[1] Because lamp calibration certificates issued at NIST report temperatures in degrees Celsius, this unit will be used in a limited manner in this section.

involved focussing the radiometer on the specimen through an experiment chamber window, an identical window was interposed between the reference lamp and the radiometer during calibration.

Having calibrated the radiometer at T_0, an unknown specimen radiance temperature T_λ was computed using eq. (2.50), which when solved for T_λ yields[1]:

$$T_\lambda = \frac{c_2}{n \cdot \lambda_{T_0 - T_\lambda}} \cdot \frac{1}{\ln\left\{1 + \frac{S(T_0)}{S(T_\lambda)} \cdot \left[\exp\left(\frac{c_2}{n \cdot \lambda_{T_0 - T_\lambda} \cdot T_0}\right) - 1\right]\right\}} \tag{3.11}$$

where $\lambda_{T_0\text{-}T_\lambda}$ is the mean effective wavelength between T_0 and T_λ. $S(T_0)$ and $S(T_\lambda)$ denote the radiometer output signal when viewing a target at T_0 and T_λ, respectively.

3.7.3 Effective wavelength calibration

In order to be able to compute $\lambda_{T_0\text{-}T_\lambda}$, the limiting effective wavelength λ_T of the radiation thermometer as a function of temperature had to be determined. For this, the instrument had to be calibrated in terms of its spectral-radiance responsivity $R_L(\lambda)$, as follows from eq. (2.46). This quantity was defined in eq. (2.40), which is repeated here for convenience:

$$R_L(\lambda) = b \cdot G \cdot \tau(\lambda) \cdot R_\Phi(\lambda) \tag{3.12}$$

For brevity, the double integral over the spatial parameters A and ω has been replaced by the constant G and these parameters have been omitted, since attention is now focused on the dependence of R_L on the spectral parameter λ. The spectral behavior of R_L is determined by the spectral transmittance $\tau(\lambda)$ of the optical components in the radiometer (primarily the interference filter) and the detector spectral-flux responsivity $R_\Phi(\lambda)$.

An existing, specially designed automated monochromator system [22] was used to measure $\tau(\lambda)$, up to a constant multiplicative factor. The main component of the system was a computer-controlled, wide-aperture, grating monochromator combined with a filter wheel for stray light reduction and unwanted order elimination. Immediately prior to the $\tau(\lambda)$-measurement the monochromator was calibrated using the 730 nm line of a low pressure mercury lamp. As a check of this calibration, several more of the mercury-lines were scanned

---

[1] Keeping in mind the simplifying assumptions that led to eq. (2.39).

in the range 400 to 1100 nm. The mercury lamp was then replaced by a gas-filled tungsten-filament lamp.

An essential requirement in the measurement of τ(λ) is that the illumination of the interference filter and the other optical components in the radiometer be identical to that during temperature measurements, since the spectral transmittance of interference filters is strongly dependent upon the particular direction of the incident radiance. In the monochromator system described here, the radiance from the tungsten-filament lamp was focused on the entrance slit of the monochromator by a pair of achromats similar to those used in the radiometer objective. The radiometer, in turn, was focused on the exit slit of the monochromator. The radiometer output signal was recorded as a function of wavelength as the monochromator scanned the range from 570 nm to 740 nm in steps of 1 nm.

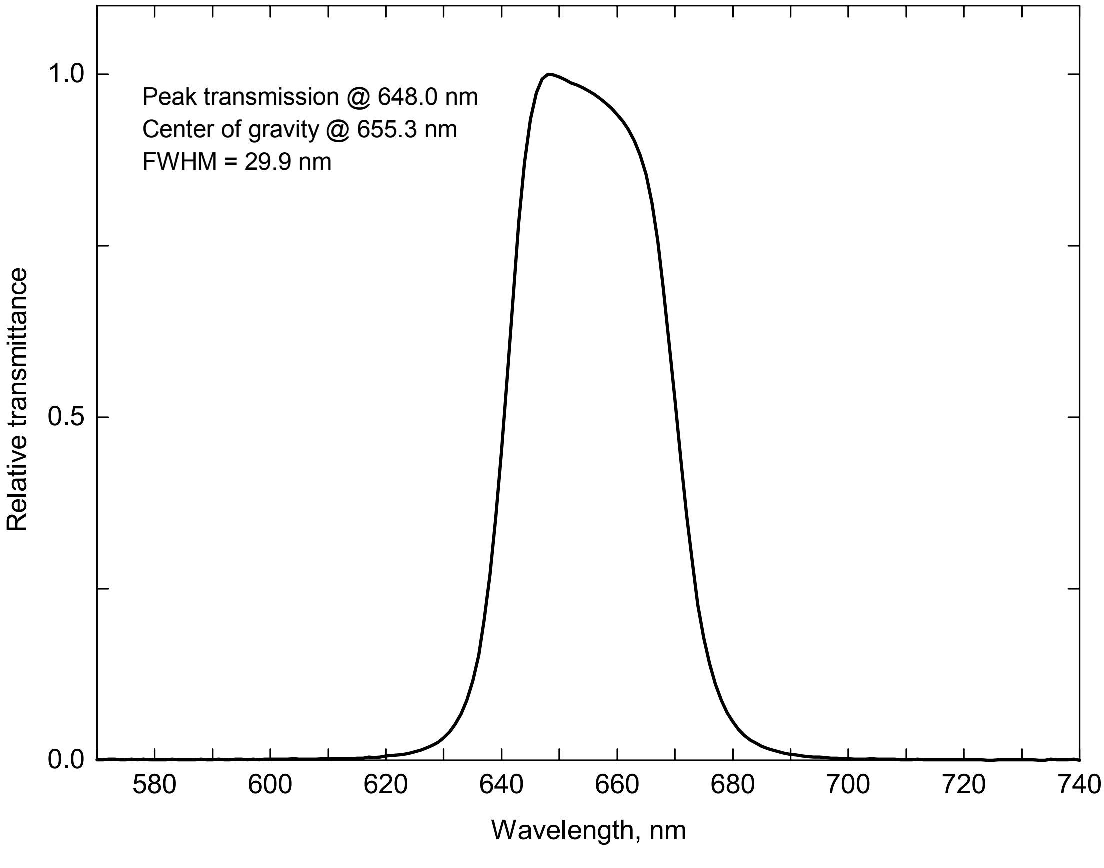

Fig. 3.9: Relative, peak-normalized spectral transmittance τ(λ) of the optical components in the radiation thermometer.

In a second step, a stand-alone silicon photodiode was mounted on the monochromator exit slit and the photodiode current was recorded as the monochromator scanned the same spectral range. The peak-normalized ratio of the radiometer output signal to the stand-alone photodiode signal represented the (relative) peak-normalized spectral transmittance curve $\tau_{rel}(\lambda)$ of the optical components in the radiometer (fig. 3.9). Each scan was preceded by a measurement of the 'dark' signal (with a shutter between the lamp and the monochromator in the 'closed' position) that was then subtracted from the 'bright' signal to account for the zero-offset of the radiometer and the dark current of the stand-alone photodiode.

By substituting eq. (3.12) into eq. (2.39) the radiometer signal recorded in the first monochromator scan may be expressed as:

$$S(\lambda) = b \cdot G \cdot \tau(\lambda) \cdot R_{\Phi}(\lambda) \cdot L_{\lambda}(\lambda) \cdot \Delta\lambda_m \tag{3.13}$$

λ denotes the monochromator setting and $\Delta\lambda_m$ the wavelength interval around λ of significant transmission through the monochromator. $L_\lambda(\lambda)$ is the lamp spectral radiance at λ. The integral of eq. (2.39) was replaced in eq. (3.13) by a simple product, assuming that $\tau(\lambda)$, $R_\Phi(\lambda)$, and $L_\lambda(\lambda)$ were constant throughout the narrow[1] interval $\Delta\lambda_m$.

Similarly, the signal of the stand-alone photodiode recorded in the second scan may be expressed as:

$$S_{ph}(\lambda) = G_{ph} \cdot R_{\Phi}(\lambda) \cdot L_{\lambda}(\lambda) \cdot \Delta\lambda_m \tag{3.14}$$

G_{ph} is a factor taking into account the geometry of illumination of the photodiode, similar to the factor G in eq. (3.12).

The ratio of $S(\lambda)$ to $S_{ph}(\lambda)$ is proportional to $\tau(\lambda)$:

$$\frac{S(\lambda)}{S_{ph}(\lambda)} = \frac{b \cdot G}{G_{ph}} \cdot \tau(\lambda) \tag{3.15}$$

Normalization of this ratio with respect to its peak value yields the relative, peak normalized spectral transmittance of the optical components in the radiometer:

$$\tau_{rel}(\lambda) = \frac{\tau(\lambda)}{\tau(\lambda_{max})} \tag{3.16}$$

λ_{max} denotes the wavelength of peak transmittance.

---

[1] A measure for $\Delta\lambda_m$ when the entrance and exit slits are equal in width, is the double spectral slit width, $2 \cdot \Delta\lambda_w$, of the monochromator. $\Delta\lambda_w$ is defined in [23] as $\Delta x \cdot (dx/d\lambda)^{-1}$, with Δx denoting the width of the exit slit and $dx/d\lambda$ denoting the linear dispersion of the instrument. The actual values for Δx and $(dx/d\lambda)^{-1}$ were 0.25 mm and 3.0 $nm \cdot mm^{-1}$, respectively, yielding 1.5 nm for $2 \cdot \Delta\lambda_w$ [24].

Substitution of $\tau(\lambda)$ from eq. (3.16) into eq. (2.46) yields for the limiting effective wavelength of the radiometer as a function of temperature:

$$\frac{1}{\lambda_T} = \frac{\int\limits_{\Delta\lambda} \frac{1}{\lambda} \cdot \tau_{rel}(\lambda) \cdot R_\Phi(\lambda) \cdot L_{\lambda,b}(\lambda, T) \cdot d\lambda}{\int\limits_{\Delta\lambda} \tau_{rel}(\lambda) \cdot R_\Phi(\lambda) \cdot L_{\lambda,b}(\lambda, T) \cdot d\lambda} \qquad (3.17)^1$$

The detector flux-responsivity $R_\Phi(\lambda)$ was approximated within the integration limits by a linear function of wavelength tangent to the responsivity curve at λ_{max}

$$R_\Phi(\lambda) = R_\Phi(\lambda_{max}) + a \cdot (\lambda - \lambda_{max}) \qquad (3.18)$$

with $R_\Phi(\lambda_{max}) = 0.45\ A \cdot W^{-1}$ and $a = 1\ A \cdot W^{-1} \cdot \mu m^{-1}$. These values were obtained from the photodiode manufacturer's data sheet.

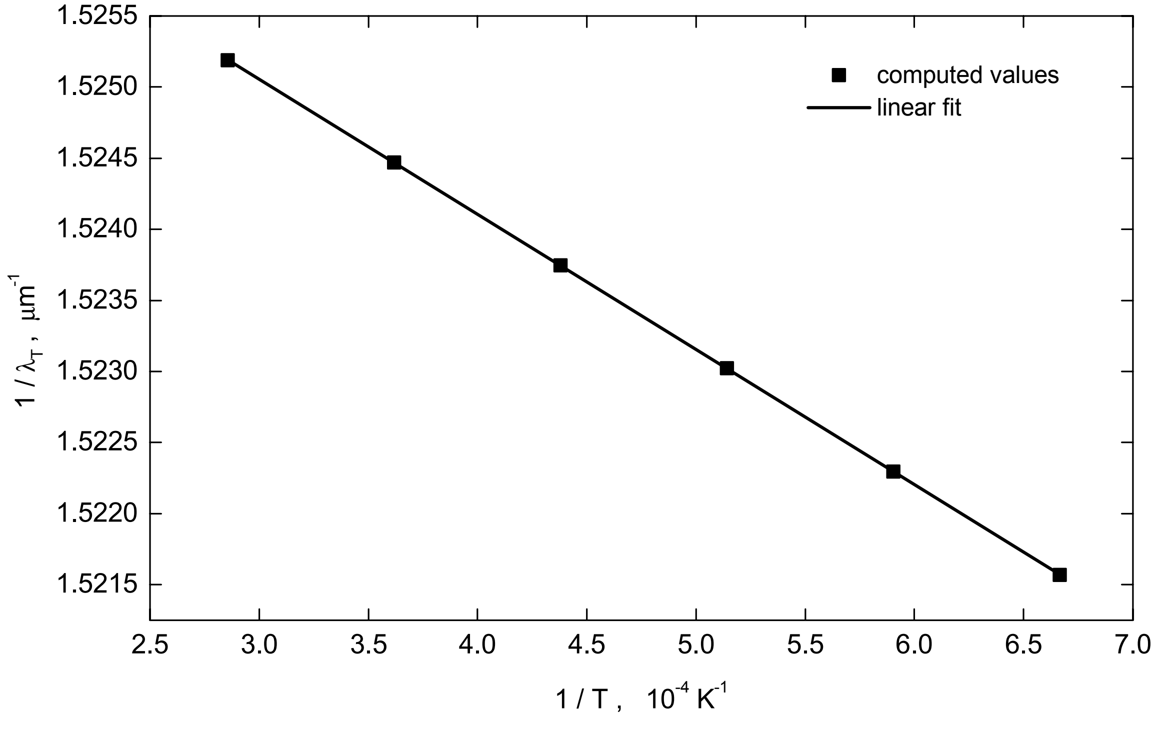

Fig. 3.10: The inverse limiting effective wavelength of the radiation thermometer as a function of inverse temperature.

Figure (3.10) shows the inverse limiting effective wavelength of the radiometer, computed at six temperatures in the range 1500 to 3500 K. A linear function of inverse temperature was fitted to the computed values of inverse limiting effective wavelength:

---

[1] $\Delta\lambda$ is the wavelength interval of significant instrument responsivity and should not be confused with $\Delta\lambda_m$, which denotes the wavelength interval of significant monochromator transmittance.

$$\frac{1}{\lambda_T} = \left(1.527906\,\mu m^{-1}\right) - \left(9.502448\,\frac{\mu m^{-1}}{K^{-1}}\right) \cdot \frac{1}{T} \qquad (3.19)$$

The largest deviation of the fit from the computed values of $1/\lambda_T$ was less than $4\times10^{-6}\ \mu m^{-1}$, corresponding to a deviation of less than 0.002 nm in λ_T.

Using eqs. (2.47) and (3.19), $\lambda_{T_0\text{-}T_\lambda}$ was computed as a function of target radiance temperature T_λ in the range 1500 to 3000 K, for both calibration temperatures $T_0 = 2073.15$ K and $T_0 = 2373.15$ K (fig. 3.11).

The variation of $\lambda_{T_0\text{-}T_\lambda}$ over the entire temperature measurement range was considered small. Therefore, specimen radiance temperature was computed from the measured radiance using a constant value of 656.3 nm for $\lambda_{T_0\text{-}T_\lambda}$ in eq. (3.11). The error in radiance temperature stemming from this simplification was less than 0.35 K over the entire range and less than 0.2 K in the range of 1700 to 2800 K.

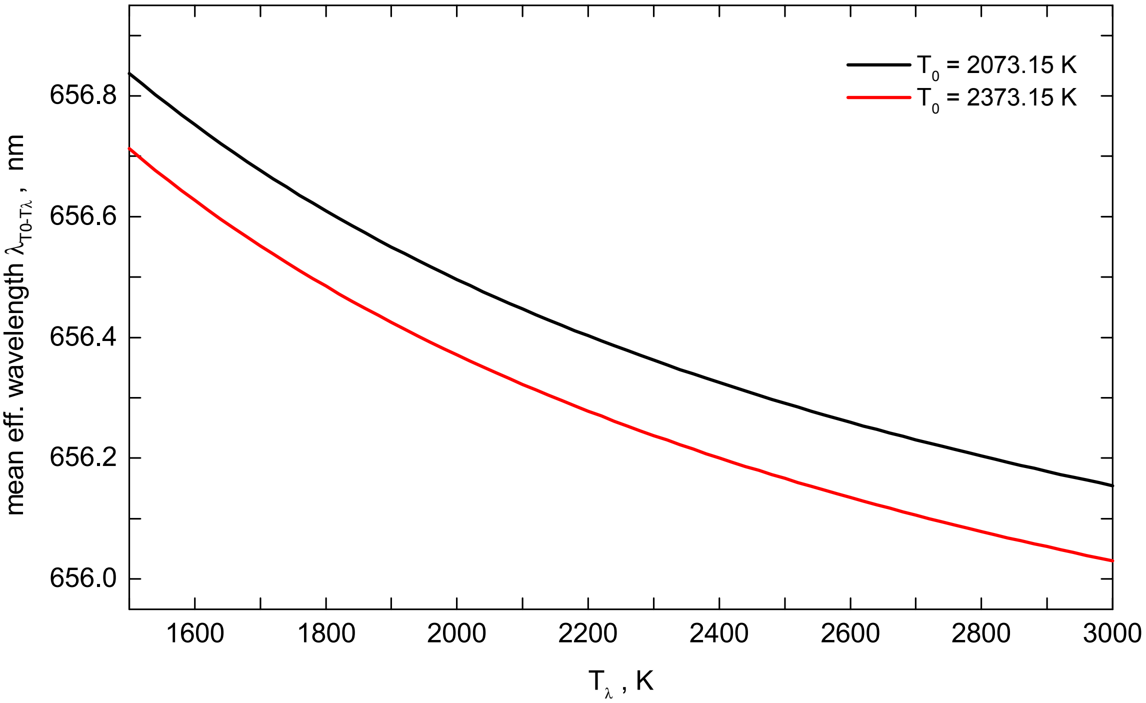

Fig. 3.11: The mean effective wavelength $\lambda_{T_0\text{-}T_\lambda}$ of the radiation thermometer as a function of target radiance temperature T_λ, for the two calibration temperatures T_0.

3.8 Reflection Polarimetry

3.8.1 Determination of normal spectral emittance from polarimetric measurements

In reflection polarimetry a light wave of known state of polarization is reflected off the specimen surface at a specified oblique angle of incidence θ_i and the state of polarization of the reflected wave is measured. This leads to the determination of the ratio q of the complex Fresnel reflection coefficients (§2.3.6) for the p and s polarizations, from which the complex index of refraction N_2 of the specimen material is derived by use of eq. (2.95):

$$n_2 - j \cdot k_2 = n_1 \cdot \tan\theta_i \cdot \left[1 - \frac{4q}{(1+q)^2}\sin^2\theta_i\right]^{\frac{1}{2}} \tag{2.95}$$

where it has been assumed that the medium in which the incident and reflected waves propagate is transparent ($k_1 = 0$).

Assuming that the specimen surface reflects specularly, the spectral normal-hemispherical reflectance $\rho_{n,h}(\lambda,T)$ (§2.1.14) can be computed from N_2 by use of eq. (2.102):

$$\rho_{n,h}(\lambda,T) = \frac{(n_2 - n_1)^2 + k_2^{\,2}}{(n_2 + n_1)^2 + k_2^{\,2}} \qquad (2.102)^1$$

In this work, the quantity of interest was the normal spectral emittance $\varepsilon_n(\lambda,T)$ of the specimen surface, which was needed in order to convert the measured radiance temperature to true (thermodynamic) temperature. $\varepsilon_n(\lambda,T)$ was determined indirectly from the spectral normal-hemispherical reflectance via the energy balance equation for opaque materials:

$$\rho_{n,h}(\lambda,T) + \varepsilon_n(\lambda,T) = 1 \tag{2.31}$$

3.8.2 The Division-of-Amplitude Photopolarimeter

In order to measure the change in the state of polarization of a laser beam upon its reflection at the specimen surface, a microsecond-resolution Division-of-Amplitude Photopolarimeter (DOAP) was used. The DOAP was first conceived by R. M. A. Azzam [25]. Compared to static ellipsometers the DOAP offers the advantage of having no moving parts, which makes it predestined for fast measurements.

The DOAP used in this work was a prototype developed by Containerless Research, Inc (CRI) in Evanston, IL, USA. This instrument was similar in design to an earlier, slower

---

[1] For brevity, the modifiers λ and T have been omitted from the right side of the equation. However, it should be kept in mind that n_1, n_2 and k_2 are all wavelength-dependent and, in addition, n_2 and k_2 depend on the temperature T of the specimen.

DOAP device, designed by CRI for use with a millisecond-resolution pulse-heating system [4, 26]. However, a number of modifications had to be made to accommodate the requirements of microsecond-resolution pulse-heating experimentation. These modifications, which will be explained below, were dictated by the need for high-speed operation and for shielding against EMI in a capacitor-discharge environment.

The DOAP consisted of three modules. The polarization state generator (PSG), the polarization state detector (PSD), and the electronics module. The PSG and the PSD contained the polarizing and analyzing components, respectively, and were situated close to the experiment chamber, each in front of one of the polarimetry viewports. The electronics module, including the modulated laser source and the photodetectors, was located outside the shielded room in order to minimize the effect of EMI on the measured signals. This was one of the major modifications, as compared to the millisecond-resolution DOAP that was mentioned above.

3.8.2.1 The Polarization state generator (PSG)

The light from the laser source was delivered to the PSG inside the shielded room using a fiber optic light guide. The PSG was used to polarize the laser beam that was incident on the specimen. It contained a Glan-Thompson crystal-prism linear polarizer, a mica quarter-wave retarder (QWR), and a converging lens. The linear polarizer and the QWR were each mounted on a computer-controlled motorized rotator. The lens reduced the divergence of the laser beam so that the spot size on the specimen was approximately 1 mm in diameter. The PSG sat on a micrometer-driven horizontal translation stage for alignment in a direction normal to the axis of the beam. This translation stage was, in turn, mounted on top of a laboratory jack for vertical alignment. The entire unit (PSG, horizontal translator, jack) was attached to a carrier that could slide on an optical table rail in a direction parallel to the laser beam. In addition, the PSG could be finely rotated about its optical axis (roll) and about the horizontal axis perpendicular to the optical axis (pitch). The roll was particularly important, since it directly affected the azimuth of the polarization ellipse of the polarized laser beam. Pitch and roll were monitored using two spirit levels attached to the PSG in the appropriate directions.

By independently rotating the linear polarizer and the QWR any desired state of polarization could be generated. The Stokes vector $\mathbf{S}_{PSG}$ of the light at the output of the PSG can be derived from the Stokes vector **S** = $[S_0\ S_1\ S_2\ S_3]^t$ of the beam delivered to the PSG through the optical fiber, where the superscript t indicates the transpose, if the Mueller matrices of the polarizing components are known. Assuming that the linear polarizer and the quarter wave retarder are perfect[1], their Mueller matrices can be expressed as

$$\mathbf{M}_{\mathrm{LP}} = \frac{1}{2} \cdot \begin{bmatrix} 1 & \cos 2P & \sin 2P & 0 \\ \cos 2P & \cos^2 2P & \sin 2P \cdot \cos 2P & 0 \\ \sin 2P & \sin 2P \cdot \cos 2P & \sin^2 2P & 0 \\ 0 & 0 & 0 & 0 \end{bmatrix} \tag{3.20}$$

$$\mathbf{M}_{\mathrm{QWR}} = \begin{bmatrix} 1 & 0 & 0 & 0 \\ 0 & \cos^2 2Q & \sin 2Q \cdot \cos 2Q & -\sin 2Q \\ 0 & \sin 2Q \cdot \cos 2Q & \sin^2 2Q & \cos 2Q \\ 0 & \sin 2Q & -\cos 2Q & 0 \end{bmatrix} \tag{3.21}$$

where $\mathbf{M}_{\mathrm{LP}}$ is the Mueller matrix of the linear polarizer and $\mathbf{M}_{\mathrm{QWR}}$ is the Mueller matrix of the quarter-wave retarder. P and Q are the angles of rotation (in a counter-clockwise sense when looking against the direction of propagation) of the transmission axis of the linear polarizer and the fast axis of the QWR, respectively, with respect to the zero reference direction, i.e. the x-axis of the coordinate system to which **S** and $\mathbf{S}_{\mathrm{PSG}}$ are referenced[2] and from which the azimuth of the polarization ellipse is measured. In practice, P and Q were measured from the zero reading on the graduated circles on the polarizer and QWR rotators. When the bubbles in the spirit levels on the PSG were centered, the laser beam was horizontal and the zero reading (x-axis) of both rotators corresponded to the laboratory horizontal direction, whereas the 90° reading (y-axis) corresponded to the laboratory vertical direction. Since the specimens in the experiment chamber were installed vertically, the laboratory horizontal direction was parallel to the plane of incidence during measurements.

---

[1] A linear polarizer is considered perfect if the transmittance for light that is linearly polarized parallel to the extinction axis is zero (extinction ratio = 0) and the transmittance for light that is linearly polarized parallel to the transmission axis is one.

A QWR is considered perfect if its transmittance is one, regardless of incident polarization, and the relative phase retardation for linear polarizations parallel to its fast and slow axes is exactly 90°.

[2] This right-handed Cartesian coordinate system is chosen such that the positive z-direction is parallel to the propagation direction of the beam (§2.3.4).

By carrying out the matrix multiplication[1]

$$\mathbf{S}_{\mathrm{PSG}} = \mathbf{M}_{\mathrm{QWR}} \cdot \mathbf{M}_{\mathrm{LP}} \cdot \mathbf{S} \tag{3.22}$$

the Stokes vector $\mathbf{S}_{\mathrm{PSG}}$ of the outgoing light is found to be

$$\mathbf{S}_{\mathrm{PSG}} = \frac{(S_0 + S_1 \cos 2P + S_2 \sin 2P)}{2} \cdot \begin{bmatrix} 1 \\ \cos 2Q \cdot \cos(2Q - 2P) \\ \sin 2Q \cdot \cos(2Q - 2P) \\ \sin(2Q - 2P) \end{bmatrix} \tag{3.23}$$

It follows from eq. (3.23) (by forming the sum of the squares of the elements of $\mathbf{S}_{\mathrm{PSG}}$) that the outgoing laser beam is totally polarized. This is expected, since we assumed the polarizer of the PSG to be perfect. Furthermore, by inspecting the multiplicative factor in eq. (3.23), it is evident that the stronger the linear preferences in the light that is incident on the PSG are, as expressed by nonzero values of S_1 and S_2, the more the outgoing beam will be modulated by a rotation of the linear polarizer.

A comparison of eqs. (3.23) and (2.72) yields the following system of equations relating P and Q to the azimuth θ and the ellipticity andgle ε of the polarization ellipse of the outgoing laser beam:

$$\cos 2Q \cdot \cos(2Q - 2P) = \cos 2\theta \cdot \cos 2\varepsilon \tag{3.24a}$$

$$\sin 2Q \cdot \cos(2Q - 2P) = \sin 2\theta \cdot \cos 2\varepsilon \tag{3.24b}$$

$$\sin(2Q - 2P) = \sin 2\varepsilon \tag{3.24c}$$

For a given pair of θ and ε, these equations can easily be solved to yield the values of P and Q required to generate that particular state of polarization. Specifically, it follows from eq. (3.24c) that P and Q can be chosen such that either

$$Q - P = \varepsilon \quad (3.25\mathrm{a}) \qquad \text{or} \qquad Q - P = \pm\frac{\pi}{2} - \varepsilon \quad (3.25\mathrm{b})$$

---

[1] The converging lens alters only the total radiant flux of the beam, not its polarization state. Its effect is neglected here for simplicity, since we're not interested in the absolute radiant flux.

Equations (3.24a) and (3.24b) then yield:

$$Q = \theta \qquad (3.26a) \qquad \text{or} \qquad Q = \theta \pm \frac{\pi}{2} \qquad (3.26b)$$

respectively, provided that $\cos 2\varepsilon \neq 0$. The signs in eqs. (3.25b) and (3.26b) can be chosen independently of each other. The difference in choosing either sign is only formal, since azimuthal orientations of the QWR or the linear polarizer that are 180°-apart are physically indistinguishable.

If $\cos 2\varepsilon = 0$, then $\varepsilon = \pm\pi/4$, which means that the outgoing light is circularly polarized. In that case, the azimuth θ is, of course, indeterminate. The angular position of the QWR relative to that of the linear polarizer that is required to generate circularly polarized light follows from eqs. (3.25a) or (3.25b):

$$\text{For RCP light:} \qquad Q - P = \frac{\pi}{4} \qquad (3.27)$$

$$\text{For LCP light:} \qquad Q - P = -\frac{\pi}{4} \qquad (3.28)$$

To generate linearly polarized light ($\varepsilon = 0$) the QWR has to be oriented with its fast axis either parallel or perpendicular to the transmission axis of the linear polarizer:

$$Q - P = 0 \qquad (3.29a) \qquad \text{or} \qquad Q - P = \pm\frac{\pi}{2} \qquad (3.29b)$$

In both cases, the azimuth of the linearly polarized light is determines the required azimuth of the linear polarizer:

$$P = \theta \qquad (3.30)$$

For linearly polarized output light, eq. (3.23) takes on the simpler form

$$\mathbf{S}_{\mathrm{PSG}} = \frac{(S_0 + S_1 \cos 2P + S_2 \sin 2P)}{2} \cdot \begin{bmatrix} 1 \\ \cos 2P \\ \sin 2P \\ 0 \end{bmatrix} \qquad (3.31)$$

This is equivalent to removing the QWR from the optical train. Equation (3.31) can, therefore, be directly obtained from eq. (3.22) if $\mathbf{M}_{\mathrm{QWR}}$ is omitted.

3.8.2.2 The polarization state detector (PSD)

A functional diagram of the PSD is shown in fig. (3.12). Light reflected off the cylindrical specimen was collected by the objective lens[1] and was focused on the plane of a 2 mm pinhole. An iris diaphragm in front of the objective acted as an aperture stop. Since cylindrical surfaces produce a diverging ribbon of reflected light in the plane of incidence, the iris opening controlled the angular range over which light was collected, as well as its amount. The polarimeter signals increased with increasing opening, but at the same time so did the angular uncertainty (θ_i in eq. 2.95). An opening of 10 mm in diameter was a reasonable compromise between increased accuracy and better signal to noise ratio. An interference filter was used to block most of the background light that was thermally emitted by the specimen. The filter was centered at 677 nm and had a nominal bandwidth (FWHM) of 3 nm. Having passed through the aperture, the beam was collimated by a lens before it struck a beamsplitter made of ZnS and coated with a thin layer of MgF_2. The beam splitter, which was the key element of the DOAP, was oriented at an angle of 70° to the optical axis of the PSD. It divided the incident beam into a reflected and a transmitted beam. Each of these beams was, in turn, analyzed into two orthogonally polarized beams, i.e. the ordinary and the extraordinary beam, by a beamsplitting Glan-Thompson prism. The angular separation of the two beams exiting each prism was 45°. The orthogonal transmission axes of the Glan-Thompson prisms were oriented at 45° and 135° with respect to the plane of incidence at the coated beam splitter. The four light beams that were produced by the three beamsplitters constituted the output of the PSD. They were focused into optical fibers that transmitted the light to four photodetectors in the electronics module outside the shielded room, thus ensuring immunity to EMI.

Like the PSG, the PSD sat on a micrometer-driven horizontal translation stage for left-right alignment, a laboratory jack for height adjustment, and a carrier that could be moved along an optical table rail in a direction parallel to the optical axis of the PSD in order to focus the PSD on the specimen. The PSD could be rotated about its optical axis, the vertical axis, and the horizontal axis perpendicular to the optical axis, to finely adjust its roll, yaw, and pitch, respectively. Pitch and roll were monitored with a circular spirit level. The design was such,

---

[1] In actuality, a pair of plano-convex lenses with the interference filter placed in-between.

that the base point of rotation when changing the pitch or yaw of the PSD lay near the center of the iris diaphragm in the front, largely decoupling such a rotation from a translational alignment of the PSD's front end. This facilitated the alignment of the instrument, which had to be carried out with great care because the measurement was rather sensitive to misalignment.

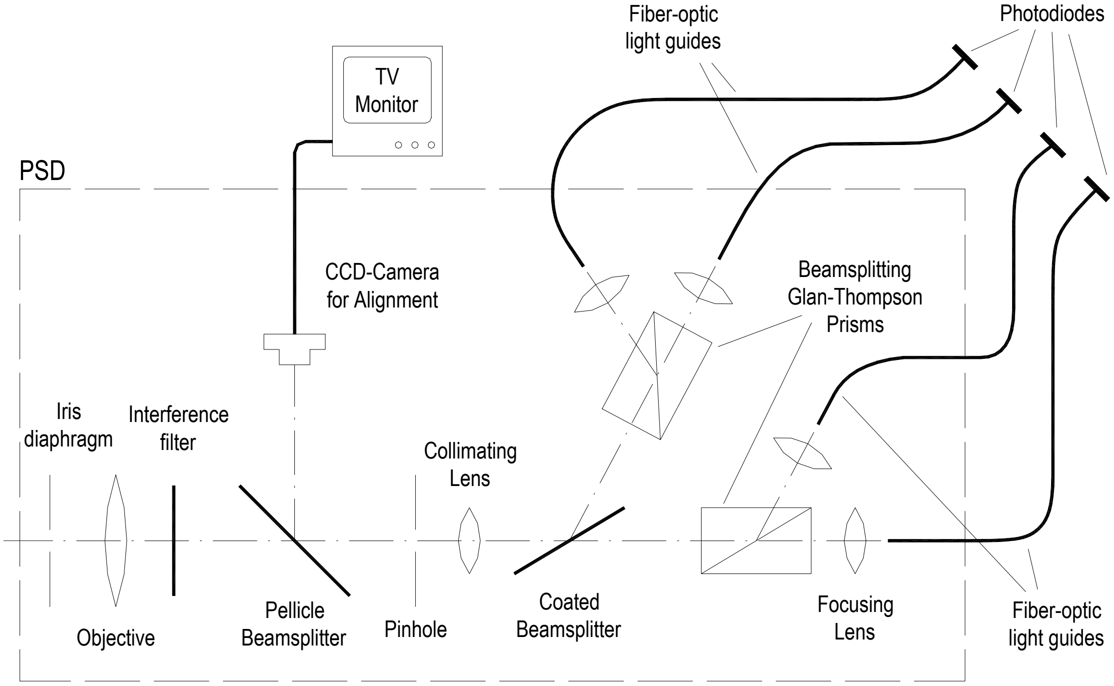

Fig. 3.12: Functional diagram of the PSD.

As in the case of the PSG, the roll was very important, since a rotation of the PSD about its optical axis in one direction would have been perceived by the instrument as a rotation in the opposite direction of the ellipse of polarization of the light entering the PSD. Just as important was the angle between the optical axis of the PSD and that of the PSG. This angle determined the angle of incidence θ_i on the cylindrical specimen that had to be accurately known in order to compute the complex index of refraction of the specimen (eq. 2.95). Although the rails, on which the PSG and the PSD could be moved, were installed such as to include an angle of 140°, an exact value for θ_i was established using a custom-made glass prism placed at the specimen location (fig. 3.13). The laser was first directed at the front prism face (toward the PSG) and the prism was rotated until the beam was reflected back into itself, which meant that the front face was perpendicular to the incident laser beam. The PSG was then horizontally translated until the laser beam struck the inclined prism face, which exactly included an angle of 70° with the back prism face, thus ensuring that the angle of incidence was also 70°. The PSD was translated until the reflected laser beam entered centrally through the iris diaphragm, which for this purpose had been closed to a small diameter. Finally, the PSD was rotated about the vertical axis (yaw) to have the laser beam pass centrally through the pinhole, as well. An enlarged image of the pinhole could be viewed on a TV monitor via a small CCD-chip and a pellicle beamsplitter that were installed inside the PSD (fig. 3.12) to facilitate alignment.

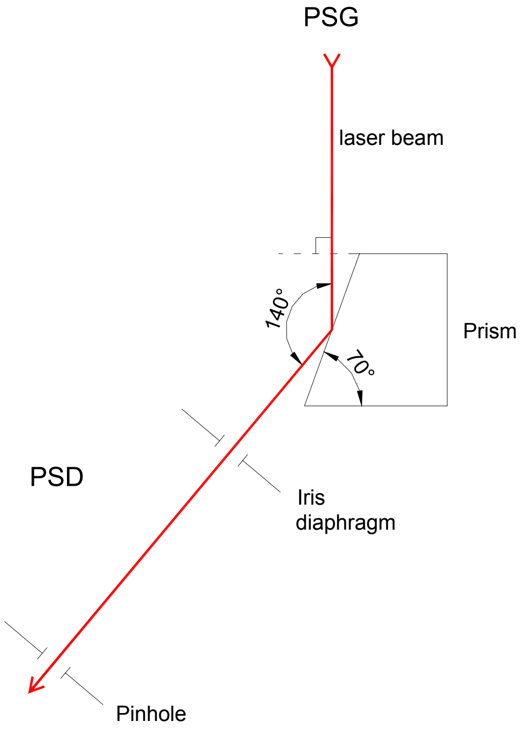

Fig. 3.13: Schematic drawing explaining the alignment of the PSD using a prism to establish an angle of incidence of 70°. The drawing is not to scale.

3.8.2.3 The electronics

A temperature-stabilized laser diode system was used as the laser source for the DOAP measurements. As mentioned above, it was contained in the electronics module outside the shielded room. It featured active thermoelectric temperature control via a bipolar Peltier element. This was important because the emitted wavelength in laser diode systems is known to depend on temperature (typical temperature coefficients range from 0.1 to 0.3°nm·K^{-1}). The temperature control allowed the laser wavelength to be finely adjusted until it closely matched the wavelength of peak transmission of the interference filter (677 nm), yielding maximum signal. In addition, the constant temperature prevented a drift in wavelength as the diode heated up during operation. To improve the signal-to-noise ratio and reject light that was thermally emitted by the specimen within the passband of the PSD's interference filter the laser was amplitude-modulated. A 4 MHz square TTL-level waveform was used as the carrier signal.

The laser beam was then coupled into the optical fiber that was clamped in a custom-made fixture. This fixture permitted translational and angular alignment of the clamped fiber end along and about two orthogonal axes perpendicular to the beam to achieve the best possible coupling of the laser light into the fiber core. The modulated laser beam was delivered to the PSG, reflected off the target, and analyzed by the PSD.

The four output light signals of the PSD were collected by four optical fibers and delivered to an equal number of silicon PIN photodiodes inside the electronics module. Each of the photodiode signals was then individually pre-amplified, demodulated using phase-locked loops, and further amplified to be finally recorded by the data acquisition instrumentation. A block diagram of one (out of a total of four) of the DOAP channels is shown in fig. (3.14).

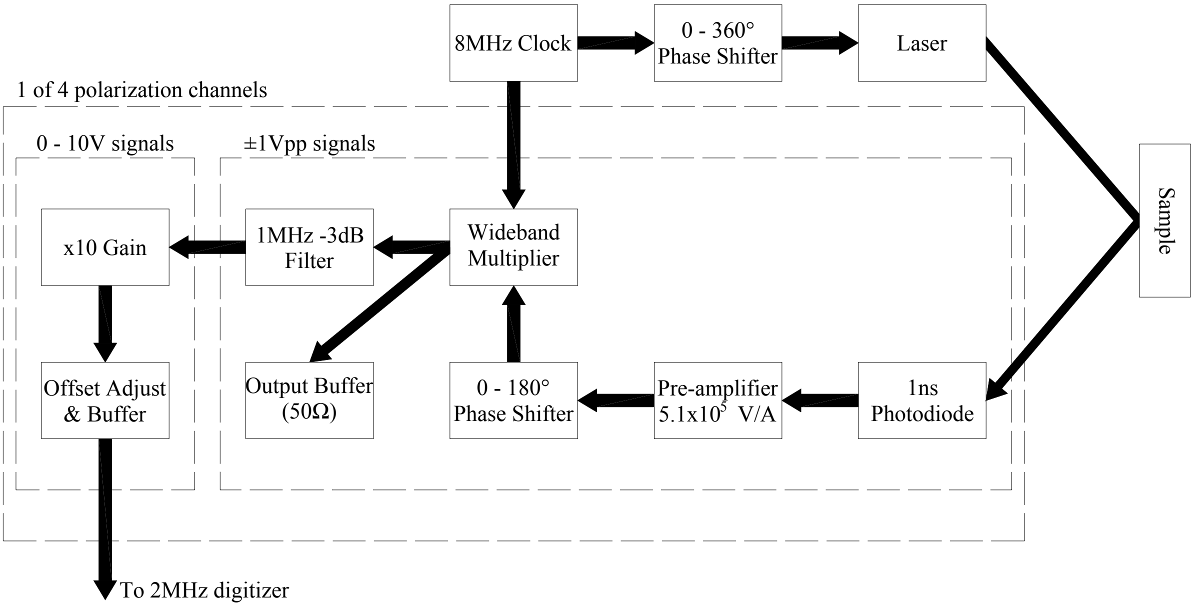

Fig. 3.14: Block diagram of the DOAP electronics (courtesy of CRI). Only one channel is shown.

3.8.2.4 Measurement

In order to derive the equations relating the four electrical output signals of the DOAP to the optical properties of the reflecting specimen, it is not necessary to know the exact details describing the propagation of the light through the system. Following the linear-systems approach introduced in §(2.3.5), the optical system is simply described in terms of the component Mueller matrices.

The laser light entering the PSD was split into four separate beams that were then coupled into the collection fibers and delivered to the photodiodes. Each of these beams can be described in terms of a Stokes vector and the path the beam propagated through by a Mueller matrix. The following four equations relate the Stokes vectors of the four light beams that are coupled into the fibers, via the Mueller matrices of their respective paths through the PSD, to the Stokes vector $\mathbf{S}_r$ of the light entering the PSD:

$$\mathbf{S}_{tt} = \mathbf{M}_{tt} \cdot \mathbf{S}_r \tag{3.32a}$$

$$\mathbf{S}_{tr} = \mathbf{M}_{tr} \cdot \mathbf{S}_r \tag{3.32b}$$

$$\mathbf{S}_{rr} = \mathbf{M}_{rr} \cdot \mathbf{S}_r \tag{3.32c}$$

$$\mathbf{S}_{rt} = \mathbf{M}_{rt} \cdot \mathbf{S}_r \tag{3.32d}$$

The subscripts tt, tr, rr, and rt stand for ‘transmitted-transmitted’, ‘transmitted-reflected’, ‘reflected-reflected’, and ‘reflected-transmitted’, respectively, and describe the path of a particular beam in the PSD. Transmitted-reflected, for instance, would mean that the beam was first transmitted at the coated beamsplitter and subsequently reflected at the beamsplitting Glan-Thompson prism. $\mathbf{M}_{tt}$, $\mathbf{M}_{tr}$, $\mathbf{M}_{rr}$, and $\mathbf{M}_{rt}$ can be derived from the optical properties and orientations of the optical components of the PSD, most importantly the coated beam splitter and the beam-splitting Glan-Thompson prisms. In most cases though, a calibration procedure performed in-situ will be more accurate.

The four electrical signals making up the output of the DOAP were each proportional to the radiant flux of one of the four beams exiting the PSD, hence to the first component of the Stokes vector representing that particular beam (eqs. 3.32a - 3.32d). If we cast these four signals into a column vector **I**, then this vector is related to $\mathbf{S}_r$ by the following expression:

$$\mathbf{I} = \begin{bmatrix} I_{tt} \\ I_{tr} \\ I_{rr} \\ I_{rt} \end{bmatrix} = \begin{bmatrix} r_{tt} \cdot S_{tt,0} \\ r_{tr} \cdot S_{tr,0} \\ r_{rr} \cdot S_{rr,0} \\ r_{rt} \cdot S_{rt,0} \end{bmatrix} = \begin{bmatrix} r_{tt} \cdot \mathbf{M}_{tt}^{<0>} \\ r_{tr} \cdot \mathbf{M}_{tr}^{<0>} \\ r_{rr} \cdot \mathbf{M}_{rr}^{<0>} \\ r_{rt} \cdot \mathbf{M}_{rt}^{<0>} \end{bmatrix} \cdot \mathbf{S}_r \tag{3.33}$$

$S_{tt,0}$, $S_{tr,0}$, $S_{rr,0}$, and $S_{rt,0}$ denote the first element of $\mathbf{S}_{tt}$, $\mathbf{S}_{tr}$, $\mathbf{S}_{rr}$, and $\mathbf{S}_{rt}$, respectively. The transmittance of the fibers, the responsivity of the photodiodes, the current-to-voltage conversion and subsequent amplification of the photodiode signal by the DOAP electronics, and the gain of the data acquisition instrumentation were all lumped into four proportionality constants, r_{tt}, r_{tr}, r_{rr}, and r_{rt}, one for each of the four DOAP channels. $\mathbf{M}_{tt}^{<0>}$, $\mathbf{M}_{tr}^{<0>}$, $\mathbf{M}_{rr}^{<0>}$, and $\mathbf{M}_{rt}^{<0>}$ denote the first row of the respective Mueller matrices.

The matrix by which $\mathbf{S}_r$ is pre-multiplied in eq. (3.33) is a real 4×4 matrix that is characteristic of the instrument. It is called the instrument or calibration matrix of the DOAP and will be denoted by $\mathbf{F}$:

$$\mathbf{F} = \begin{bmatrix} r_{tt} \cdot \mathbf{M}_{tt}^{<0>} \\ r_{tr} \cdot \mathbf{M}_{tr}^{<0>} \\ r_{rr} \cdot \mathbf{M}_{rr}^{<0>} \\ r_{rt} \cdot \mathbf{M}_{rt}^{<0>} \end{bmatrix} \tag{3.34}$$

Thus, eq. (3.33) takes on the simple form

$$\mathbf{I} = \mathbf{F} \cdot \mathbf{S}_r \tag{3.35}$$

Pre-multiplication of eq. (3.35) with $\mathbf{F}^{-1}$, the inverse instrument matrix, yields

$$\mathbf{S}_r = \mathbf{F}^{-1} \cdot \mathbf{I} \tag{3.36}$$

A condition for $\mathbf{F}^{-1}$ to exist, is, of course, that $\mathbf{F}$ be non-singular.

The light that is analyzed by the PSD during measurement is light that was first reflected off the specimen. Therefore, $\mathbf{S}_r$ can be expressed in terms of the Stokes vector $\mathbf{S}_i$ of the laser beam that is incident on the specimen and the Mueller matrix $\mathbf{M}_{ref}$ of reflection:

$$\mathbf{S}_r = \mathbf{M}_{ref} \cdot \mathbf{S}_i \tag{3.37}$$

As already stressed in §(2.3.5), $\mathbf{M}_{ref}$ depends on the azimuthal orientation of the (x, y) and (x′, y′) axes of the coordinate systems to which $\mathbf{S}_i$ and $\mathbf{S}_r$ are referenced. When the directions of x and x′ are chosen in the plane of incidence, the Mueller matrix $\mathbf{M}_{ref}$ of an isotropic, non-depolarizing reflector as a function of the ellipsometric angles ψ and Δ, is given (see [27]) by:

$$\mathbf{M}_{\mathrm{ref}} = \frac{\rho_p + \rho_s}{2} \cdot \begin{bmatrix} 1 & -\cos 2\psi & 0 & 0 \\ -\cos 2\psi & 1 & 0 & 0 \\ 0 & 0 & \sin 2\psi \cdot \cos\Delta & \sin 2\psi \cdot \sin\Delta \\ 0 & 0 & -\sin 2\psi \cdot \sin\Delta & \sin 2\psi \cdot \cos\Delta \end{bmatrix} \tag{3.38}$$

The factor by which the matrix is pre-multiplied can be recognized as the reflectance for unpolarized incident light (eq. 2.100).

With $\mathbf{S}_i$ known from the angular positions of the linear polarizer and the quarter-wave retarder in the PSG (eq. 3.23) and $\mathbf{S}_r$ measured by the DOAP, eq. (3.37) could be solved for ψ and Δ. Since we were not interested in the absolute radiant flux of the incident and of the reflected beams, $\mathbf{S}_i$ and $\mathbf{S}_r$ were normalized with respect to their first element $S_{i,0}$ and $S_{r,0}$, respectively. The letter n in the subscript of the Stokes parameters in the following equations stands for 'normalized':

$$\cos 2\psi = \frac{S_{i,1n} - S_{r,1n}}{1 - S_{i,1n} \cdot S_{r,1n}} \tag{3.39}$$

$$\sin\Delta = \frac{1 - S_{i,1n} \cdot \cos 2\psi}{\left[\left(S_{i,2n}\right)^2 + \left(S_{i,3n}\right)^2\right] \cdot \sin 2\psi} \cdot \left(S_{r,2n} \cdot S_{i,3n} - S_{i,2n} \cdot S_{r,3n}\right) \tag{3.40}$$

$$\cos\Delta = \frac{1 - S_{i,1n} \cdot \cos 2\psi}{\left[\left(S_{i,2n}\right)^2 + \left(S_{i,3n}\right)^2\right] \cdot \sin 2\psi} \cdot \left(S_{i,2n} \cdot S_{r,2n} + S_{i,3n} \cdot S_{r,3n}\right) \tag{3.41}$$

$$\tan\Delta = \frac{S_{r,2n} \cdot S_{i,3n} - S_{i,2n} \cdot S_{r,3n}}{S_{i,2n} \cdot S_{r,2n} + S_{i,3n} \cdot S_{r,3n}} \tag{3.42}$$

Equation (3.42), which was derived from eqs. (3.40) and (3.41), was used to compute Δ. Attention was paid to the signs of the numerator and denominator in eq. (3.42) to determine the proper quadrant for Δ. Equations (3.40) and (3.41) were used as a consistency check since they had to obey

$$\sin^2\Delta + \cos^2\Delta = 1 \tag{3.43}$$

Substitution of $\cos 2\psi$, $\sin\Delta$, and $\cos\Delta$ from eqs. (3.39) - (3.41) into eq. (3.43) yields

$$\sin^2\Delta + \cos^2\Delta = \frac{1 - \left(S_{i,1n}\right)^2}{P_i^2 - \left(S_{i,1n}\right)^2} \cdot \frac{P_r^2 - \left(S_{r,1n}\right)^2}{1 - \left(S_{r,1n}\right)^2} \tag{3.44}$$

where P_i and P_r denote the degree of polarization (eq. 2.76) for the incident and the reflected light, respectively. In our case, P_i was very close to 1 because the incident light was polarized in the PSG. Thus, P_r had to be very close to 1, as well, since we assumed the process of reflection to be non-depolarizing (eq. 2.79). If we substitute $P_i = P_r = 1$ into eq. (3.44) we obtain eq. (3.43). Therefore, any larger deviation of $\sin^2\Delta + \cos^2\Delta$ from unity would have indicated that the surface was depolarizing, possibly as a result of excessive roughness. Rough surfaces are known to be depolarizing. When surfaces are depolarizing, non-zero values occur in the 2×2 off-diagonal blocks of $\mathbf{M}_{\text{ref}}$. In addition, terms in the 2×2 diagonal blocks, which in the case of the isotropic specular reflector are numerically equal, become unequal [28, 29]. In that case, the use of eq. (3.38) is not justified.

3.8.2.5 Calibration

The goal of the calibration was to obtain the instrument matrix **F**. This was done by recording the DOAP response to a number of known polarization states generated by the PSG. **F** was then computed from the acquired data by inversion.

For calibration, the PSG was moved from the measurement position[1] to the straight-through position, meaning that the polarized laser beam was incident directly onto the PSD (fig. 3.15). The distance of the PSG from the PSD during calibration was equal to the combined distances of the PSG and the PSD from the specimen during measurements. A neutral density filter was inserted in front of the linear polarizer in the PSG to prevent the DOAP output from saturating.

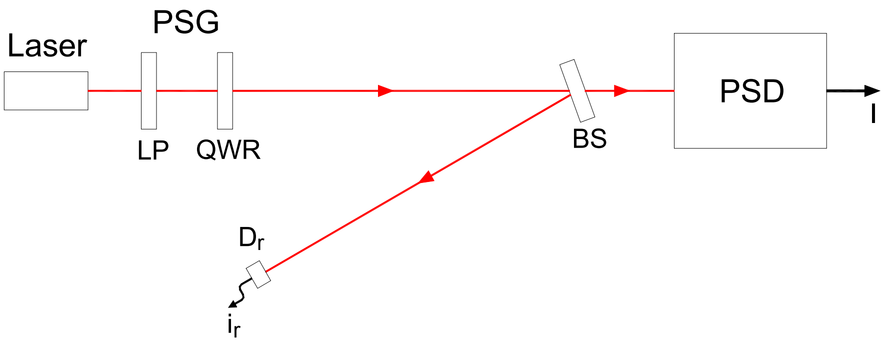

Fig. 3.15: Functional diagram showing the PSD and the PSG in the calibration position (adapted from [30]). LP…linear polarizer, QWR…quarter-wave retarder, BS…beamsplitter, D_r…reference detector.

---

[1] As outlined in §(3.8.2.2), when conducting measurements, the PSG and the PSD were set up such that their optical axes included an angle of 140°.

The different polarization states required for calibration were generated by rotating the linear polarizer and the quarter-wave retarder in the PSG. Because the beam, which was delivered to the PSG via an optical fiber, exhibited residual linear preferences, the rotation of the linear polarizer caused a variation in the total radiant flux incident on the PSD (eq. 3.23). This unwanted effect was cancelled by normalizing the four DOAP signals with respect to the varying incident flux. To measure this flux, a pellicle beamsplitter was installed in front of the PSD and a reference detector attached to the PSG. Both these components were used only during calibration and removed afterwards. The beamsplitter was tilted by a small angle (<5°) with respect to the plane perpendicular to the incident laser beam and reflected part of it onto the reference detector. Because this reference beam was generated by near-normal incidence reflection from the beamsplitter, its flux was a fixed fraction (approximately 5%) of the incident flux, irrespective of the incident polarization [31]. Therefore, any changes in the reference detector signal i_r were a direct measure for the relative variation in the total incident flux, caused by the rotation of the polarizer or, perhaps, by instabilities in the laser source. By using the normalized DOAP signal vector $\mathbf{I}/i_r$ to determine the instrument matrix $\mathbf{F}$ both effects were rendered inconsequential. At the same time, this normalization justified the use of a normalized Stokes vector $[1\ S_1\ S_2\ S_3]^t$ to describe the input light to the PSD.

In principle, the instrument matrix can be determined from the response of the DOAP to only four linearly independent polarization states[1]. If we let $\mathbf{S}_k$ denote the Stokes vector of one of these states and $\mathbf{I}_k$ the corresponding column vector formed by the four electrical signals constituting the DOAP response, then, according to eq. (3.35):

$$\mathbf{I}_k = \mathbf{F} \cdot \mathbf{S}_k \qquad (k = 0 \ldots 3) \tag{3.45}$$

Let $\boldsymbol{I}$ denote a matrix whose columns are the four signal vectors $\mathbf{I}_k$ and $\boldsymbol{S}$ denote a matrix whose columns are the corresponding Stokes vectors $\mathbf{S}_k$ of the four incident polarization states. Then, the above system of four algebraic equations can be reduced into one that only involves 4×4 matrices,

$$\boldsymbol{I} = \mathbf{F} \cdot \boldsymbol{S} \tag{3.46}$$

---

[1] By linearly independent polarization states we mean polarization states whose Stokes vectors are linearly independent.

from which the instrument matrix is obtained by pre-multiplication with $\boldsymbol{S}^{-1}$:

$$\mathbf{F} = \boldsymbol{I} \cdot \boldsymbol{S}^{-1} \tag{3.47}$$

The inverse matrix $\boldsymbol{S}^{-1}$ ought to exist, since the columns of $\boldsymbol{S}$ (i.e. the four calibration Stokes vectors) are linearly independent. An optimum choice of polarization states for this calibration results if the endpoints of the four vectors $\mathbf{S}_k$ in the Stokes subspace (§2.3.4) become the vertices of a tetrahedron [32]. This is the maximum-volume pyramid inscribed inside the unit-sphere (Poincaré sphere) and corresponds to the maximum determinant of $\boldsymbol{S}$.

The accuracy of this straightforward calibration procedure, called the four-point method, is, of course, negatively influenced by imperfections in the polarizing components of the PSG. Superior results can be obtained by a different calibration scheme, known as the equator-poles method, that has been described in [30]. It involves the measurement of the DOAP response to a larger number of incident polarization states and allows the instrument matrix **F** to be determined mostly free of the small imperfections in the PSG. The equator-poles method was used in this work to calibrate the DOAP. It was carried out in two steps.

In the first step, the QWR was removed from the PSG and the four output signals of the DOAP were recorded as the linear polarizer was rotated through 360° in steps of 10°. In other words, the instrument response to incident linearly polarized light of variable azimuth was measured. Ideally, azimuthal positions of the polarizer that are 180°-apart are physically indistinguishable and one should only need to let the linear polarizer complete half a revolution to obtain all the desired information. In practice, however, this is not exactly the case because of a small angular beam deviation introduced by the polarizer. By averaging the responses of the DOAP recorded at 180°-apart this effect was largely cancelled. It was found that the difference between the responses of any of the four DOAP detectors to two such diametrically opposite orientations could be as much as 12%. The average difference, though, was much less, approximately 2% to 5%.

The normalized Stokes vector of the incident linearly polarized light, as a function of the polarizer azimuth P, is given by eq. (3.31):

$$\mathbf{S}_{\mathrm{LP}} = \begin{bmatrix} 1 \\ \cos 2P \\ \sin 2P \\ 0 \end{bmatrix} \tag{3.48}$$

The four normalized DOAP signals are linked to $\mathbf{S}_{\mathrm{LP}}$ by the instrument matrix **F**. Substitution of eq. (3.48) into eq. (3.35) yields

$$\mathbf{I}_{\mathrm{LP}} = \begin{bmatrix} I_0 \\ I_1 \\ I_2 \\ I_3 \end{bmatrix} = \begin{bmatrix} F_{00} + F_{01} \cdot \cos 2P + F_{02} \cdot \sin 2P \\ F_{10} + F_{11} \cdot \cos 2P + F_{12} \cdot \sin 2P \\ F_{20} + F_{21} \cdot \cos 2P + F_{22} \cdot \sin 2P \\ F_{30} + F_{31} \cdot \cos 2P + F_{32} \cdot \sin 2P \end{bmatrix} \tag{3.49}$$

F_{ij} denotes the element in the ith row and jth column of **F** (i,j=0,1,2,3). I_0, I_1, I_2, and I_3 correspond to I_{tt}, I_{tr}, I_{rr} and I_{rt} of eq. (3.33), in exactly this order.

By fitting I_0, I_1, I_2, and I_3 to the simple Fourier series of eqs. (3.49), the first three columns of **F** were obtained. Allowing most of the instrument matrix to be obtained without the QWR in the optical train is an important feature of the equator-poles method, considering that the most significant imperfections of the PSG reside in the quarter-wave retarder [30].

In the second step of the calibration, the instrument response to circularly polarized light was measured. The normalized Stokes vectors of right-circularly and left-circularly polarized light are given by:

$$\mathbf{S}_{\mathrm{RCP}} = \begin{bmatrix} 1 \\ 0 \\ 0 \\ 1 \end{bmatrix} \tag{3.50a}$$

$$\mathbf{S}_{\mathrm{LCP}} = \begin{bmatrix} 1 \\ 0 \\ 0 \\ -1 \end{bmatrix} \tag{3.50b}$$

Substitution of eqs. (3.50a) and (3.50b) into eq. (3.35) yields for the DOAP response to circularly polarized light:

$$\mathbf{I}_{\mathrm{RCP}} = \begin{bmatrix} F_{00} + F_{03} \\ F_{10} + F_{13} \\ F_{20} + F_{23} \\ F_{30} + F_{33} \end{bmatrix} \tag{3.51a}$$

$$\mathbf{I}_{\mathrm{LCP}} = \begin{bmatrix} F_{00} - F_{03} \\ F_{10} - F_{13} \\ F_{20} - F_{23} \\ F_{30} - F_{33} \end{bmatrix} \tag{3.51b}$$

Thus, the fourth and last column of the instrument matrix can be obtained from the difference between $\mathbf{I}_{\text{LCP}}$ and $\mathbf{I}_{\text{RCP}}$:

$$\frac{1}{2}(\mathbf{I}_{\text{RCP}} - \mathbf{I}_{\text{LCP}}) = \begin{bmatrix} F_{03} \\ F_{13} \\ F_{23} \\ F_{33} \end{bmatrix} \tag{3.52}$$

In addition, the average of the two signal vectors yields the first column of **F**:

$$\frac{1}{2}(\mathbf{I}_{\text{RCP}} + \mathbf{I}_{\text{LCP}}) = \begin{bmatrix} F_{00} \\ F_{10} \\ F_{20} \\ F_{30} \end{bmatrix} \tag{3.53}$$

Equation (3.53) was only used as a consistency check, since the first column of the instrument matrix was obtained in the first step of the calibration from a multitude of incident linearly polarized states. Typically, the largest relative difference in the elements of the column obtained in the two steps was below 1%.

According to eqs. (3.27) and (3.28), the only condition to be satisfied in order to generate RCP (or LCP) light, is that the QWR lead (or lag) the linear polarizer by 45°. However, imperfections in the QWR make it practically impossible to produce exact circular polarization states (CS). Instead, elliptical states that are more or less near-circular (NCS) will be generated by the PSG when the fast axis of the QWR is oriented at (or near) ±45° with respect to the transmission axis of the linear polarizer. Nevertheless, it is still possible to measure the DOAP response to exact circular states, without being able to produce them, if the deviation of the near-circular states from the ideal is small [30].

The difference β of the ellipticity angle ε of an elliptical state from ±45° can be used as a measure of how close to circular this state is:

$$\beta = 45° - |\varepsilon| \tag{3.54}$$

If β is small enough for the first-order approximations $\cos 2\beta \approx 1$ and $\sin 2\beta \approx 2\beta$ to be justified, it can be shown that the DOAP response to a circular state equals the average instrument response to two near-circular states of orthogonal azimuths, θ and $\theta+90°$:

$$\mathbf{I}_{\text{CS}} = \frac{1}{2}[\mathbf{I}_{\text{NCS}}(\theta) + \mathbf{I}_{\text{NCS}}(\theta + 90°)] \tag{3.55}$$

To obtain $\mathbf{I}_{\mathrm{RCP}}$, any two right-handed near-circular states with the same β and orthogonal azimuths can be used. Similarly, to obtain $\mathbf{I}_{\mathrm{LCP}}$, any two left-handed near-circular states with the same β and orthogonal azimuths can be used for the response to LCP light. No explicit knowledge of either θ or β, and hence of the PSG imperfections, is required for this measurement.

The effect of angular beam deviation as it traverses the PSG, needs again to be taken into account, as in the first calibration step. Since there are two components in the beam path now, four measurements have to be averaged for every combination of P and Q, namely with the linear polarizer and QWR oriented at (P,Q), (P,Q+180°), (P+180°,Q), and (P+180°,Q+180°). Combining this with eq. (3.55), a total of sixteen measurements have to be taken to obtain the DOAP response to right-circular and left-circular light. The values of P and Q (initial orientation) can be arbitrarily chosen, as long as they satisfy P–Q = ±45°. A possible choice is:

$$\mathbf{I}_{\mathrm{RCP}} = \frac{1}{2}\left\{\begin{aligned} &\frac{1}{4}[\mathbf{I}(0°,45°)+\mathbf{I}(0°,225°)+\mathbf{I}(180°,45°)+\mathbf{I}(180°,225°)] \\ &\qquad +\frac{1}{4}[\mathbf{I}(90°,135°)+\mathbf{I}(90°,315°)+\mathbf{I}(270°,135°)+\mathbf{I}(270°,315°)]\end{aligned}\right\} \tag{3.56}$$

$$\mathbf{I}_{\mathrm{LCP}} = \frac{1}{2}\left\{\begin{aligned} &\frac{1}{4}[\mathbf{I}(0°,135°)+\mathbf{I}(0°,315°)+\mathbf{I}(180°,135°)+\mathbf{I}(180°,315°)] \\ &\qquad +\frac{1}{4}[\mathbf{I}(90°,45°)+\mathbf{I}(90°,225°)+\mathbf{I}(270°,45°)+\mathbf{I}(270°,225°)]\end{aligned}\right\} \tag{3.57}$$

where the first angle in the round brackets indicates the polarizer azimuth and the second one the retarder azimuth.

The computer-controlled rotators in the PSG were, by default, programmed to take thirty eight measurements, nineteen for RCP and nineteen for LCP light. The polarizer-retarder combination was rotated solidly as one piece through a complete circle in steps of 20°, once with the retarder leading the polarizer by 45° and once with the retarder lagging by the same angle. Although this is a deviation from the recommendations in [30], the large number of calibration states should yet warrant results of nearly the same quality.

The top graph in fig. (3.16)[1] shows the raw polarimeter signals (prior to normalization) and

---

[1] Figures (3.16) - (3.19) are at the end of this section.

the reference detector signal recorded during the latest calibration. A total of seventy five data points was acquired in both calibration steps. The effect of the varying incident flux is apparent in the instrument response to the (near-) circular states, which should be (nearly) constant.

The normalized signals are shown in the bottom graph of the same figure. As expected, the response to the (near-) circular states is now much more constant. The residual variation probably stems from the above mentioned angular deviation of the beam and the fact that the incident states are not exactly circular. Table (3-1) lists the standard deviations of the individual signals from their mean value, before and after normalization.

Figure (3.17) shows the normalized instrument response to linearly polarized light of variable azimuth, in the range 0° to 180°, after averaging signals recorded at azimuths that were 180°-apart. The signals were least-squares fitted to the Fourier-series of eq. (3.49) to yield the first three columns of the instrument matrix. The solid lines in the graph represent the fits. The standard deviations of the measured data points from the fits were 3.6 mV for I_0, 2.2 mV for I_1, 5.2 mV for I_2, and 5.6 mV for I_3.

Table 3-1: Relative standard deviations of the individual polarimeter signals from their mean value, for the different incident (near-) circular states generated during calibration, before and after normalization.

	Relative standard deviations			
	Before normalization		After normalization	
	RCP	LCP	RCP	LCP
I_0	3.64%	3.29%	2.39%	1.91%
I_1	3.29%	3.66%	1.22%	1.51%
I_2	2.42%	2.47%	1.57%	1.42%
I_3	2.52%	2.63%	1.11%	1.93%
ref. det.	3.17%	3.36%		

The instrument matrix obtained by this calibration and its determinant are shown below:

$$\mathbf{F} = \begin{bmatrix} 0.845 & 0.224 & 0.781 & -0.112 \\ 1.228 & 0.314 & -1.098 & 0.119 \\ 0.651 & -0.508 & -0.193 & -0.190 \\ 0.758 & -0.583 & 0.224 & 0.272 \end{bmatrix} \quad (3.58a) \qquad \det \mathbf{F} = -0.699 \quad (3.58b)$$

Since inversion of a matrix is associated with division by its determinant, the larger the determinant of the instrument matrix, the better. A small determinant would indicate a near-singular matrix. In the real world, where the elements of the instrument matrix are always accompanied by a measurement uncertainty, inversion of a near-singular matrix would greatly amplify any error, eventually rendering the matrix useless. For ease of reference the inverse instrument matrix $\mathbf{F}^{-1}$ is also given here:

$$\mathbf{F}^{-1} = \begin{bmatrix} 0.434 & 0.311 & 0.186 & 0.172 \\ 0.536 & 0.417 & -0.843 & -0.550 \\ 0.580 & -0.404 & -0.262 & 0.233 \\ -0.537 & 0.361 & -2.108 & 1.825 \end{bmatrix} \tag{3.59}$$

The physical meaning of the rows and columns of the instrument matrix is discussed in detail in [33][1]. Each of the rows of **F** is associated with one of the polarimeter channels. More specifically, it follows from eq. (3.35) that the response of a channel to a particular incident polarization state, represented by a Stokes vector **S**, is determined by the scalar product of the corresponding row of **F** with **S**. If the incident light is unpolarized (eq. 2.71), the response is determined by the first element of that row. In other words, the first column of the instrument matrix specifies the DOAP response to unpolarized light, normalized per unit incident radiant flux. Because the polarimeter signals can only be non-negative, the elements in the first column of **F** must be positive (zero response to unpolarized light would indicate zero transmittance of the corresponding channel).

If the rows of **F** are interpreted as vectors in four-dimensional space, the polarimeter signals can be thought of as the projections of **S** along these vectors. Four independent projections are needed to fix **S** in four-dimensional space[2]. Because of this analogy, the rows of the instrument matrix are also called projection vectors. If these vectors and **S** are each normalized with respect to their first element, the four projections can easily be visualized in the three-dimensional Stokes subspace (§2.3.4). The normalized projection vectors (NPV's)

---

[1] Actually, in the cited reference the instrument matrix of a different device, the four-detector photopolarimeter (FDP), is discussed. However, the FDP and the DOAP are mathematically equivalent except for some of the constraints on the elements of the instrument matrix.

[2] If the number of available independent projections exceeds four, for instance in a polarimeter with more than four channels (detectors), then there may exist several distinct possible combinations of four projection vectors whose associated instrument matrices are all non-singular. In this case the Stokes vector **S** is overdetermined, and an average of several determinations of **S** can be taken to improve the accuracy and precision of measurement [34].

are defined by:

$$\mathbf{f}_i = \begin{bmatrix} \frac{F_{i1}}{F_{i0}} & \frac{F_{i2}}{F_{i0}} & \frac{F_{i3}}{F_{i0}} \end{bmatrix}^t \quad , \quad i = 0,1,2,3 \tag{3.60}$$

F is non-singular if these vectors do not all lie in the same plane.

In terms of the four NPV's, eq. (3.35) can now be written as:

$$I_i = F_{i0} \cdot S_0 \cdot (1 + \mathbf{f}_i \cdot \mathbf{s}) \quad , \quad i = 0,1,2,3 \tag{3.61}$$

s denotes the normalized Stokes vector in the Stokes subspace:

$$\mathbf{s} = \begin{bmatrix} \frac{S_1}{S_0} & \frac{S_2}{S_0} & \frac{S_3}{S_0} \end{bmatrix}^t \tag{3.62}$$

Equation (3.61) states that a signal is maximum when the incident light is totally polarized ($|\mathbf{s}| = 1$) and its Stokes vector parallel to the corresponding projection vector. It is minimum when the incident light is totally polarized and its Stokes vector antiparallel to the corresponding projection vector. Put differently, the polarization state that yields minimum signal is orthogonal to that which yields maximum signal. The average signal is equal to the response to unpolarized light[1] ($\mathbf{s} = 0$) or light whose Stokes vector is perpendicular to the corresponding projection vector ($\mathbf{f}_i \cdot \mathbf{s} = 0$).

It also follows from eq. (3.61) that, since F_{i0} and S_0 are both positive, the length of the NPV's cannot exceed 1. A NPV will be of unit length if the last element in the optical train of that particular channel (prior to the photodetector) is an ideal polarizer (analyzer). In that case, the minimum signal will be zero, and if **s** were to scan the entire surface of the unit sphere in the Stokes subspace the modulation[2] of the signal would be one.

With **F** from eq. (3.59), the four normalized projection vectors are:

$$\begin{aligned} \mathbf{f}_0 &= [0.265 \quad 0.924 \quad -0.133]^t \\ \mathbf{f}_1 &= [0.256 \quad -0.894 \quad 0.097]^t \\ \mathbf{f}_2 &= [-0.780 \quad -0.296 \quad -0.292]^t \\ \mathbf{f}_3 &= [-0.769 \quad 0.296 \quad 0.359]^t \end{aligned} \quad , \quad \begin{aligned} |\mathbf{f}_0| &= 0.970 \\ |\mathbf{f}_1| &= 0.935 \\ |\mathbf{f}_2| &= 0.884 \\ |\mathbf{f}_3| &= 0.899 \end{aligned} \tag{3.63}$$

---

[1] Remember that unpolarized light can be thought of as the superposition of two polarized waves of equal amplitude and orthogonal polarizations.

[2] Defined as $(I_{max}-I_{min})/(I_{max}+I_{min})$. Also known in optics as the contrast or visibility.

Although the last (polarization-altering) element in all channels of the PSD is a prism polarizer, a reduction in the length of the NPV's is expected because of the fibers delivering the light to the photodetectors. A slower DOAP described in [35] did not utilize fibers. The reported NPV's for that instrument do, indeed, have lengths that are closer to one.

The four characteristic Stokes vectors that result in maximum signals can be derived from eq. (3.63). They are listed below, together with the ellipticity angles and azimuths of the polarization ellipses that they describe:

$$\begin{aligned}
\mathbf{S}_0 &= [1 \quad 0.273 \quad 0.952 \quad -0.137]^t & (\varepsilon_0 &= -3.94°,\ \theta_0 = 37.0°) \\
\mathbf{S}_1 &= [1 \quad 0.274 \quad -0.956 \quad 0.104]^t & (\varepsilon_1 &= 2.98°,\ \theta_1 = -37.0°) \\
\mathbf{S}_2 &= [1 \quad -0.882 \quad -0.335 \quad -0.330]^t & (\varepsilon_2 &= -9.65°,\ \theta_2 = -79.6°) \\
\mathbf{S}_3 &= [1 \quad -0.856 \quad 0.329 \quad 0.399]^t & (\varepsilon_3 &= 11.8°,\ \theta_3 = 79.5°)
\end{aligned} \tag{3.64}$$

3.8.2.5.1 Verification

Upon completion of the calibration and with the PSG and the PSD still set up in the straight-through mode, a verification procedure was started to check the validity of the newly obtained instrument matrix. With the linear polarizer fixed at P = 0, the QWR was rotated through a complete circle in steps of 10°, thus generating a variety of polarization states that were measured with the DOAP. The measured Stokes parameters were then compared to the predicted Stokes parameters, that are given by:

$$\mathbf{S}_{PSG} = \begin{bmatrix} 1 \\ \cos^2 2Q \\ 0.5 \cdot \sin 4Q \\ \sin 2Q \end{bmatrix} \tag{3.65}$$

as follows from eq. (3.23) in its normalized version and with P set zero.

Figure (3.18) shows the results of the verification that was carried out immediately after the calibration which led to the instrument matrix of eq. (3.58a). The maximum deviations of the measured from the predicted parameters were 0.041 for S_1, 0.014 for S_2, and 0.066 for S_3. The average deviations were 0.019 for S_1, 0.005 for S_2, and 0.028 for S_3. The measured degree of polarization is also plotted in the same figure. Its mean value was 1.004, with a standard deviation of 0.024.

3.8.2.5.2 Prism - Check

After calibration and verification the PSG was returned to the measurement position and the PSD was aligned using a prism, as described in §(3.8.2.2). As a final check before the prism was removed, a measurement, consisting of 2048 data points, was taken. The index of refraction n and the extinction coefficient k of the prism material (BK7 optical glass) were computed and compared with the 'should be' values. This convenient quick check was also done routinely in-between calibrations to realign the PSD and ensure that the instrument matrix in use was still valid. To check the linearity of the system, the measurement was repeated at different signal levels by changing the neutral density filter in front of the linear polarizer in the PSG. A total of three neutral density filters with varying transmittances was used. A slight tendency for the measured n to increase with increasing signals was observed. Nevertheless, this occurred when the signals by far exceeded (three to four times higher) typical signals recorded during measurements on cylindrical specimens. The relative difference between the value of n obtained with the highest signals and that obtained with the lowest signals was approximately 1%.

Figure (3.19) shows the results of a prism-check, including the raw signals (lowest of the three levels). The average measured n was 1.520 with a standard deviation of 0.032 (≈2%) compared to the published value of 1.51370[1] at 677 nm. The average measured k was 0.007 with a standard deviation of 0.11. The extinction coefficient should, of course, be exactly zero for a dielectric. The value of the spectral normal (-hemispherical)[2] reflectance at 677 nm, computed from the measured n and k (eq. 2.102), was 0.0426.

In all the prism checks that were done in the course of this work, the measured values for the index of refraction of the prism were always higher than the published value. The average deviation, when the signals in the prism check were comparable in magnitude to those during measurements, was +1.7%. This points to a systematic error, which, unfortunately, could not be traced to its source.

---

[1] Source: Schott Optical Glass catalog 1995.

[2] See the comments at the end of §(2.3.6).

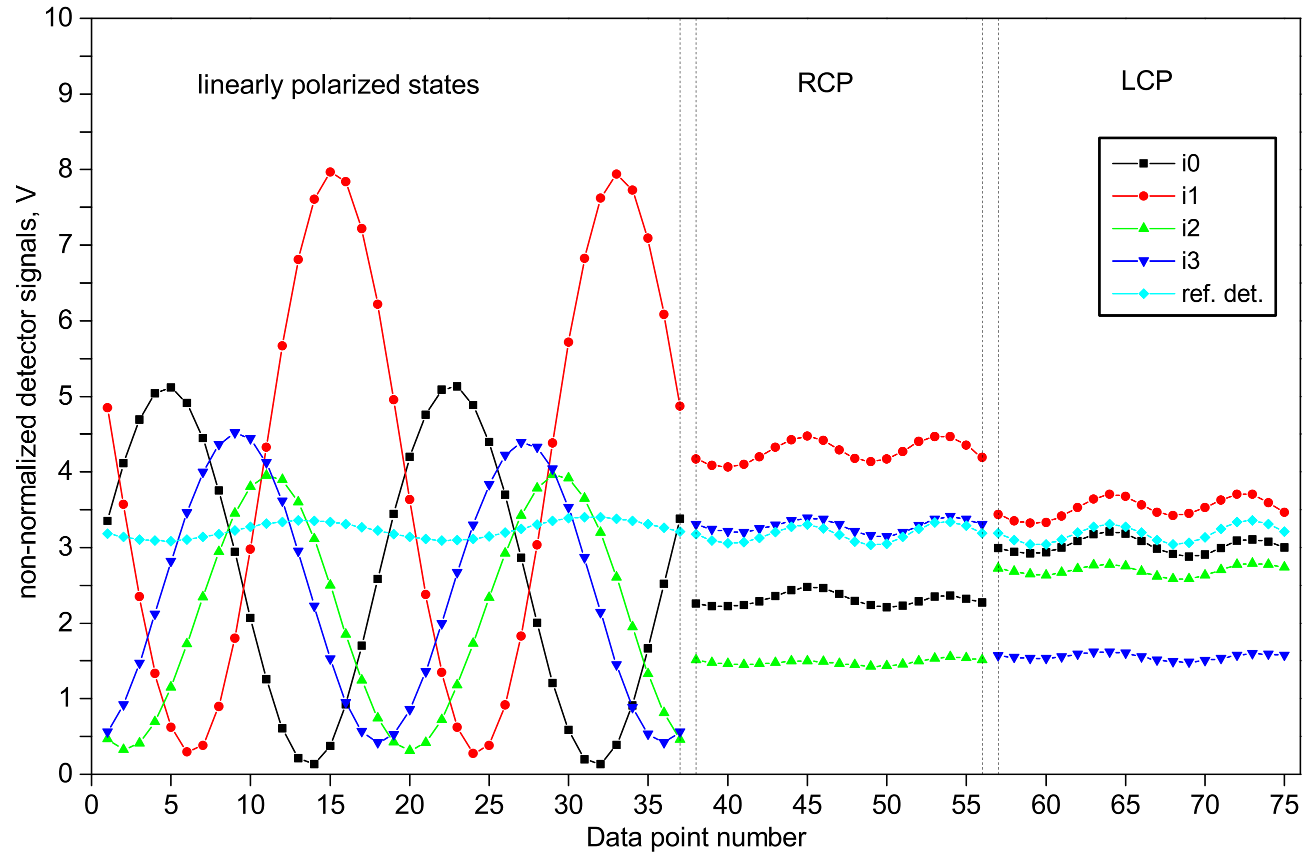

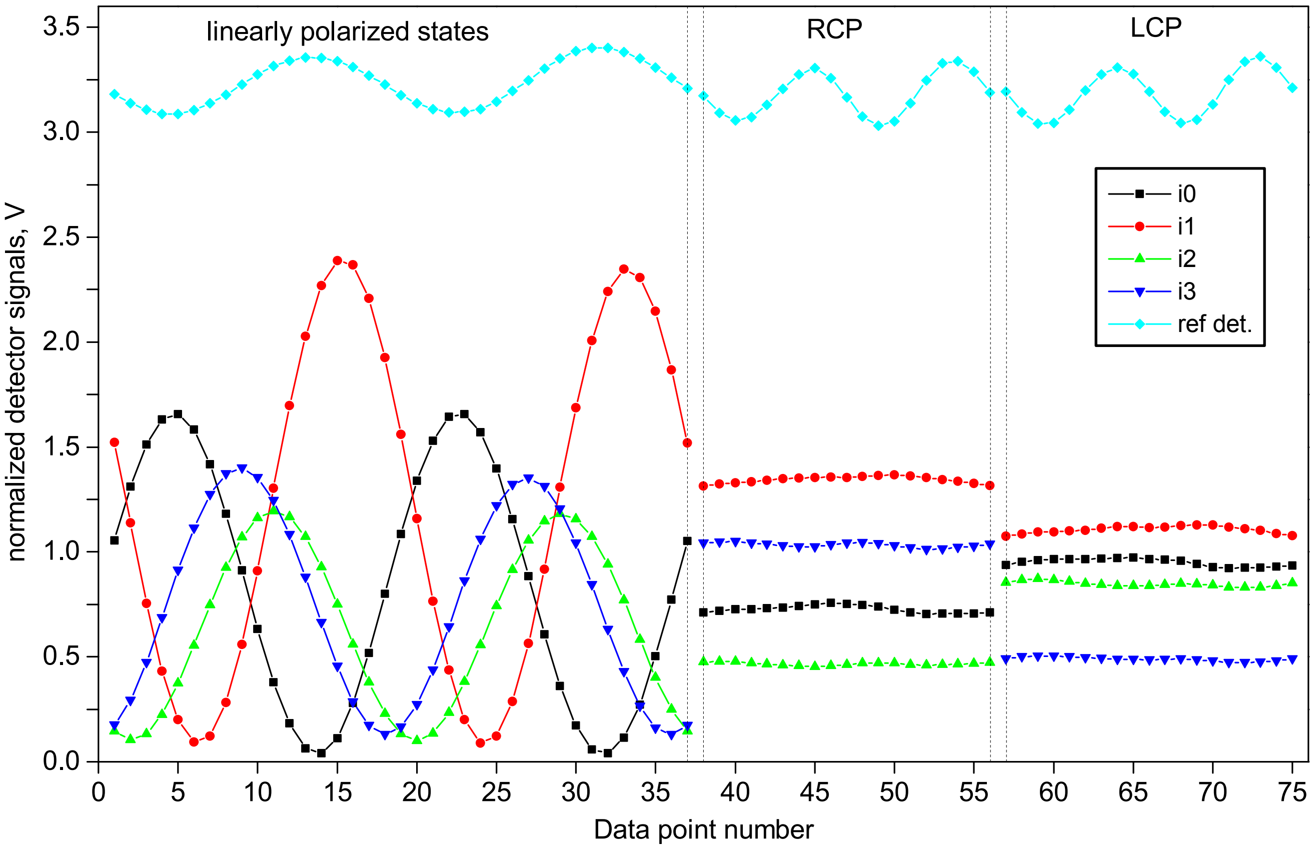

Fig. 3.16: The four polarimeter signals recorded during a equator-poles calibration. Shown before (top) and after (bottom) normalization with respect to the reference detector signal.

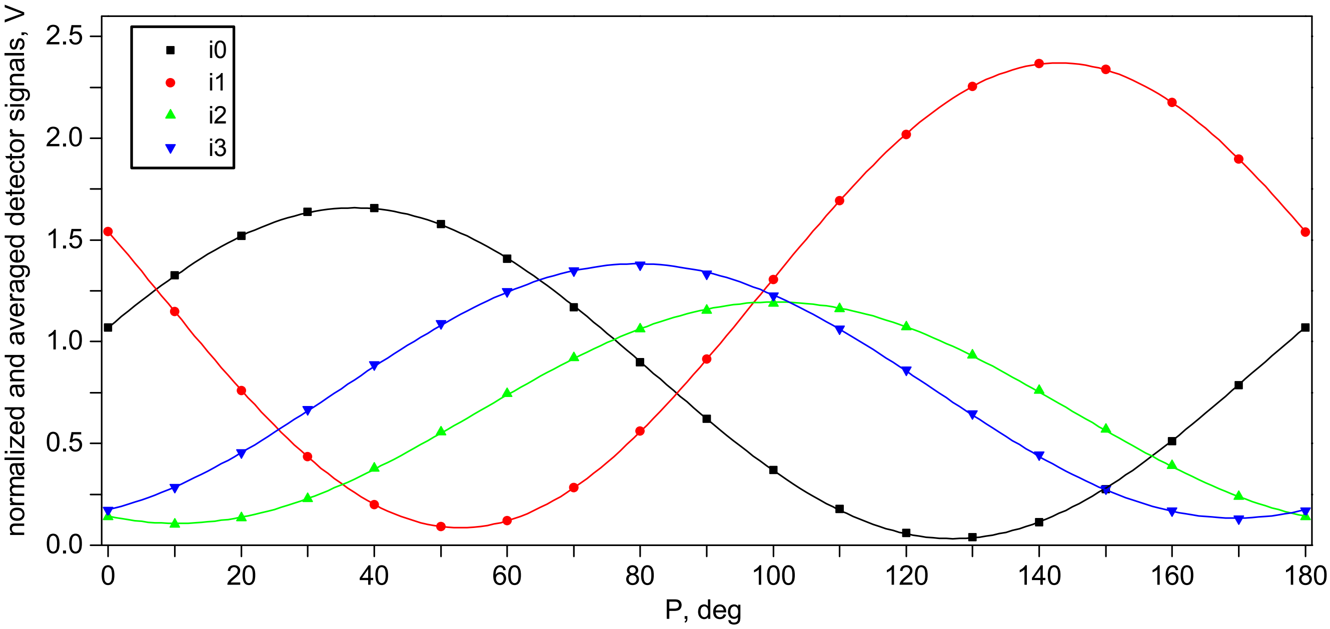

Fig. 3.17: The normalized instrument response to incident linearly polarized light as a function of the varying azimuth.

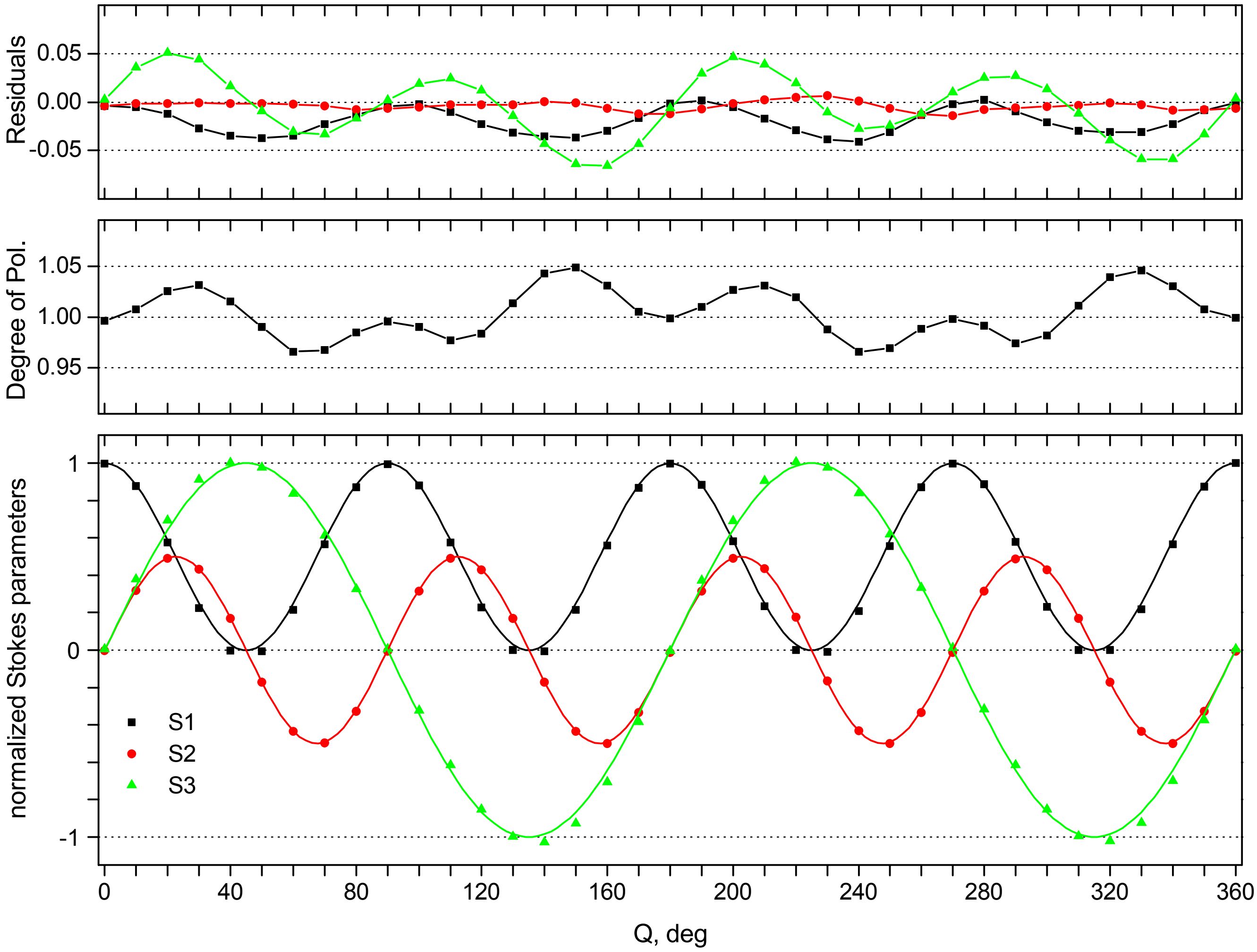

Fig. 3.18: Results of the verification procedure. In the bottom graph, the symbols represent the measured Stokes parameters S_1, S_2, and S_3, whereas the solid curves are plots of the predicted Stokes parameters, as a function of the QWR azimuth. The deviation of the measured from the predicted values is plotted in the top graph. The middle graph shows the degree of polarization of the measured Stokes vectors (values greater than one are, of course, the result of measurement errors).

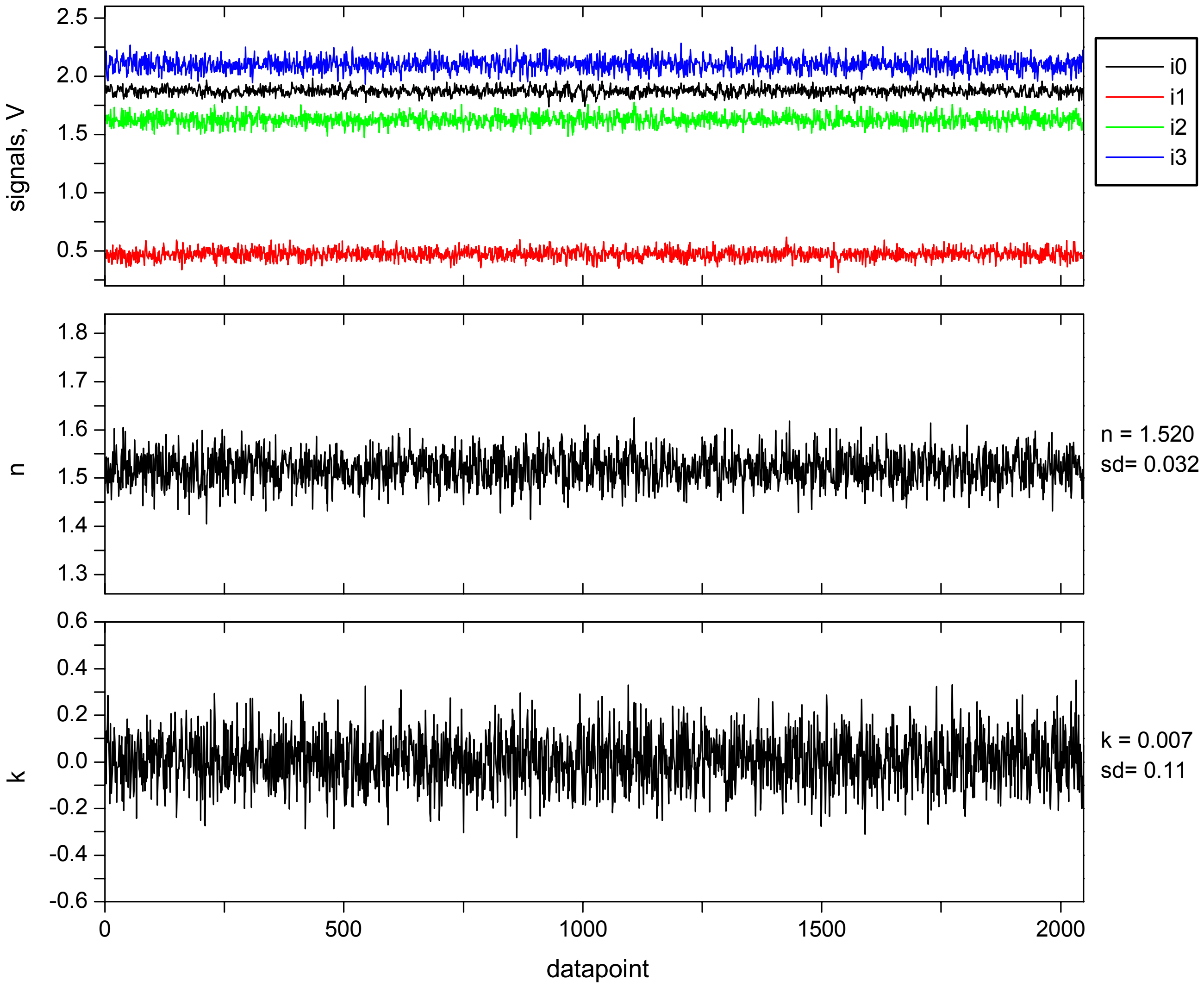

Fig. 3.19: Results of the latest prism-check. Shown from top to bottom are the DOAP raw signals, the index of refraction, the extinction coefficient, and the computed spectral normal (hemispherical) reflectance of the prism material (BK7 optical glass).

3.9 The data acquisition

The data acquisition system consisted mainly of four data acquisition boards installed in a PC. Each board featured two analog input channels, each with its own 12-bit A/D-converter, with a full scale input range of 0 to +10 V, a sampling rate of 2 MHz, and a sampling size of up to 4095 samples/channel. Two of the boards were used to acquire the demodulated polarimeter signals, the third board was used for the two radiometer outputs, and the last one for the current and voltage measurements. All four boards were triggered simultaneously by a TTL-signal generated by the DOAP electronics module.

A fifth, slower (16-bit, 160 kHz A/D-converter), data acquisition and I/O board was used primarily to control digital I/O operations of the timing and overload conditions of the DOAP electronics module. It was also used during polarimeter calibration to acquire the demodulated reference detector signal.

The radiometer, current, and voltage signals were also simultaneously acquired by a digital oscilloscope (four channels, 12-bit, 10 MHz max. sampling rate). Its was used in the trial discharges to adjust the tuning coil (§3.6) and for double-checking purposes.

4 DATA REDUCTION

4.1 Temperature

The thermodynamic temperature T of the specimen at each instant was obtained from its measured radiance temperature T_λ (§3.7.2) and normal spectral emittance $\varepsilon_n(\lambda,T)$ (§3.8.1) using eq. (2.52):

$$T = \frac{c_2}{n \cdot \lambda_{T_\lambda - T}} \cdot \frac{1}{\ln\left\{1 + \varepsilon_n\left(\lambda_{T_\lambda - T}, T\right) \cdot \left[\exp\left(\frac{c_2}{n \cdot \lambda_{T_\lambda - T} \cdot T_\lambda}\right) - 1\right]\right\}} \tag{4.1}$$

The implicit assumptions regarding the target size, field of view of the radiation thermometer, and constancy of the specimen emittance throughout the spectral passband of the radiation thermometer, that led to this expression, should of course be kept in mind (§2.2.3, §2.2.5). No correction was made to account for the difference in the operating wavelengths of the polarimeter and the radiometer.

In computing radiance temperature, the mean effective wavelength $\lambda_{T_0\text{-}T_\lambda}$ was assumed constant at 656.3 nm throughout the covered temperature range, as explained in §(3.7.3). In converting radiance temperature to thermodynamic temperature, the mean effective wavelength between a different pair of temperatures has to be used. Namely, between the radiance temperature and the thermodynamic temperature of the specimen. Since T depends on the normal spectral emittance of the specimen, so does $\lambda_{T_\lambda\text{-}T}$. However, the error caused by the use of $\lambda_{T_\lambda\text{-}T} = 656.3$ nm for this computation as well, was negligible compared to the overall uncertainty caused by the uncertainty in the normal spectral emittance. $\lambda_{T_\lambda\text{-}T}$ as a function of T_λ for three values of normal spectral emittance is shown in fig. (4.1). For ease of comparison, $\lambda_{T_0\text{-}T_\lambda}$ from fig. (3.11) is also shown. Figure (4.2) shows the error caused by the use of a constant value of 656.3 nm for $\lambda_{T_\lambda\text{-}T}$, as a function of radiance temperature in the range 1500 to 3000 K.

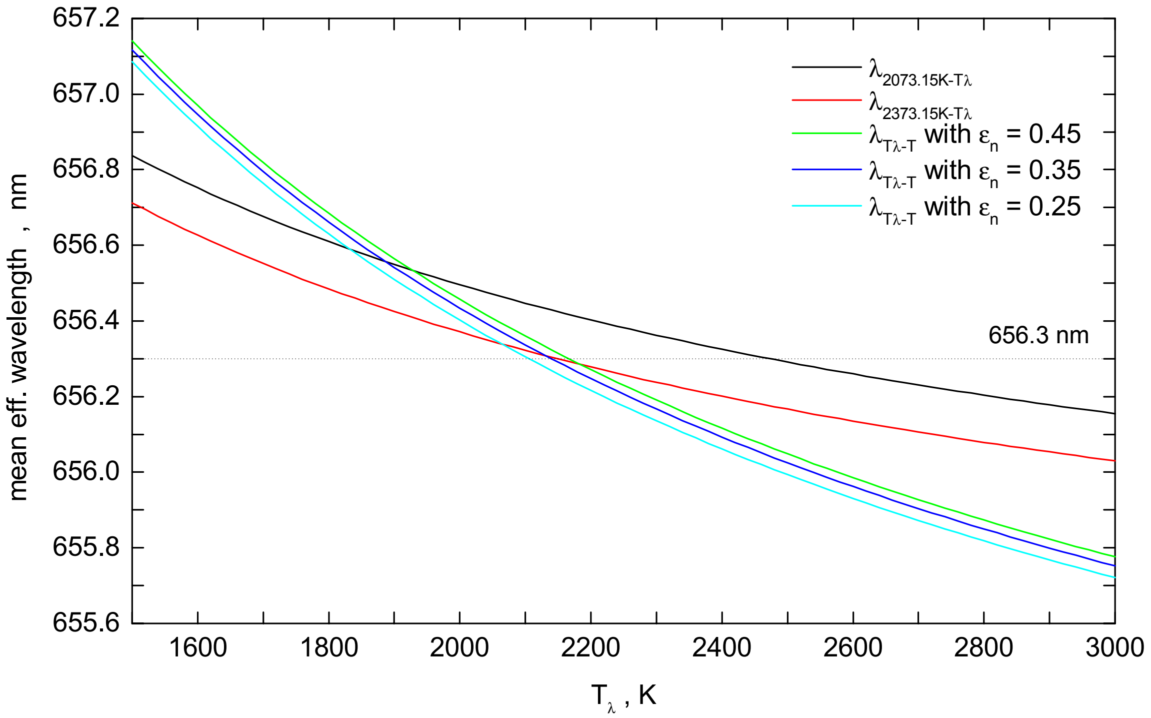

Fig. 4.1: The mean effective wavelength $\lambda_{T_\lambda\text{-}T}$ as a function of radiance temperature T_λ, computed for three values of normal spectral emittance ε_n. $\lambda_{T_0\text{-}T_\lambda}$ from fig. (3.11) is also shown here for ease of reference.

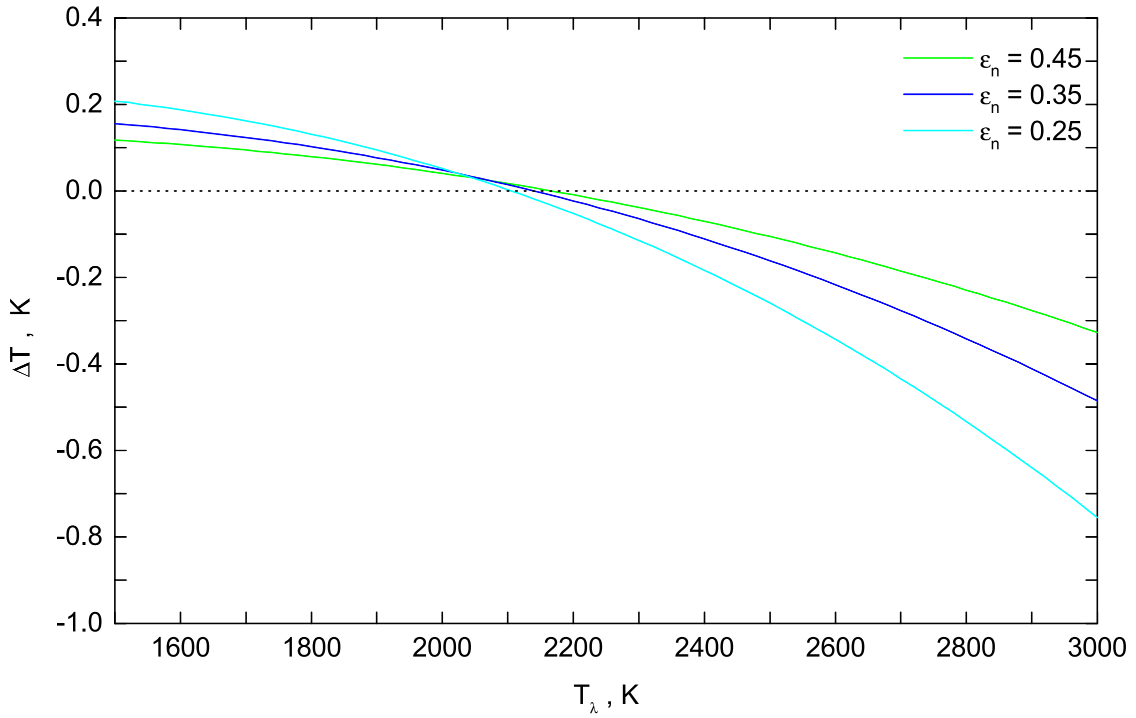

Fig. 4.2: Error in the computed thermodynamic temperature T, caused by the use of a constant value $\lambda_{T_\lambda\text{-}T} = 656.3$ nm in the conversion of T_λ to T, shown as a function of radiance temperature T_λ for three values of normal spectral emittance ε_n.

4.2 Electrical resistivity

The specimen resistance at each instant, was determined from the measured voltage U across the effective[1] specimen length l_{eff} and the measured current I through the specimen. Computing resistivity requires knowledge of the specimen dimensions as a function of time, as well. Since no experimental means were available to measure thermal expansion, the resistivity data reported in this work are based on the room-temperature specimen dimensions. They were obtained using[2]:

$$\rho_{\text{el}} = \frac{U}{I} \cdot \frac{\gamma_{\text{lin}}}{\gamma_0 \cdot l_{\text{eff}}} \tag{4.2}$$

where γ_{lin} is the linear density of the specimen (mass per length) and γ_0 is its density at room-temperature. Prior to pulse-heating a specimen, its linear density was derived from a weight measurement, using a precision scale, and a length measurement, using a traveling microscope. This proved more reliable than a direct measurement of the specimen diameter. By measuring the linear density of each individual specimen, small differences in the specimen diameter, caused, for instance, by different degrees of polishing, could be taken into account. The average value of γ_{lin} for the niobium specimens was 1.682×10^{-2} kg·m^{-1}, and for the titanium specimens 0.8490×10^{-2} kg·m^{-1}. For the density γ_0, values of 8570 kg·m^{-3} and 4540 kg·m^{-3} were used for niobium and titanium, respectively.

Having obtained the 'uncorrected' electrical resistivity using eq. (4.2), it is a simple matter to account for thermal expansion if such data are available from literature:

$$\rho_{\text{el,c}} = \rho_{\text{el}} \cdot \left(\frac{r}{r_0}\right)^2 \tag{4.3}$$

The subscript 'c' stands for 'corrected'. r_0 denotes the specimen radius at room temperature, r the specimen radius as a function of temperature[3].

For each experiment the thermodynamic temperature was plotted against resistivity. A plateau

---

[1] The effective specimen length was defined by the distance of the voltage probes (§3.6) and was measured using a traveling microscope.

[2] Although the symbol ρ has already been used to denote reflectance, it will always be clear from the context and the different subscripts which quantity is actually meant.

[3] Thermal expansion was only possible in the radial direction because the specimens were tightly clamped at both ends. In addition, buckling does not take place at sufficiently high heating rates [19, 36].

indicated melting of the specimen. Linear functions were fitted to the data in the solid phase and in the liquid phase. In the case of niobium a linear function was also fitted to the data in the melting plateau. The intersections of the melting-plateau fit with the solid-phase fit and with the liquid-phase fit provided the resistivity values at the start and at the end of melting, respectively. In the case of titanium, however, resistivity changed little during melting. Fitting a straight line to such a short melting plateau (in terms of resistivity change) was impractical. In order to obtain the resistivity values at the start and at the end of melting the solid- and liquid-phase fits were extrapolated to the average measured melting temperature, instead. Using the fits obtained from each experiment in the solid and in the liquid phase, resistivity was computed every 50 K in the temperature range of interest. At each of these temperatures (every 50 K) the mean of the individual-experiment-values was computed. Linear functions were then fitted to these mean resistivity values from all experiments, in the solid and in the liquid phase.

4.3 Specific enthalpy

The specific energy absorbed by the specimen during heating, as a function of time, was obtained from the integral of imparted electrical power over time, divided by the number of moles of the 'effective' specimen:

$$\Delta q(t) = \frac{M}{\gamma_{\mathrm{lin}}\, l_{\mathrm{eff}}} \int_0^t U(t')I(t')\,dt' \qquad (4.4)$$

where M is the molar mass of the specimen material. For niobium $M = 92.91\times10^{-3}$ kg·mol^{-1} and for titanium $M = 47.88\times10^{-3}$ kg·mol^{-1} was used.

For an isobaric experiment, the increase in the specific enthalpy h of the specimen is equal to the electrical energy Δq(t) absorbed by it during heating:

$$\Delta h(t) = h(t) - h_0 = \Delta q(t) \qquad (4.5)$$

h_0 denotes the specific enthalpy at room temperature and ambient pressure.

At the temperatures and speeds involved in the present work, the only significant heat loss from the specimen can be that due to thermal radiation. Using the Stefan-Boltzmann law that relates the total self-exitance of a surface element to the fourth power of its temperature, this heat loss can be estimated. With an effective specimen length of 23 mm and a specimen radius of 0.8 mm, we obtain values[1] of 687 W and 154 W for the emitted radiant power at 3200 K and 2200 K, respectively. These two temperatures correspond to the upper limit of the temperature ranges in which data for niobium and titanium are reported in this work. At that point of the discharge (near the experiment end), the imparted electrical power was approximately 4 MW, in the case of niobium, and larger than 1 MW in the case of titanium. Thus, at the highest temperatures, the heat losses due to thermal radiation represented less than 0.02% of the imparted power and could be neglected without significant reduction in accuracy.

4.4 Heat of fusion

To obtain the heat of fusion, the temperature was plotted as a function of Δh. A plateau in that plot indicated melting of the specimen. In the case of niobium, a quadratic function was fitted to the solid-phase data and linear functions were fitted to the melting plateau and to the data in the liquid phase. For titanium linear functions were fitted to the data in the solid phase, the melting plateau and in the liquid phase. The intersections of these three fits were used to define the beginning and the end of melting. The heat of fusion h_F was then computed as the increase in specific enthalpy between the beginning and the end of the melting plateau.

4.5 Specific heat capacity

The specific heat capacity at constant pressure c_p, is equal to the derivative of specific enthalpy with respect to temperature:

$$c_p = \left(\frac{\partial h}{\partial T} \right)_{p=\mathrm{const.}} \tag{4.6}$$

Having already obtained functions of temperature vs. specific enthalpy (§4.4), c_p was computed as the reciprocal of the slope dT/dh of these functions.

4.6 Thermal conductivity and thermal diffusivity

The principal mechanism for thermal conduction in pure metals in the liquid state is through the transport of electrons. Although lattice conduction can make a significant contribution at

---

[1] These values were computed using a value of one for the total-hemispherical emittance of the specimen surface. The increase in specimen radius because of thermal expansion was not accounted for.

lower temperatures, electronic conduction is dominant at temperatures around the melting point [37]. Under these conditions, thermal conductivity[1] λ can be derived from electrical resistivity using the Wiedemann-Franz-Lorenz law:

$$\lambda = \frac{L_0 \cdot T}{\rho_{el,c}} \tag{4.7}$$

where T is the thermodynamic temperature, $\rho_{el,c}$ is the 'corrected' electrical resistivity, and $L_0 = 2.45 \times 10^{-8}\ \mathrm{W \cdot \Omega \cdot K^{-2}}$ is the theoretical Lorenz number (as given by Sommerfeld). However, data computed using eq. (4.7) should only be regarded as estimates, since experimentally determined values for the Lorenz number can vary with temperature and specimen material.

Thermal diffusivity α is related to thermal conductivity by:

$$\alpha = \frac{\lambda \cdot M}{c_p \cdot \gamma} = \frac{L_0 \cdot T \cdot M}{\rho_{el} \cdot c_p \cdot \gamma_0} \tag{4.8}$$

c_p is the specific heat capacity (expressed in $\mathrm{J \cdot mol^{-1} \cdot K^{-1}}$), M denotes the molar mass of the specimen, γ is the density as a function of temperature, γ_0 is the density at room temperature, and ρ_{el} denotes the electrical resistivity based on the room-temperature dimensions of the specimen.

---

[1] The symbol λ has been used throughout this work to denote wavelength. It is reintroduced here because of its widespread use in the materials-science literature, where it refers to thermal conductivity. It will always be clear from the context, which meaning is attributed to λ.

5 EXPERIMENTS

5.1 Measurements on niobium

The purity of the niobium material was 99.9+%. The impurities, as reported by the manufacturer, were: Ta, 100 ppm; O, 73 ppm; W, 50 ppm; N, 29 ppm; Zr, Mo, Ti, Fe, Ni, Si, Mn, Ca, Al, Cu, Sn, Cr, V, Co, Mg, Pb, and Hf, each less than 20 ppm; and C, H, B, and Cd, together less than 21 ppm.

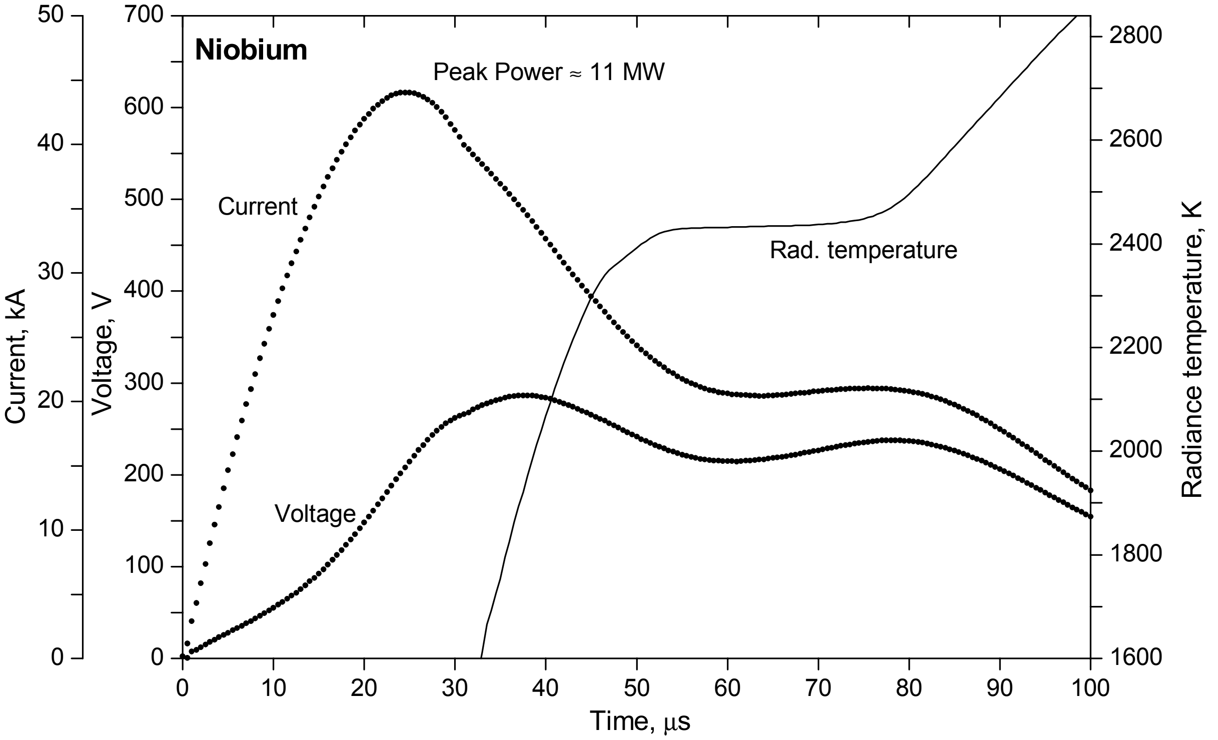

Fig. 5.1: Current, voltage, and radiance temperature at 656.3 nm, as functions of time, during a pulse-heating experiment with niobium.

In a typical experiment, the capacitor bank was charged to 6.6 - 6.7 kV and discharged in the crowbar-mode of operation (§3.4). The specimen was heated from room temperature to its melting point in approximately 50 µs. After 100 µs, it reached a radiance temperature of approximately 2850 K, corresponding to a true temperature close to 3300 K. Figure (5.1) shows the time variation of current, voltage, and radiance temperature at 656.3 nm, during an experiment with niobium. The peak current through the specimen was about 45 kA and the peak voltage across its effective length was close to 275 V. The apparent phase difference between current and voltage is most likely due to the rapidly increasing resistance of the specimen as it heats. The peak electrical power imparted on the specimen was approximately

11 MW. The plateau in the radiance temperature trace indicates the melting of the specimen. The heating rate in the solid phase, at about 200 K below the melting point, was approximately 5×10^7 K·s^{-1}.

Though some of the specimens were used 'as received', most of them were given some treatment prior to pulse-heating in the capacitor-discharge circuit. The purpose of this treatment was to improve the specimen surface for the polarimetric measurement by removing possible oxide layers and making the surface more specular. These two conditions of an oxide-free, specular surface, had to be met as closely as possible, in order to justify the use of the Fresnel-equations (eqs. 2.87a and 2.87b).

To achieve this goal, some of the specimens were finely ground, some were subjected to one or two 'pre-heating' pulses prior to the experiments, and some were both ground and pre-heated. Grinding was done in successively finer steps, using silicon carbide sheets down to 4000-grade. Pre-heating was done using the millisecond-resolution pulse-heating system at NIST [1]. This system is designed for highly accurate thermophysical property-measurements of electrically conducting materials up to their melting range. It uses a battery bank for energy storage, a variable resistor for rough control of the heating rate, and a computer-controlled FET-switch for accurate control of the current through the specimen [38]. The temperature is determined by means of radiation thermometry and millisecond-resolution laser polarimetry. The radiometer output is coupled to the FET-switch via a feedback algorithm that allows heating the specimen to a preset radiance temperature and holding it at that temperature for a specified amount of time (up to 20 s). All pre-heating pulses were carried out in argon, at slightly above atmospheric pressure. They were about 250 ms in duration.

In order to obtain the optimum parameters for pre-heating, a series of trials was conducted on 'as received' specimens. The results are summarized in figs. (5.2) - (5.7). In general, it was observed that some surface cleaning took place in the first shot, provided the temperature was high enough, which manifested itself in a 'bumpy' emittance[1] trace. As a consequence, the room-temperature emittance (after the specimen had cooled off again) decreased significantly. Subsequent pre-heating pulses on the same specimen to the same radiance temperature (but

---

[1] All emittance values reported in this section in conjunction with pre-heating, are normal spectral emittance values at 633 nm, the wavelength of the He-Ne laser used with the millisecond-resolution polarimeter.

slightly higher true temperature because of the lower emittance), exhibited a much smoother and very reproducible decrease in emittance with temperature. In addition, the room-temperature emittance did not decrease significantly with subsequent pre-heating pulses to the same temperature.

Figure (5.2) shows the radiance and true temperature traces, as functions of time, during two pre-heatings to 1800 K radiance temperature[1], conducted on the same specimen (Nb1). The second pre-heating took place two days after the first one, during which time the specimen remained in the experiment chamber but was exposed to air. Figure (5.3) shows the pre-heating of a different specimen (Nb8) to a higher temperature, in which the same 'bumpy' emittance is observed. Despite the higher temperature, the emittance at the peak temperature dropped to the same value it had dropped to during the lower temperature pre-heating pulse. Also, the decrease in the room-temperature value of emittance was the same as in the lower temperature pre-heating.

Figures (5.4) and (5.5) offer a different view of the emittance vs. true temperature traces of the previous two figures. It is interesting to see that there is some hysteresis between the heating and cooling branches of the curves. Its width was always large in the first shot, as expected, since the cleaning of the surface could not be undone. The remaining hysteresis in subsequent pre-heating shots could not be explained. It probably indicated some surface changing process that could not keep pace with heating and continued to take place in the initial cooling period, when the temperature was still high.

Figure (5.6) shows the change in room-temperature emittance of several specimens, after one or more pre-heating pulses. Specimens Nb1, Nb2, and Nb3 (upper row), were heated to 1800 K in radiance temperature. In the middle row (specimens Nb8, Nb9, and Nb10), the peak radiance temperature was nominally 2000 K. No significant difference was observed between the higher and lower temperature pulses, with respect to their effect on room-temperature emittance. Specimens Nb1 and Nb10 were pre-heated twice. It is interesting to see, that the room-temperature emittance of specimen Nb1, rose slightly in the two days between the two pre-heatings, during which time it was exposed to air. This was not the case

---

[1] Radiance temperatures reported in this section in conjunction with the pre-heating experiments, were measured at the mean effective wavelength of the millisecond-system radiometer, which was approximately 651 nm.

with specimen Nb10, that was subjected to the second pre-heating pulse some ten minutes after the first one and remained in the argon atmosphere during this time. Specimen Nb15 was pre-heated several times to temperatures[1,2] that were increasingly close to the melting point of niobium (2422 K in radiance temperature at 653 nm, [39]). This was done in an effort to produce a mirror-like surface by surface-melting, and consequently increase the polarimeter signals.

Figure (5.7), which is the counterpart of the previous figure, shows the change in the room-temperature millisecond polarimeter signals after every pre-heating pulse. It can be seen, that after the ninth and tenth shot on specimen Nb15, the polarimeter signals did, indeed, all rise. However, it was rather difficult to achieve this result with all specimens. Often, after a pulse this close to the melting point, deep grain boundaries appeared on the specimen surface. Though the individual grains themselves were very shiny, the grain boundaries had a deteriorating effect on the reflected laser beam (scattering) and the polarimeter signals.

Therefore, this effort was abandoned. Instead, it was decided to pre-heat the specimens only to a radiance temperature (at 651 nm) of 1750 to 2000 K, corresponding to a thermodynamic temperature of 1880 to 2170 K, which was enough to produce the ‘cleaning’ effect described above.

---

[1] The temperatures shown in figs. (5.6) and (5.7) for the pre-heating pulses on Nb15, are inaccurate (lower) by a few degrees. The error was probably caused by an old transmittance value for the neutral density filter that had to be placed in front of the radiometer in this high-temperature pre-heating series. In other words, the actual temperatures were even closer to the melting point of niobium.

[2] Unfortunately, some data of the first and eighth pre-heating pulses on Nb15 were not saved properly. The radiance temperatures shown in figs. (5.6) and (5.7) (2400 K and 2410 K) are the nominal peak radiance temperatures, to which the system was preset. The actual values could have differed by 1-2 K. The corresponding values of peak true temperature could not be recovered.

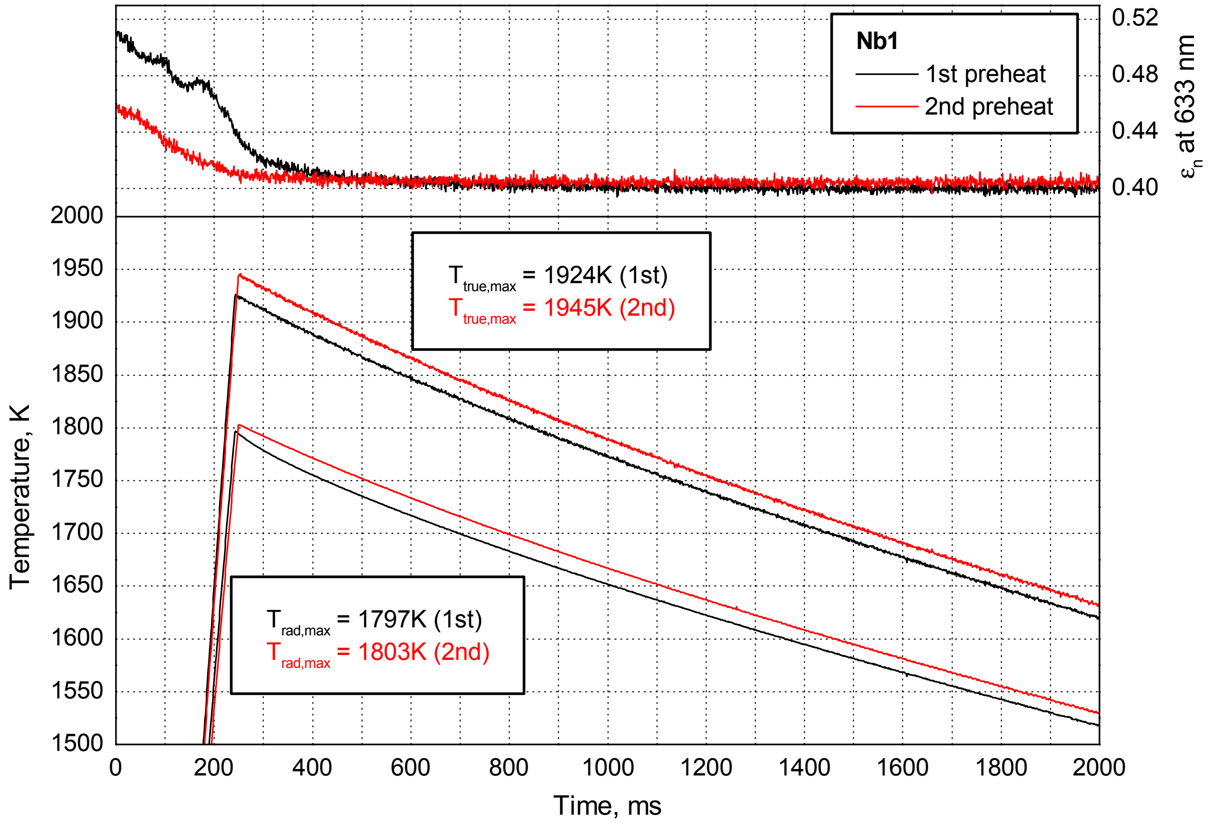

Fig. 5.2: Pre-heating specimen Nb1 twice to a nominal radiance temperature of 1800 K at 651 nm, using the slow millisecond-system. The second preheat was done two days after the first one. The radiance and thermodynamic temperature traces, as well as normal spectral emittance at 633 nm, are shown as functions of time.

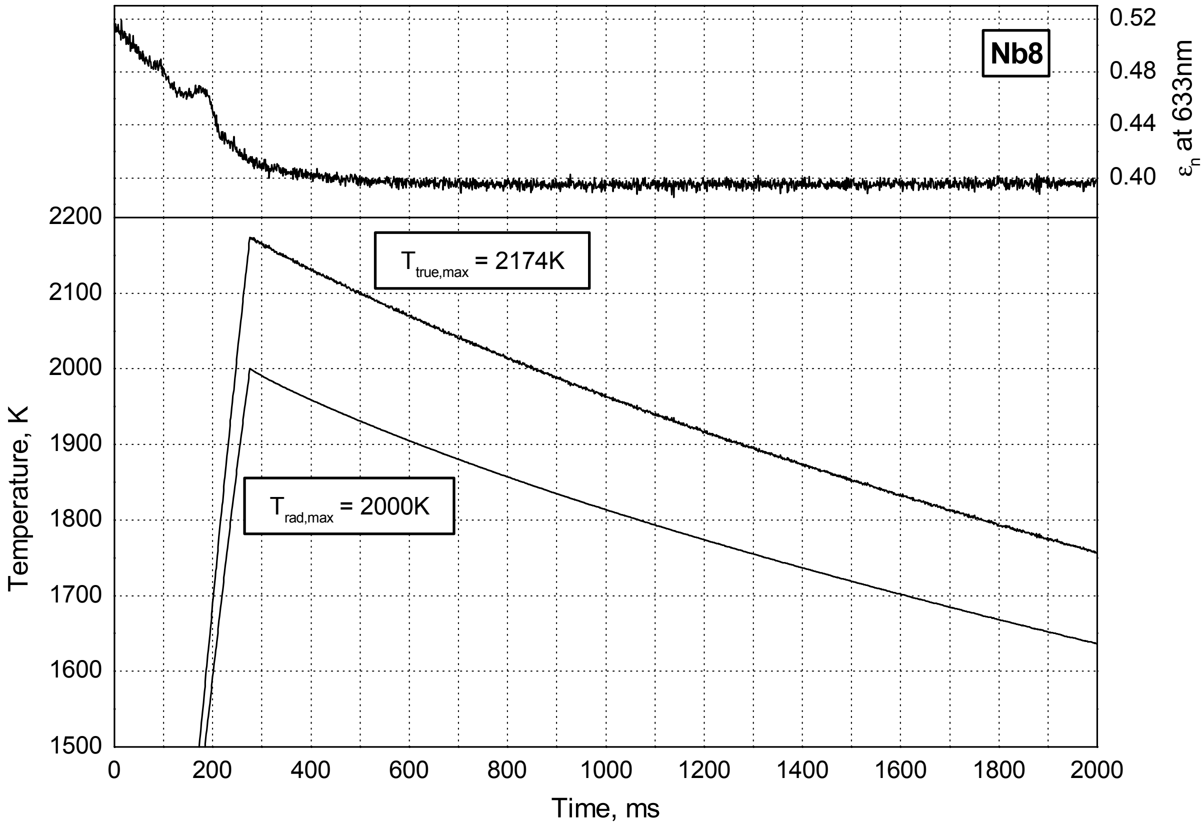

Fig. 5.3: Pre-heating specimen Nb8 to a radiance temperature of 2000 K at 651 nm, using the slower millisecond-system. The radiance and thermodynamic temperature traces, as well as normal spectral emittance at 633 nm, are shown as functions of time.

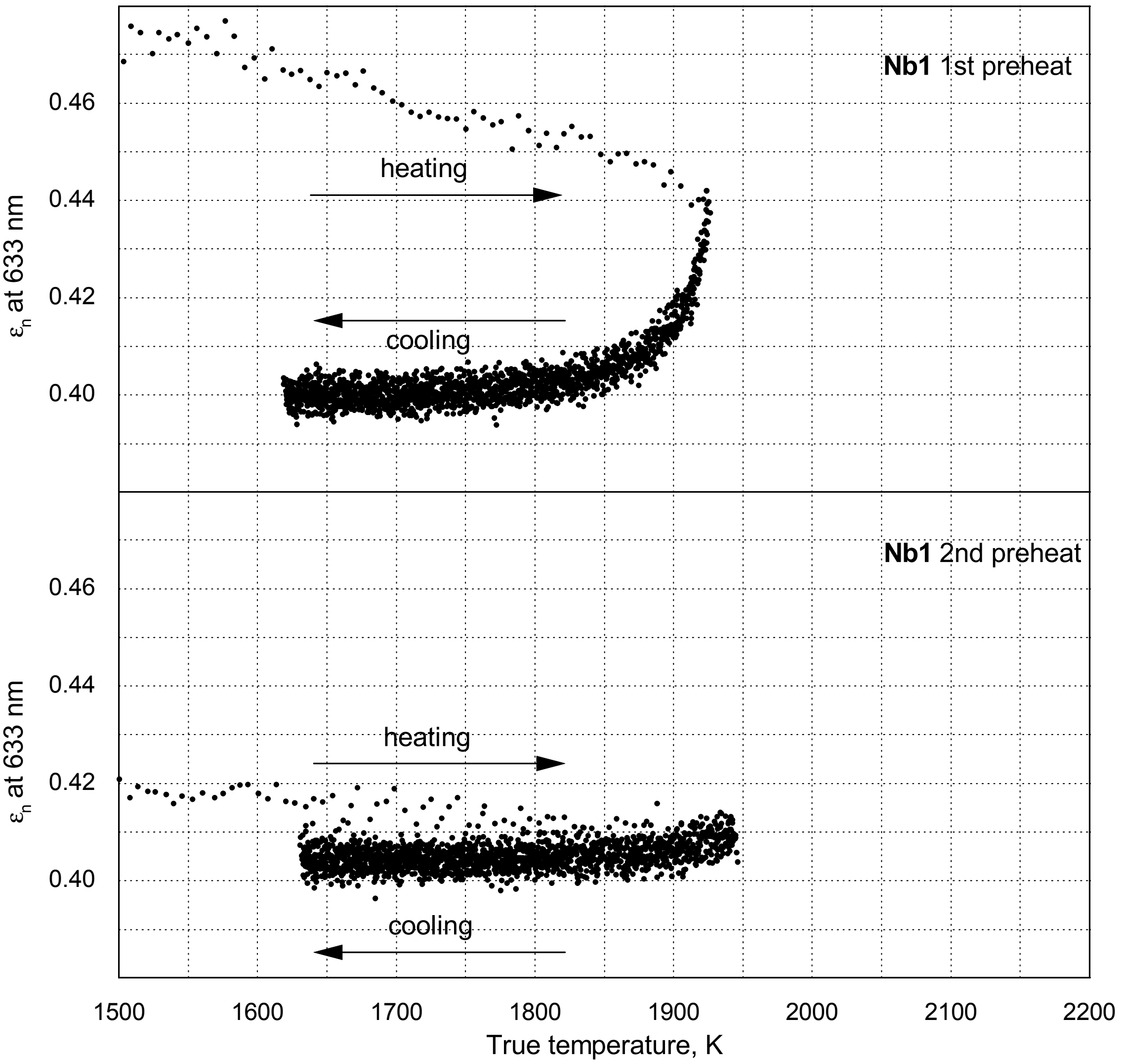

Fig. 5.4: Pre-heating specimen Nb1 twice to a nominal radiance temperature of 1800 K at 651 nm, using the slower millisecond-system. The second preheat was done two days after the first one. The normal spectral emittance at 633 nm is shown as a function of thermodynamic temperature during pulse-heating and subsequent natural cooling.

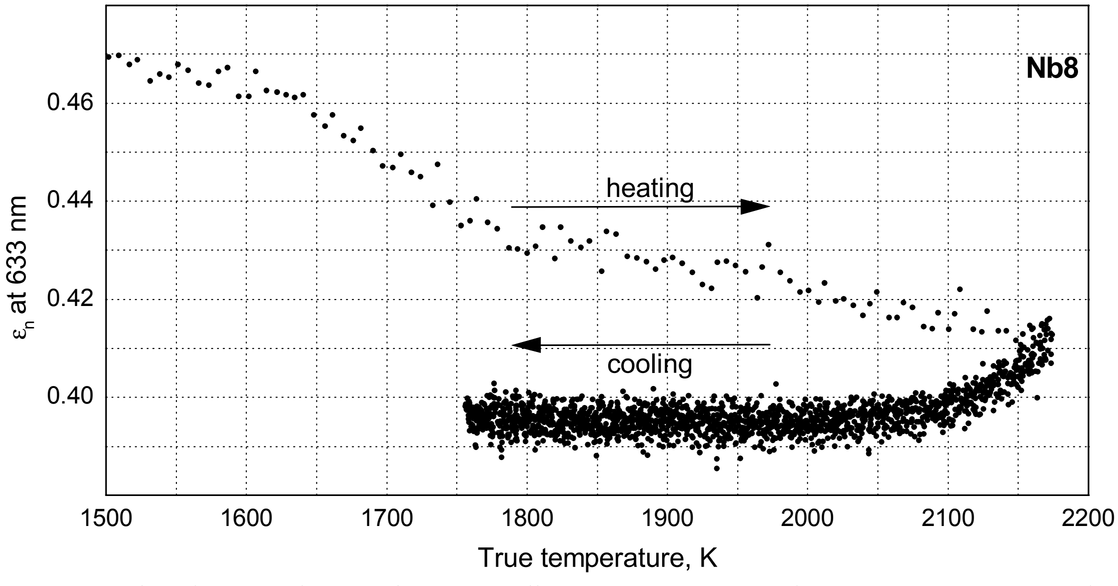

Fig. 5.5: Pre-heating specimen Nb8 to a radiance temperature of 2000 K at 651 nm, using the slower millisecond-system. The normal spectral emittance at 633 nm is shown as a function of thermodynamic temperature during pulse-heating and subsequent natural cooling.

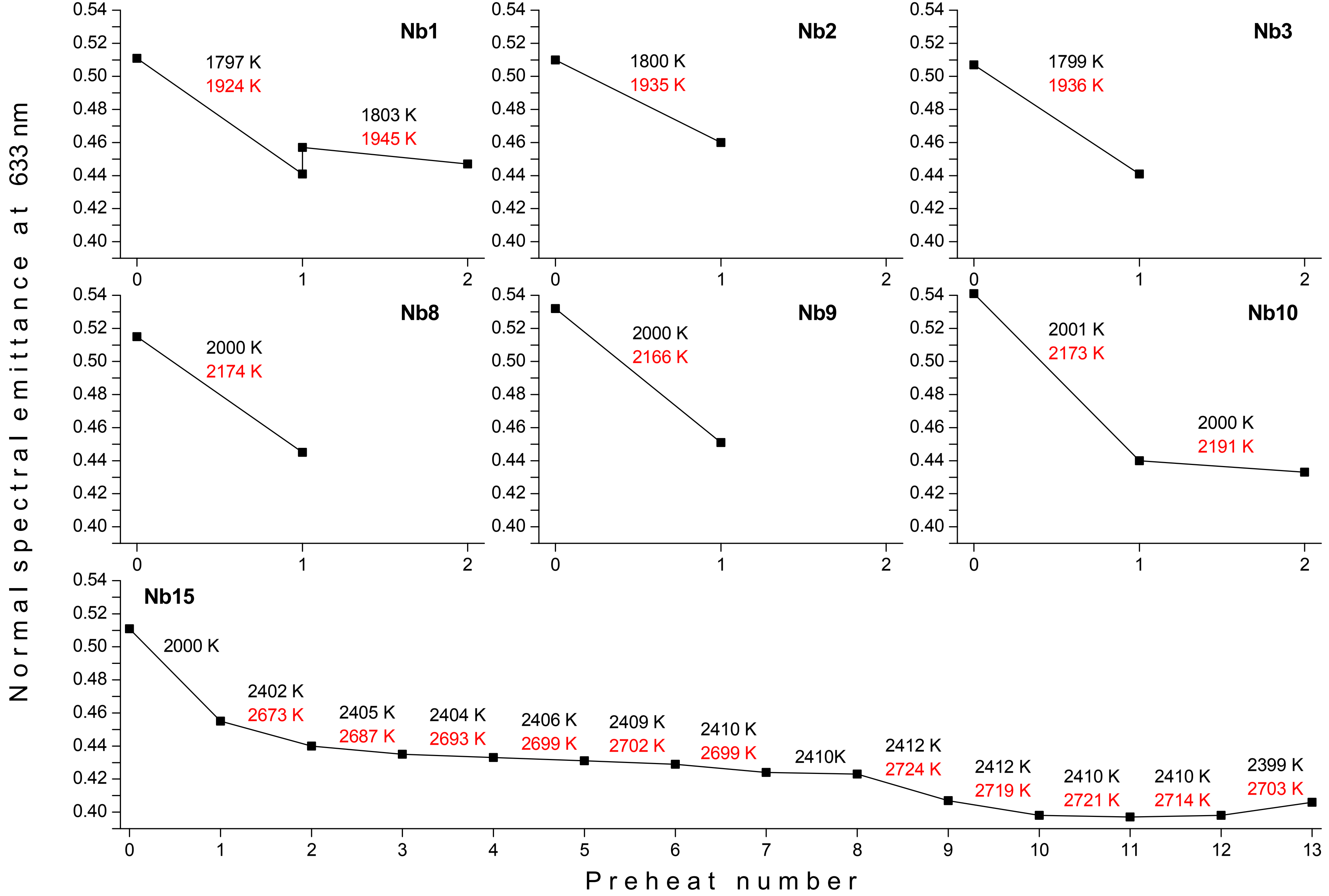

Fig. 5.6: The effect of pre-heating on the room-temperature normal spectral emittance. Temperatures in black (red) denote the maximum radiance (thermodynamic) temperature of the preheats. In the case of specimen Nb1, the second preheat was done two days after the first one.

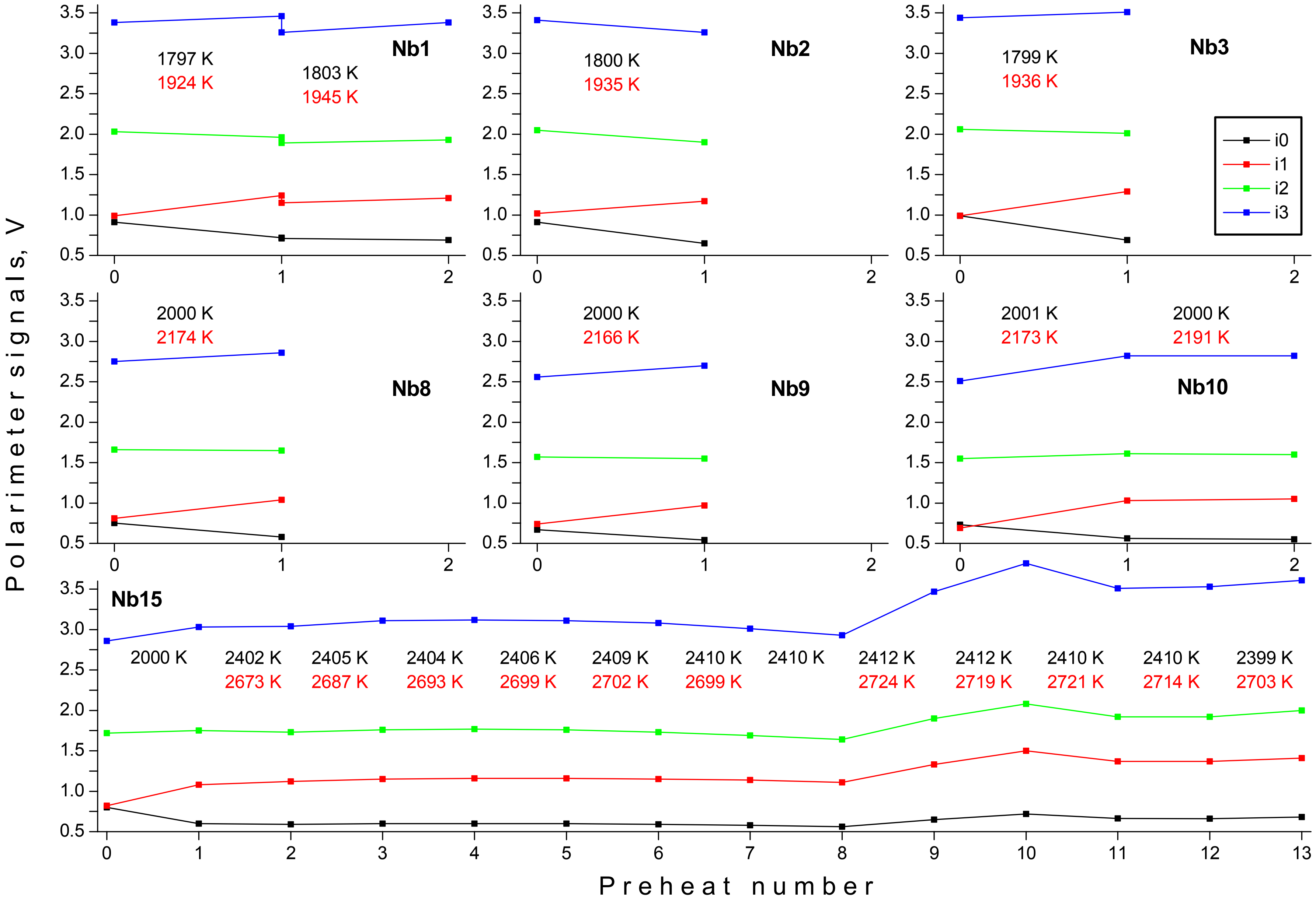

Fig. 5.7: The effect of pre-heating on the room-temperature millisecond-polarimeter signals. Temperatures in black (red) denote the maximum radiance (thermodynamic) temperature of the preheats. In the case of specimen Nb1, the second preheat was done two days after the first one.

5.2 Measurements on titanium

As reported by the manufacturer, the titanium material was 99.9% pure, with the following major impurities: O, 700 ppm; Fe, 300 ppm; C, 100 ppm; N, 40 ppm; H, 35 ppm.

All specimens were treated with abrasives prior to the experiments, as described in the previous section for niobium. Attempts to pre-heat resulted in discolored specimens that had to be discarded. The reason was probably the high affinity of titanium for oxygen and nitrogen[1], combined with residual atmospheric gases inside the experiment chamber.

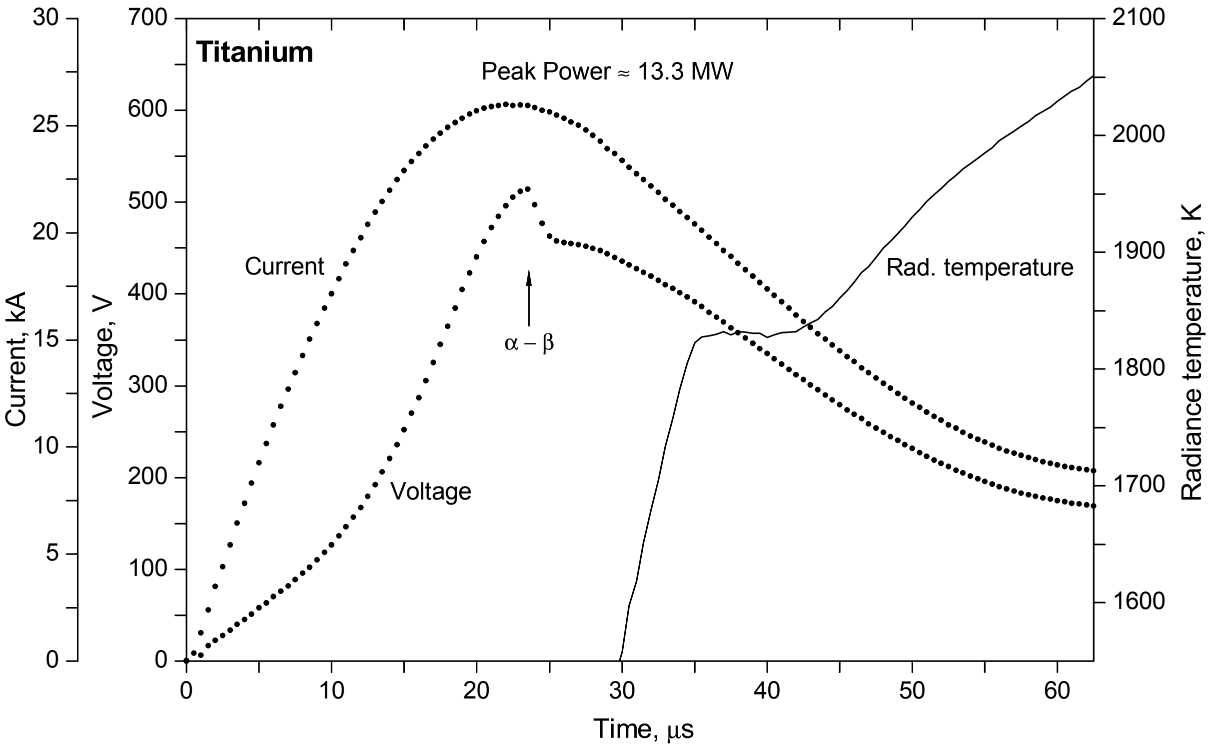

Fig. 5.8: Current, voltage, and radiance temperature at 656.3 nm, as functions of time, during a pulse-heating experiment with titanium.

Because of the significantly higher resistivity of titanium as compared to niobium, it was much easier to pulse-heat, and required a lower capacitor voltage. In a typical experiment, the capacitor bank was charged to 4.3 kV and discharged in the crowbar-mode of operation (§3.4). Figure (5.8) shows the time variation of current, voltage, and radiance temperature at 656.3 nm, during an experiment with titanium. The peak current through the specimen was about 26 kA and the peak voltage across its effective length was approximately 510 V. The

---

[1] This property of titanium is useful in its application as a deoxidizer and denitrogenizer in metallurgy, and as a getter pump inside vacuum tubes.

peak electrical power imparted on the specimen exceeded 13 MW. The melting point was reached in about 35 µs. After 63 µs, the specimen had reached a radiance temperature of approximately 2050 K, corresponding to a true temperature of about 2250 K. The heating rate in the solid phase, at about 200 K below melting, was approximately 6.5×10^{7} $K\cdot s^{-1}$. The α→β phase transformation (from hexagonal close-packed to body-centered cubic) of titanium at 1166 K [40], which is accompanied by a rapid resistance change, was visible as a sudden change in the slope of the voltage trace.

6 RESULTS

6.1 Niobium

6.1.1 Melting point

As outlined in §(4.1), the thermodynamic temperature of the specimens was computed from the measured radiance temperature and normal spectral emittance. Although radiance temperature, as such, does not bear much significance from a materials-science point of view, it plays an important role in high-temperature radiation thermometry.

As a result of a significant amount of research in the last three decades, it has been observed that, at a given wavelength (in the range of 0.5 to 1 μm), the radiance temperature of pure metals at their melting points remains constant, at least during the initial melting period[1], and that this value is highly reproducible for different specimens of the same metal, irrespective of the initial surface condition of the specimen or the operational conditions of the experiment [41, 42, 43]. This was found to be valid over a wide range of heating rates, 300 to 20000 $K\cdot s^{-1}$, corresponding to a range in heating durations (from room temperature to the melting point) of 0.04 to 1.2 s. Since radiance temperature is a surface property, it may be concluded that, at these heating rates, the surface topography of the specimen becomes uniform upon melting. Furthermore, it is reasonable to assume that the same holds for slower experiments, as well.

The present work, however, involved heating rates that were higher by a factor of at least 2.5×10^4. Therefore, the possibility of a different melting behavior could not be excluded. Figure (6.1) shows the radiance temperature at the melting transition of niobium, as measured with (i) specimens that were pulse-heated without any prior treatment, (ii) specimens that had been pre-heated to 1750 K in radiance temperature (at nominally 650 nm), and (iii) specimens that had been pre-heated to higher temperatures. The mean melting radiance temperature was highest for the 'as received' specimens and lowest for those preheated to the higher temperatures. A modified one-sided t-test applied to the measured data [44], confirmed that the mean value of melting temperatures in the first specimen group (2430.9 K) exceeded that

---

[1] In slower millisecond-resolution experiments the specimen collapses before melting is completed, except in microgravity or in levitation experiments.

of the second group (2425.3 K) at a statistical significance level of approximately 99%. Similarly, the mean melting temperature of the second group exceeded that of the third group (2416.0 K) with the same level of confidence. Although this by no means represents a systematic study, it certainly points to an interesting trend.

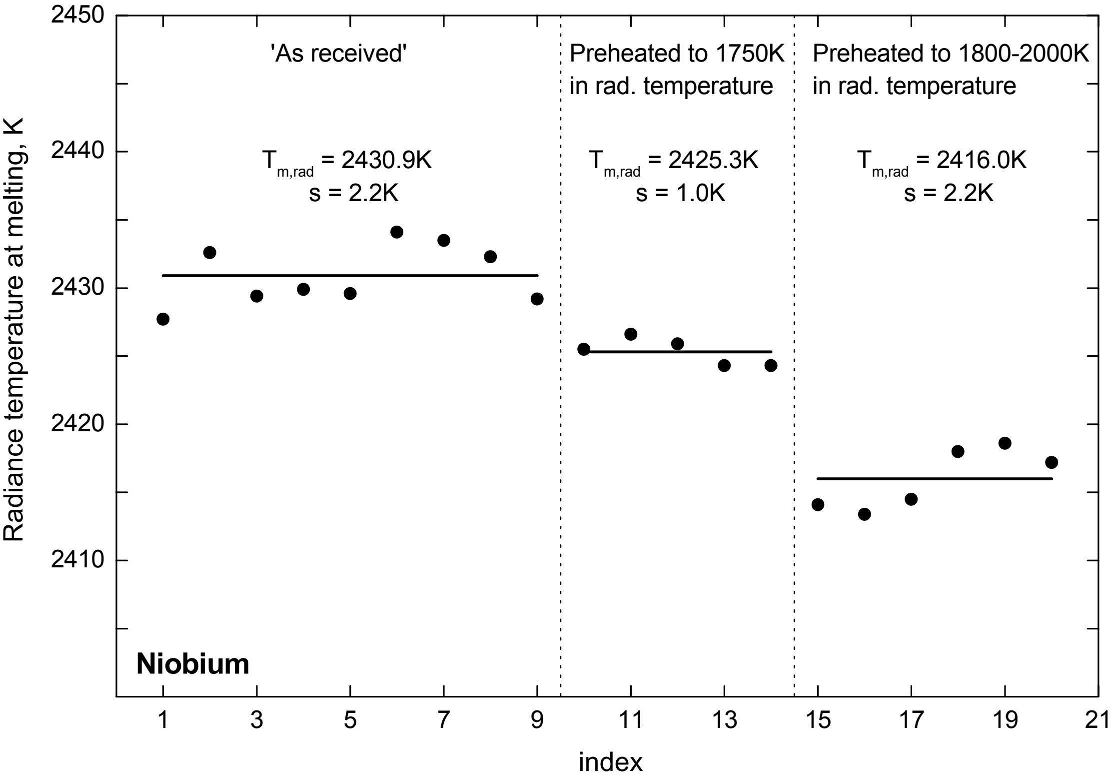

Fig. 6.1: Effect of pre-heating on the melting point radiance temperature at 656.3 nm. The sample means and standard deviations are shown for the three groups of specimens.

As mentioned above, radiance temperature is a surface property. At the melting point, the highest value it can assume is that of the thermodynamic melting temperature, as is the case with specimens incorporating a blackbody cavity (emittance≈1). With a perfectly planar surface, the radiance temperature will be a minimum, determined by the optical properties (n, k) of the specimen material. In all other cases, the radiance temperature at the melting point will lie in-between the two extremes.

When the specimen surface melts, it becomes very smooth because of the surface tension of the liquid. This might explain, why in the slower millisecond-resolution pulse-heating experiments, the radiance temperature at the melting transition of pure metals is very reproducible, irrespective of the initial surface condition of the solid specimen. At higher heating rates, however, the characteristic time of the surface smoothening may be too long compared to the duration of the melting plateau, so that some residual roughness is still present during melting, affecting the measured radiance temperature. In other words, at high heating rates it is conceivable that the melting-point radiance temperature is, to some degree, a function of the initial surface roughness of the specimen.

Along these lines, fig. (6.1) suggests that pre-heating a specimen changes its surface in a way that it behaves closer to ideal (perfectly smooth surface) at melting. This is another manifestation of the 'cleaning' effect that was always observed in the emittance-vs.-time trace of the first pre-heating pulse, as described in §(5.1). Pre-heating to higher (than 2000 K) temperatures or multiple pre-heating pulses did not further decrease the melting-point radiance temperature.

According to everything mentioned so far, the radiance temperature at the melting point of the third specimen group of fig. (6.1) should be closest to that measured in millisecond-resolution experiments (2422 K at 653 nm [39]). The fact that it is even lower (2416 K), may be explained, at least in part, by the 'size-of-source' effect [8, 45]. In short, we talk about a 'size-of-source' effect, when radiation from outside the specified target area[1] can enter the field-defining aperture and reach the detector, because of lens aberrations, internal reflections inside the radiometer, and scattering[2] in the lenses of the radiometer or the window of the chamber. The radiometer output then becomes dependent on the size of the hot object being viewed. This effect is cancelled if the measurement conditions are identical to the calibration conditions. In our case, the radiometer was calibrated on the 3 mm - wide tungsten strip of the reference lamp (§3.7.2), but the objects viewed during measurement were wires of 1.6 mm nominal diameter. If the total area on the tungsten strip from which the detector received radiation during calibration, extended in width[3] beyond the edges of the wire during measurement, then viewing a wire at the same radiance temperature as the strip would yield an apparently lower radiance temperature[4] for the wire. In order for the difference to be 6 K at 2422 K, the radiometer would have to receive approximately 2.3% of the total radiant flux

---

[1] In our case, 0.5 mm × 9.8 mm (§3.7.1).

[2] Dust on the outer surface of the objective lens is a commonly encountered source of scattering.

[3] In both cases, calibration and measurement, the objects viewed by the radiometer extended in height much beyond the nominal target height of 9.8 mm, so that any size-of-source effect in that direction was probably cancelled. This, of course, is based on the assumption that there is no temperature gradient along the portion of the tungsten filament viewed by the radiometer during calibration, as there is none along the pulse-heated wire.

[4] The impact of radiation reflected off the experiment chamber wall into the radiometer is neglected here.

that it received during calibration from the area on the tungsten strip to the left and right of the central portion of 1.6 mm in width[1].

The difference, in terms of radiance temperature at the melting point, between the first and third specimen groups of fig. (6.1), corresponds to a difference in normal spectral emittance of close to 6%. Unfortunately, the between-experiments variation of the measured emittance at the melting point was of the same order of magnitude[2], so that this difference could not be resolved. In other words, the systematic decrease in the melting-point normal spectral emittance, caused by pre-heating the specimens, was obscured by the random error of the polarimetric measurement.

At this point, it should again be stressed that the determination of normal spectral emittance by laser polarimetry requires specimen surfaces that are as close as possible to the ideal case of an optically smooth surface. The measurements on titanium (§6.2.1) suggest that the polarimeter does measure a higher normal spectral emittance on rougher surfaces. It is not clear yet, where the limits, in terms of roughness, are, within which the results can be trusted. In any case, it appears that the degree of surface roughness encountered in this work, did not have too much of a deteriorating effect on the measurement, other than perhaps reducing the polarimeter signal levels. These problems are of course much reduced in the liquid phase, when the specimen surface becomes very smooth.

The mean value of the thermodynamic temperature at the melting transition of niobium was 2736 K, compared to the accepted value (on ITS-90) of 2749 K [46]. The normal spectral emittance exhibited a rapid decrease at melting, and remained constant in the liquid phase, up to 3200 K. Its mean value in the liquid phase was 0.36 at 677 nm, somewhat higher than the value at melting of 0.339 at 653 nm, which is computed from the melting point of 2749 K and the melting-point radiance temperature (at 653 nm) of 2422 K [39].

Figure (6.2) shows the radiance temperature, thermodynamic temperature, and normal spectral emittance of a niobium specimen, as functions of time during a pulse-heating

---

[1] This estimate was computed using Wien's approximation to Planck's law (§2.1.8). Furthermore, some simplifying assumptions were made, notably that both the strip of the reference lamp and the wire-shaped specimen can be treated as iso-radiance emitters (lambertian and uniform). In the case of a wire, this also means neglecting the curvature of its surface.

[2] This rather large variation, is mainly caused by differences in the initial alignment of the PSD and/or specimen movement.

experiment. For a given specimen, the plateau temperature (radiance or thermodynamic) was determined by averaging the measured temperatures along the plateau. The standard deviation of an individual temperature from the plateau average was in the range of 0.1 to 2.7 K, for the radiance temperature plateaus, and of 11 to 29 K, for the thermodynamic temperature plateaus. The trend of radiance and thermodynamic temperature along each plateau was determined by (least-squares) fitting a linear function of time to the measured temperatures. The slope of the radiance temperature plateaus was in the range of 0.038 to 0.664 K·μs^{-1}, and that of the thermodynamic temperature plateaus in the range of -0.765 to 3.3 K·μs^{-1}.

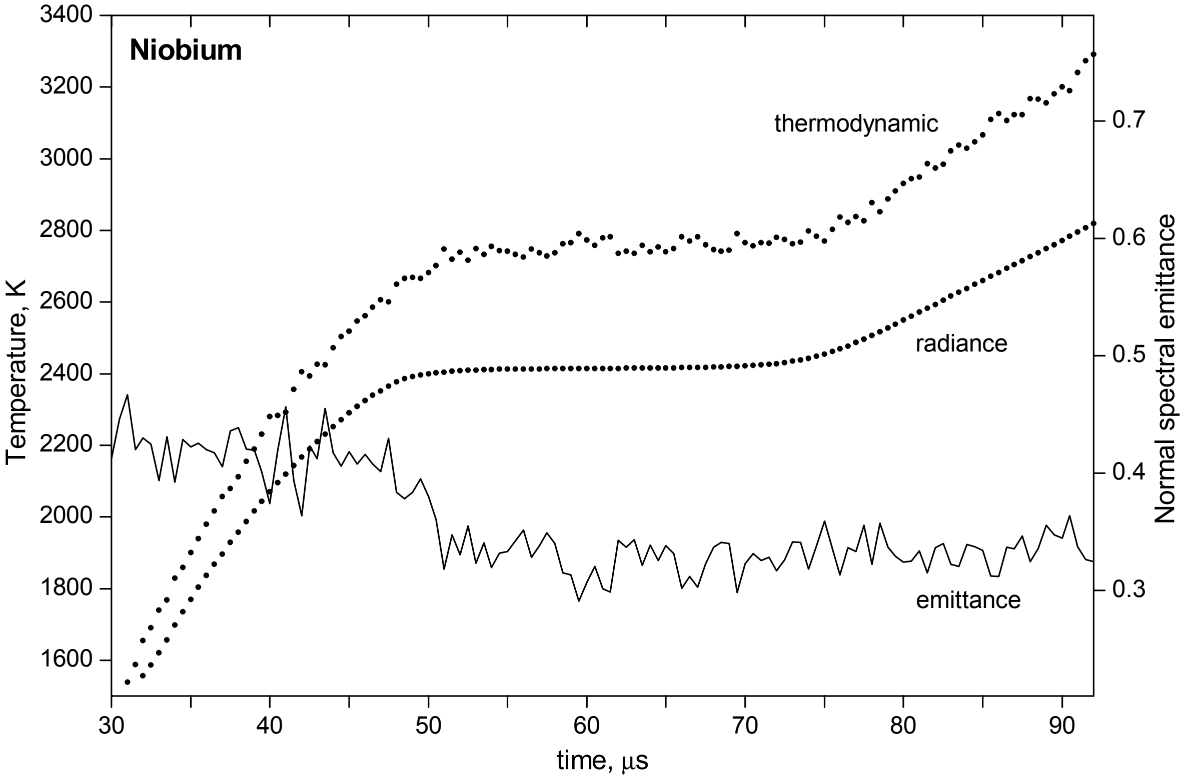

Fig. 6.2: Radiance temperature (at 656.3 nm), thermodynamic temperature, and normal spectral emittance (at 677 nm), as functions of time, during a niobium pulse-heating experiment.

The variation of the four polarimeter signals with time during a niobium pulse-heating experiment is shown in fig. (6.3). During melting and in the liquid, three out four signals increased significantly. The decrease in the signals at the experiment end is probably caused by specimen movement. Also shown, as a function of time, is the degree of polarization of the reflected laser beam, computed from the measured Stokes parameters. A significant deviation from one would have indicated some problem and questioned the use of eq. (3.38) (see the discussion in §3.8.2.4).

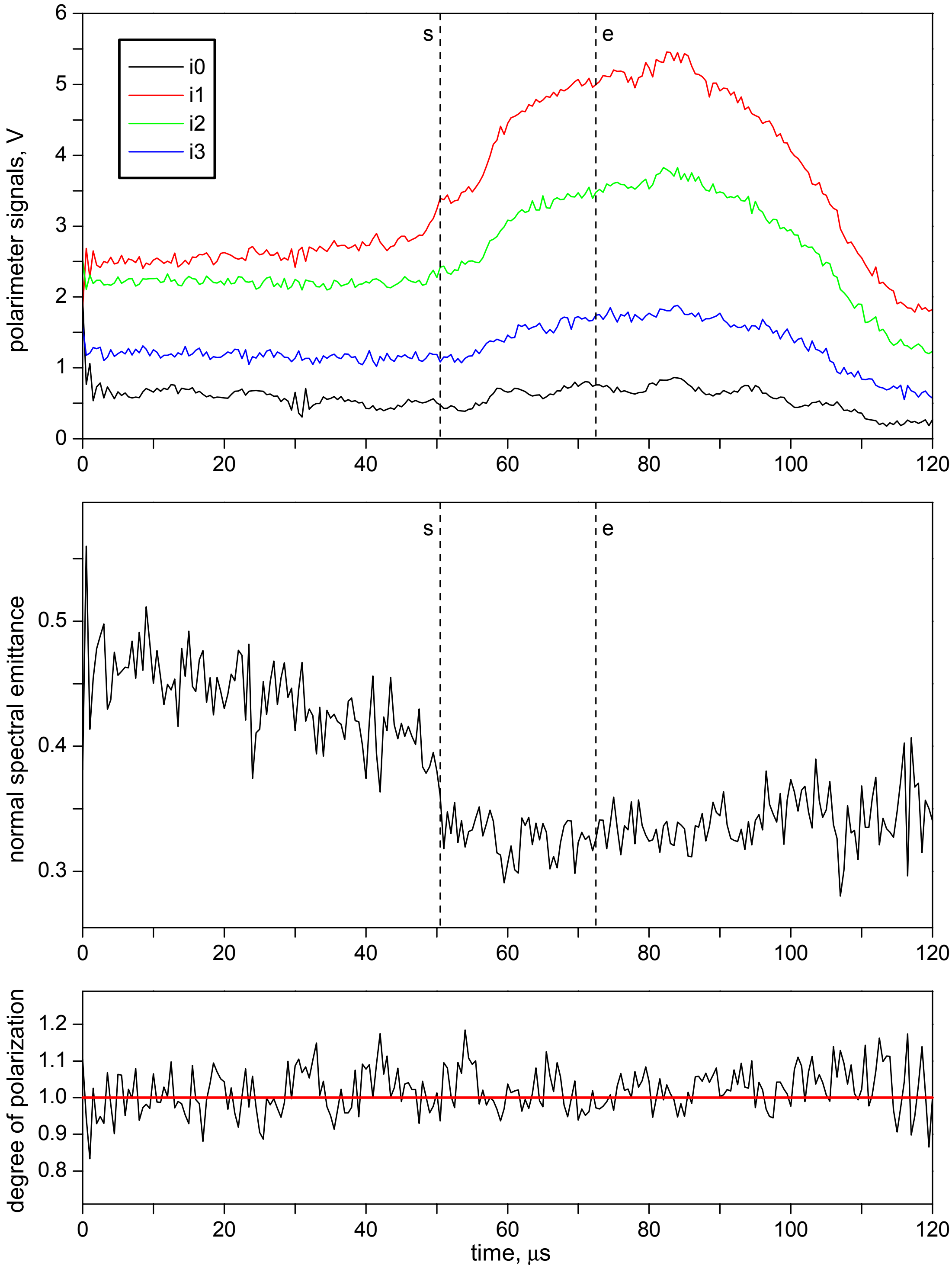

Fig. 6.3: The four polarimeter signals, the normal spectral emittance of the specimen, and the degree of polarization of the reflected laser beam, as functions of time, during a niobium pulse-heating experiment. s and e indicate the start and end of melting, respectively.

6.1.2 Electrical resistivity

The linear functions representing the measured resistivity ρ_{el} (not corrected for thermal expansion) of solid and liquid niobium, in the ranges of 1600 to 2700 K and 2800 to 3200 K respectively, were

solid: $$\rho_{el} = 60.8 + 2.42\times10^{-2}(T-1600) \tag{6.1}$$

liquid $$\rho_{el} = 98.7 + 3.95\times10^{-3}(T-2800) \tag{6.2}$$

ρ_{el} is expressed in μΩ·cm and the temperature T in K. The resistivity at the beginning and at the end of melting was 87.5 μΩ·cm and 98.5 μΩ·cm, respectively.

Using data from literature, the measured electrical resistivity was corrected for thermal expansion. Specifically, the linear thermal expansion of solid niobium as a function of temperature in the range of 1500 to 2700 K that is reported in [47], was used:

solid: $$\frac{l-l_0}{l_0} = 5.4424\times10^{-3} - 8.8553\times10^{-6}\,T + 1.2993\times10^{-8}\,T^2 - 4.4002\times10^{-12}\,T^3 + 6.3476\times10^{-16}\,T^4 \tag{6.3}$$

Since niobium is of body-centered cubic structure, the linear thermal expansion can be converted to a purely radial volume expansion using:

$$\frac{V}{V_0} = \left(\frac{r}{r_0}\right)^2 = \left(1 + \frac{l-l_0}{l_0}\right)^3 \tag{6.4}$$

where V denotes volume, and V_0 is the volume of the 'effective' specimen at room temperature.

For liquid niobium, expansion data from [19] were used:

liquid: $$\frac{V}{V_0} = 0.9627 - 2.5\times10^{-5}\,T + 3.14\times10^{-8}\,T^2 - 1.17\times10^{-12}\,T^3 \tag{6.5}$$

By combining eqs. (6.4) and (6.5) with eqs. (6.1) and (6.2), the following functions of temperature were obtained for the corrected electrical resistivity of niobium, in the same temperature ranges as above:

solid: $$\rho_{el,c} = 62.8 + 2.64\times10^{-2}(T-1600) + 1.44\times10^{-6}(T-1600)^2 \tag{6.6}$$

liquid: $$\rho_{el,c} = 110 + 1.76\times10^{-2}(T-2800) \tag{6.7}$$

Again, $\rho_{el,c}$ is expressed in μΩ·cm and the temperature T in K. Extrapolation of these functions to the measured melting temperature of 2736 K, yields 94.7 μΩ·cm and

108.9 μΩ·cm for the resistivity of niobium at the beginning and at the end of melting, respectively. The ratio of these two values (liquid/solid) did not change significantly by the correction for thermal expansion.

Figure (6.4) summarizes these results and compares them to data obtained at NIST in the past, using the millisecond-resolution [48] and microsecond-resolution pulse-heating facilities [49]. Thermodynamic temperature in [49] was computed from radiance temperature using the known melting temperature of niobium, under the assumption of constant emittance in the liquid. Since it was found that the normal spectral emittance of liquid niobium is indeed constant, the older liquid phase resistivity data agree well with that obtained in the present work.

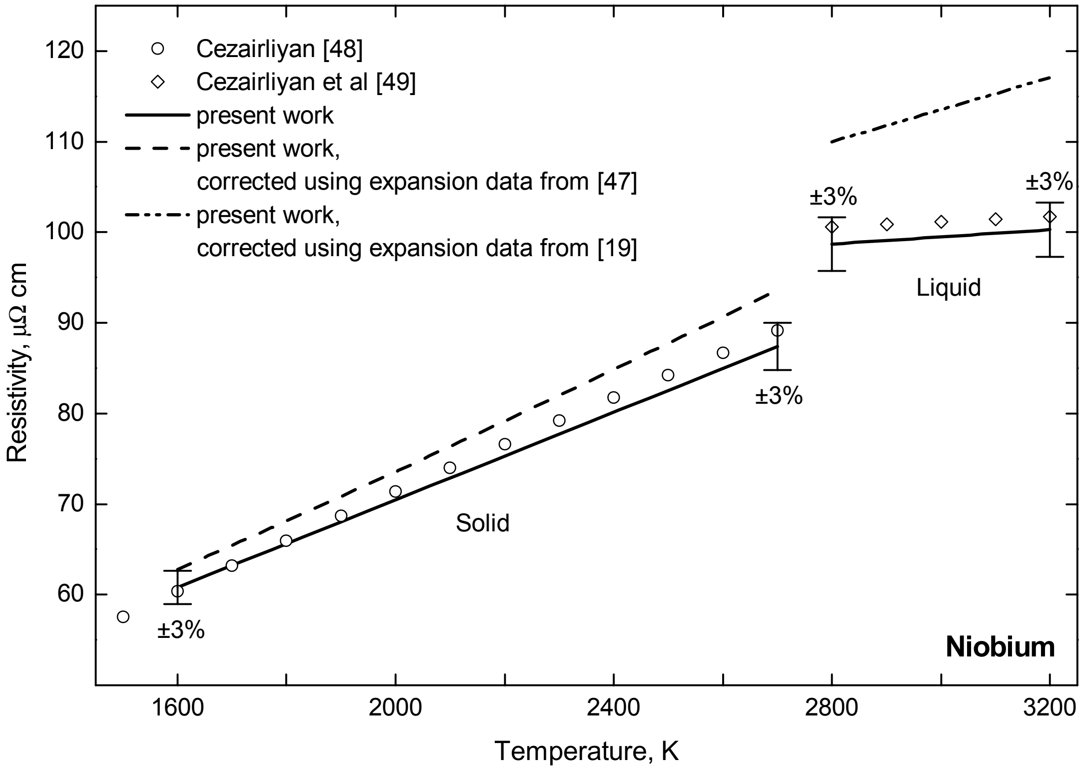

Fig. 6.4: Electrical resistivity of niobium as a function of temperature.

6.1.3 Heat of fusion

The mean value of the heat of fusion from all experiments was 32.0 kJ·mol^{-1}. The standard deviation from the mean was 1.5 kJ·mol^{-1}. This value for the heat of fusion agrees reasonably well with results obtained at NIST in the past. In [50] a value of 31.5 kJ·mol^{-1} is reported. It was measured with the slower millisecond-resolution system using the 'sandwich' technique[1] to prevent the specimen from collapsing during melting. In [51] a value of 31.1 kJ·mol^{-1} is reported. This was measured using the microsecond system. Since there were no means to obtain true temperature at that time, the heat of fusion in [51] was computed from least-squares fits to the radiance-temperature-vs.-absorbed-energy data.

6.1.4 Specific heat capacity

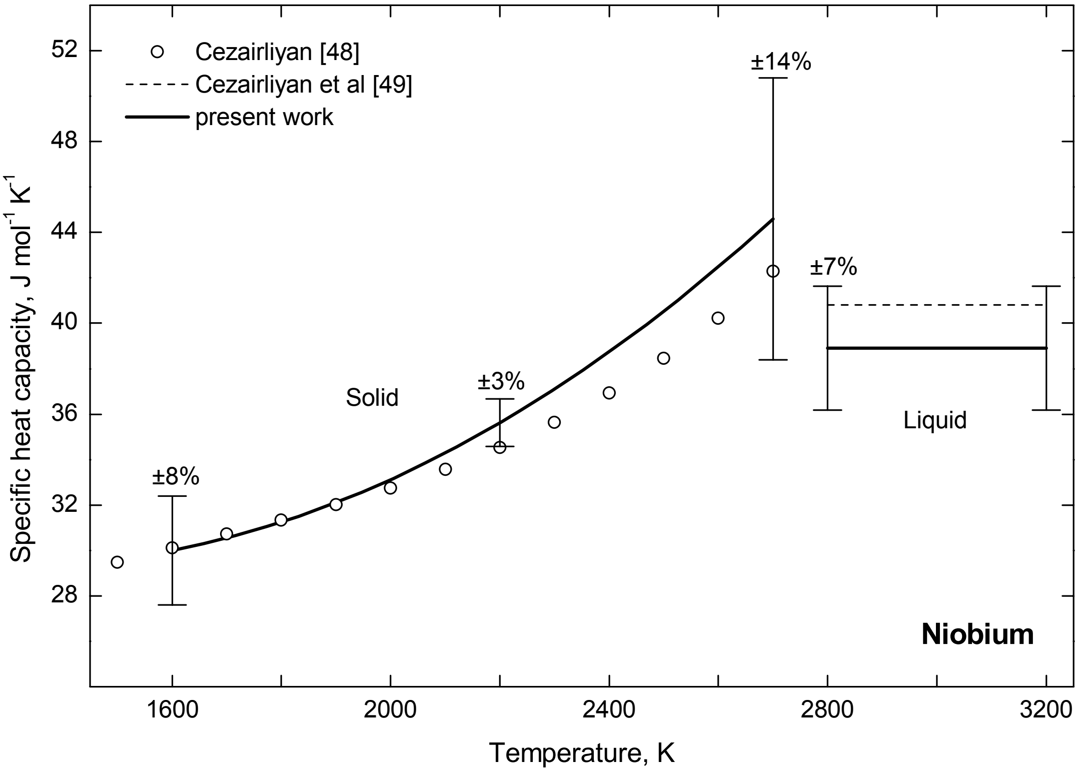

Fig. 6.5: Specific heat capacity of niobium as a function of temperature.

The quadratic function representing the specific heat capacity of solid niobium, in the range of 1600 to 2700 K, was:

solid: $$c_p = 30.0 + 4.7\times10^{-3}(T-1600) + 7.8\times10^{-6}(T-1600)^2 \quad (6.8)$$

c_p is expressed in J·mol^{-1}·K^{-1} and T in K.

In the liquid phase, up to 3200 K, the specific enthalpy increased linearly with temperature From the slope of the linear function that was fitted to the specific enthalpy vs. temperature

---

[1] This means that a strip of the metal under study (niobium in this case) was 'sandwiched' between two strips of another metal with a higher melting temperature. The two outer strips provided support for the inner strip when it melted.

data, a value of 38.9 J·mol^{-1}·K^{-1} was obtained for the specific heat capacity of liquid niobium.

The solid and liquid heat capacity of niobium is shown in fig. (6.5) as a function of temperature. The results of the present work agree, within their uncertainty, with data obtained at NIST in the past, which, for ease of reference, are also shown in the same figure.

6.1.5 Thermal conductivity

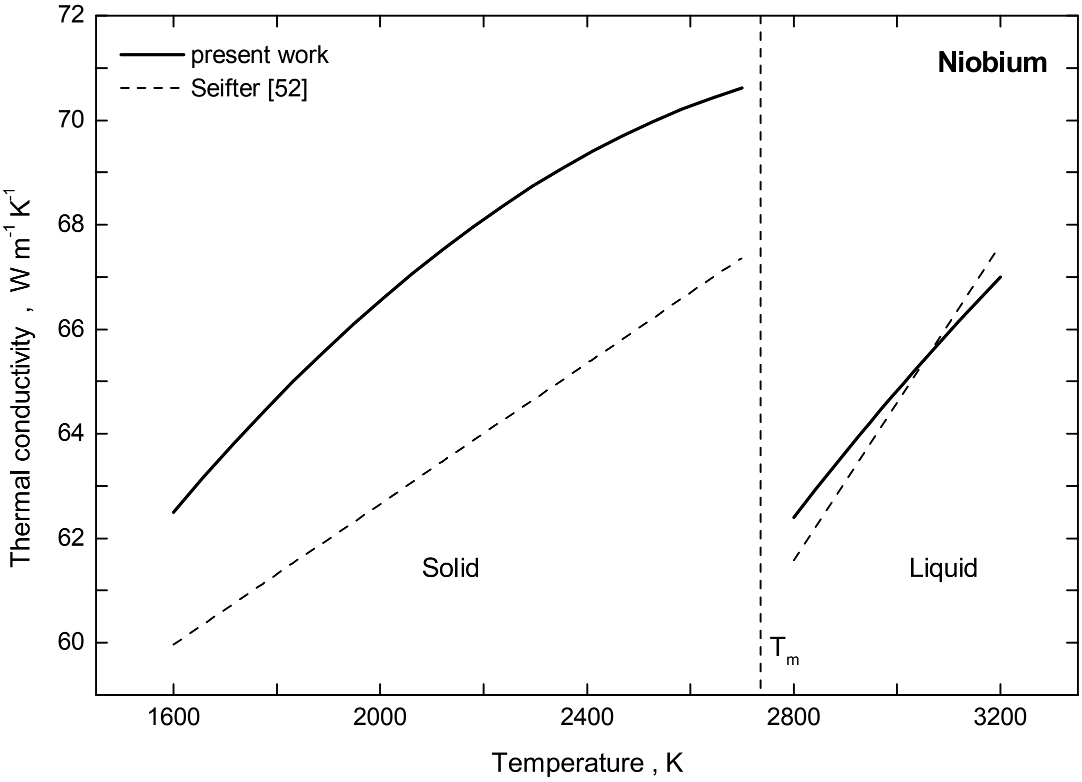

Fig. 6.6: Thermal conductivity of solid and liquid niobium as a function of temperature, estimated from the corrected electrical resistivity data, using $L_0 = 2.45\times10^{-8}$ W·Ω·K^{-2}. T_m is the melting point of niobium, as measured in the present work.

From the corrected resistivity data, eqs. (6.6) and (6.7), the thermal conductivity of solid and liquid niobium could be estimated, using eq. (4.7), in the ranges 1600 to 2700 K (solid) and 2800 to 3200 K:

solid: $$\lambda = 62.5 + 1.17\times10^{-2}(T-1600) - 3.93\times10^{-6}(T-1600)^2 \qquad (6.9)$$

liquid $$\lambda = 62.4 + 1.28\times10^{-2}(T-2800) - 3.28\times10^{-6}(T-2800)^2 \qquad (6.10)$$

λ is expressed in W·m^{-1}·K^{-1} and the temperature T in K. A value of 2.45×10^{-8} W·Ω·K^{-2} was used for the Lorenz number L_0. Equations (6.9) and (6.10) are plotted in fig. (6.6), together with estimates for the thermal conductivity of niobium reported in [52].

6.1.6 Thermal diffusivity

The thermal diffusivity of solid and liquid niobium, in the temperature ranges 1600 to 2700 K (solid) and 2800 to 3200 K (liquid), was estimated from the measured resistivity (not corrected for thermal expansion) and specific heat capacity, using eq. (4.8):

$$\text{solid:} \quad \alpha = 0.233 + 1.64\times10^{-5}(T-1600) - 8.64\times10^{-8}(T-1600)^2 + 2.82\times10^{-11}(T-1600)^3 \tag{6.11}$$

$$\text{liquid:} \quad \alpha = 0.194 + 6.05\times10^{-5}(T-2800) \tag{6.12}$$

α is expressed in $cm^2 \cdot s^{-1}$ and T in K. A value of 2.45×10^{-8} $W \cdot \Omega \cdot K^{-2}$ was used for the Lorenz number L_0.

Equations (6.11) and (6.12) are plotted in fig. (6.7).

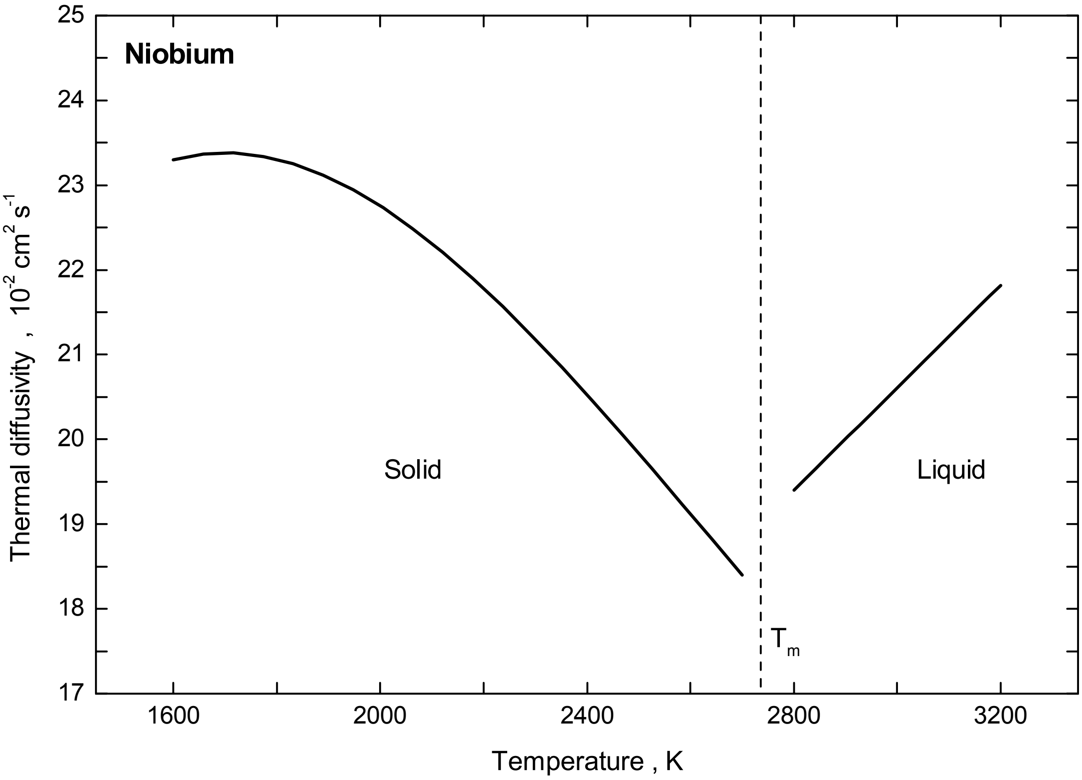

Fig. 6.7: Thermal diffusivity of solid and liquid niobium as a function of temperature, computed from the estimated thermal conductivity data (fig. 6.6). T_m is the melting point of niobium, as measured in the present work.

6.2 Titanium

6.2.1 Melting point

The mean value of the measured radiance temperatures (at 656.3 nm) at the melting transition of the titanium specimens was 1835 K. This is considerably higher than the accepted value of 1800 K (at 653 nm), determined using a (slower) millisecond-resolution pulse-heating technique [53]. The difference may be explained by the much higher heating rates involved in the present work. The standard deviation of the melting-point radiance temperatures of the individual specimens from the overall mean[1], was 10 K, which is rather large. It should be remembered that the titanium specimens could not be pre-heated in the slower millisecond-system, prior to pulse-heating in the microsecond-system (§5.2). Their treatment with abrasives to remove any oxides, probably produced surfaces with varying degrees of roughness, which, combined with the high heating rates, could be the reason for this large standard deviation.

The mean value of the computed thermodynamic temperatures at the melting transition of all specimens was 1941 K, close to the accepted value of 1945 K for the melting point of titanium [54]. The standard deviation from the mean was 6 K. The mean value of the normal spectral emittance at the melting point of titanium was 0.52. This is significantly higher than the value of 0.4 that was obtained with the slower pulse-heating technique. But it is compatible with the higher radiance temperature at the melting point, yielding a much better agreement with the slower experiments in terms of thermodynamic temperature. Whatever the reason for the higher melting-point radiance temperature, the polarimeter ‘reacted’ correctly to it. If the reason was indeed residual surface roughness at the melting point, then it is not clear at this point why the polarimeter measured the correct emittance (within the measurement uncertainty), considering that its ‘measurement equation’ (§3.8.2.4) is based on the assumption of a perfectly smooth specimen surface.

As outlined in §(6.1.1), the melting plateau temperature (radiance or thermodynamic), for a given specimen, was determined by averaging the measured temperatures (data points) along

---

[1] It is not strictly correct to compute the mean value of the radiance temperatures at the melting transition of the different specimens, since there is reason to believe that in fast pulse-heating experiments the observed differences between specimens, are, at least in part, real, and not entirely attributable to a random measurement error.

the plateau. The standard deviation of an individual temperature from the plateau average was in the range of 0.75 to 1.9 K, for the radiance temperature plateaus, and of 5.9 to 10 K for the thermodynamic temperature plateaus. The trend of radiance and thermodynamic temperature along each plateau was determined by (least-squares) fitting a linear function of time to the measured temperatures. The slope of the radiance temperature plateaus was in the range of -0.14 to 0.8 $K\cdot\mu s^{-1}$, and that of the thermodynamic temperature plateaus in the range of -1.0 to 2.3 $K\cdot\mu s^{-1}$.

Figure (6.8) shows the radiance temperature, thermodynamic temperature, and normal spectral emittance of a titanium specimen, as functions of time during a pulse-heating experiment. The normal spectral emittance gradually decreased in the solid, remained constant during melting, and further decreased in the liquid phase. The rapid drop at the onset of melting that was observed with niobium, is absent here. It is interesting to note that the emittance decreased in the liquid until it reached a value of approximately 0.4, which is the value measured with the slower pulse-heating technique at the melting point of titanium.

In the past, when no means were available to measure normal spectral emittance in such high-speed pulse-heating experiments, the measured radiance temperature was converted to thermodynamic temperature using the known melting point of the specimen (from literature), under the assumption that the emittance was constant in the liquid phase and equal to its value at the melting transition[1]. As demonstrated by niobium, this assumption was justified in some cases. In the case of titanium however, it would have introduced an error in true temperature because the normal spectral emittance decreased significantly after melting was completed. Figure (6.9) shows that this error would quickly have exceeded 50 K.

Figure (6.10) shows the four polarimeter signals, the normal spectral emittance, and the degree of polarization of the reflected laser beam, as functions of time during a titanium pulse-heating experiment. All four signals increased during melting, something that was observed with niobium, as well. The low-frequency fluctuation of the signals in the liquid phase was probably caused by specimen movement and did not affect the computed emittance, since all four signals varied ‘in step’.

---

[1] A serious limitation of this method was of course that it could not be used in the solid phase, and hence no reliable temperature measurement was possible below melting.

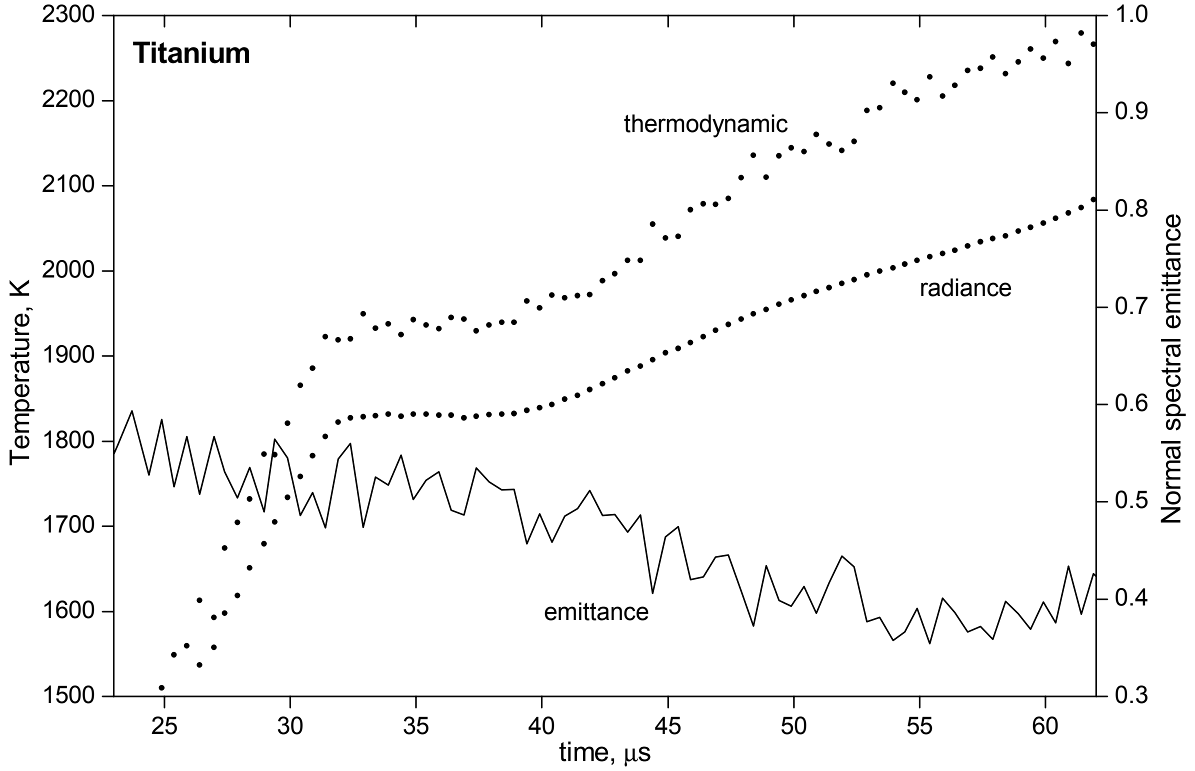

Fig. 6.8: Radiance temperature (at 656.3 nm), thermodynamic temperature, and normal spectral emittance (at 677 nm), as functions of time, during a titanium pulse-heating experiment.

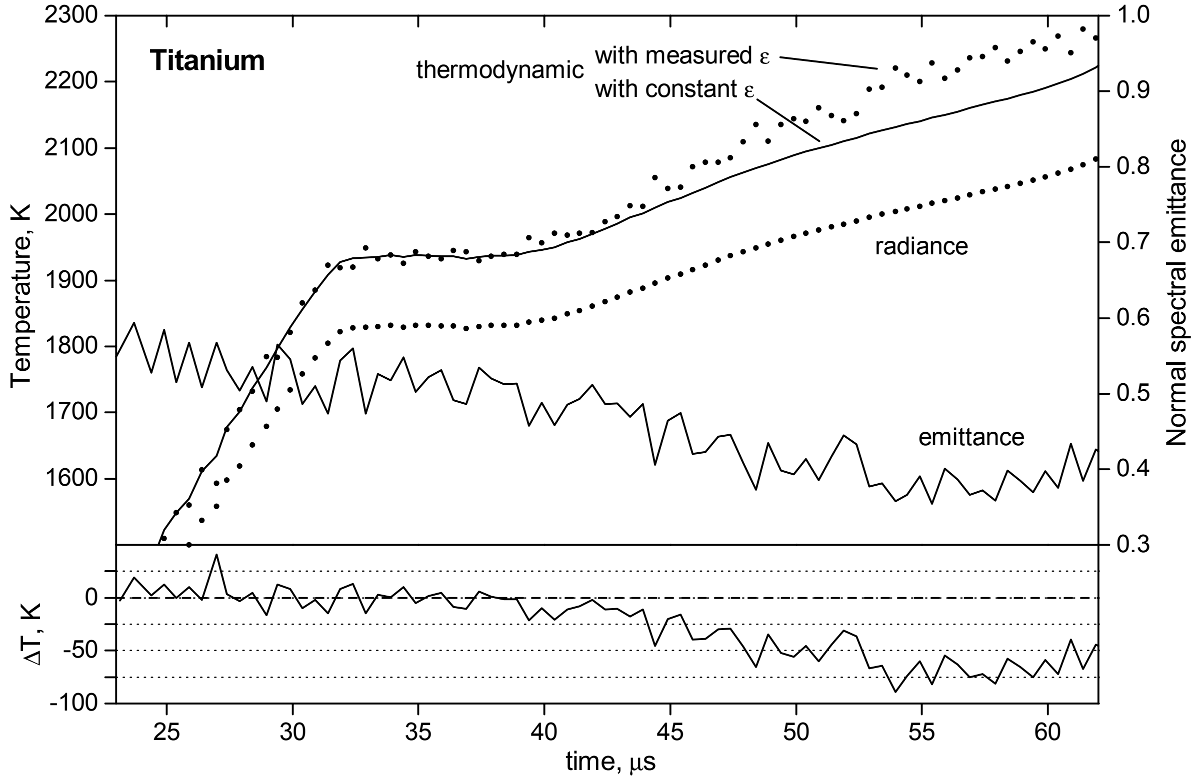

Fig. 6.9: Thermodynamic temperature computed from radiance temperature under the assumption of a constant normal spectral emittance that is equal to its value at the melting transition, is plotted in the upper graph as a solid-line temperature trace. The lower graph shows the error in true temperature introduced by this assumption.

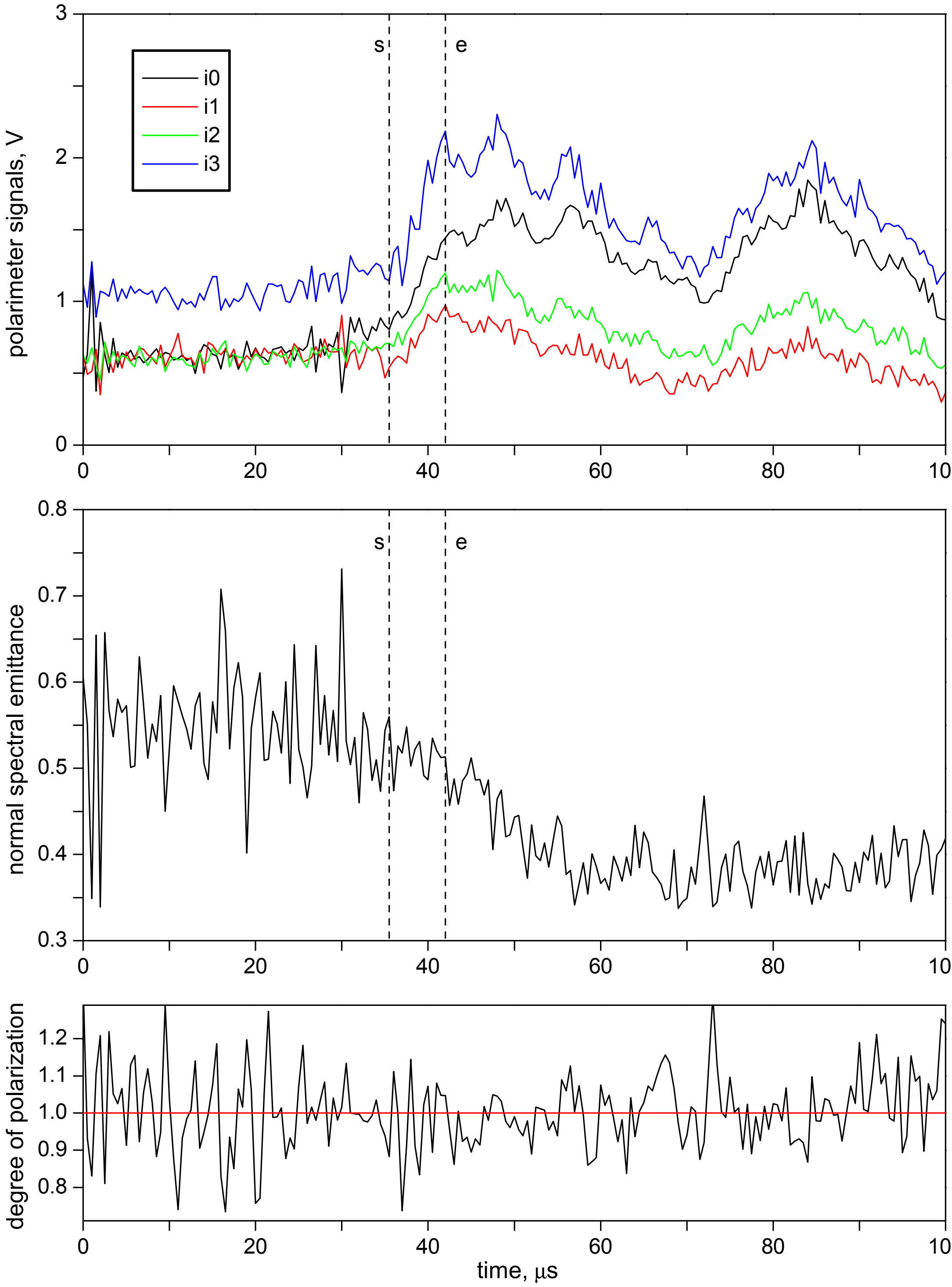

Fig. 6.10: The four polarimeter signals, the normal spectral emittance of the specimen, and the degree of polarization of the reflected laser beam, as functions of time, during a titanium pulse-heating experiment. s and e indicate the start and end of melting, respectively.

6.2.2 Electrical resistivity

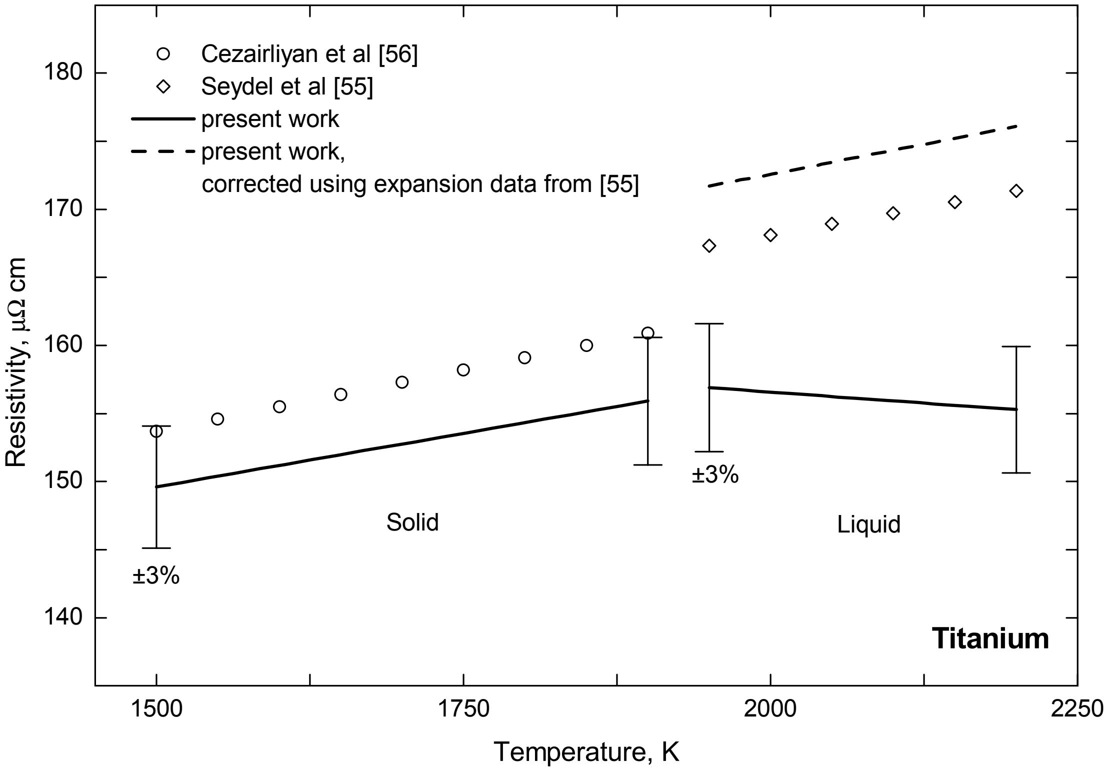

Fig. 6.11: Electrical resistivity of titanium as a function of temperature.

The linear functions representing the resistivity ρ_{el} (not corrected for thermal expansion) of solid and liquid titanium, in the ranges of 1500 to 1900 K and 1950 to 2200 K respectively, were:

solid $$\rho_{el} = 149.6 + 1.57 \times 10^{-2} (T - 1500) \tag{6.13}$$

liquid $$\rho_{el} = 156.9 - 6.48 \times 10^{-3} (T - 1950) \tag{6.14}$$

ρ_{el} is expressed in μΩ·cm and the temperature T in K. The resistivity at the beginning and at the end of melting was 156.5 μΩ·cm and 157 μΩ·cm, respectively.

In the liquid, the measured resistivity was corrected for thermal expansion using volume-expansion data from [55]:

liquid: $$\frac{V}{V_0} = 1.093 + 1.575 \times 10^{-4} (T - T_m) + 5.671 \times 10^{-9} (T - T_m)^2 \tag{6.15}$$

where T_m denotes the melting temperature. By substituting 1941 K for T_m, the following function of temperature was obtained for the corrected electrical resistivity of liquid titanium, in the range 1950 to 2200 K:

liquid: $$\rho_{el,c} = 171.7 + 1.76\times10^{-2}(T-1950) \qquad (6.16)$$

Again, $\rho_{el,c}$ is expressed in μΩ·cm and the temperature T in K. Extrapolation of this function down to the melting temperature, yields 171.5 μΩ·cm for the resistivity of titanium at the end of melting.

Figure (6.11) summarizes these results. The resistivity in the solid phase (not corrected) is compared to data that was obtained at NIST in the past [56] using the millisecond-resolution pulse-heating system. The corrected resistivity of liquid titanium is compared to the data reported in [55]. Temperature in [55] was computed using the assumption of constant normal spectral emittance in the liquid phase.

6.2.3 Heat of fusion

The mean value of the heat of fusion from all experiments was 13.2 kJ·mol^{-1}. The standard deviation from the mean was 0.4 kJ·mol^{-1}. In the past, a value of 13.0 kJ·mol^{-1} had been measured at NIST using the same microsecond-resolution pulse-heating technique [57]. At that time, a different radiometer was in use, whose measurement range started above the radiance temperature of titanium at its melting point. In order to be able to detect a melting plateau, the interference filter was removed to increase the radiant flux incident on the detector. The radiometer output therefore corresponded to an integral of the emitted radiance over a wide wavelength range. Heat of fusion was computed from least-squares fits to the radiometer-output-vs.-absorbed-energy data.

6.2.4 Specific heat capacity

For the specific heat capacity of titanium in the ranges of 1500 to 1900 K (solid) and 1950 to 2200 K (liquid), constant values of 37.6 and 35.3 J·mol^{-1}·K^{-1}, were obtained. Although, it is common for liquid metals to have a constant heat capacity, a constant value in the solid phase is not realistic. The reason for not being able to resolve a positive (upward) curvature in the specific-enthalpy-vs.-temperature data, was the noise in the computed true temperature combined with the short temperature interval that was covered in the solid. Consequently, the agreement with heat capacity data of solid titanium obtained in the past at NIST, using the slower millisecond-system, is not good, particularly at the lower temperatures (fig. 6.12).

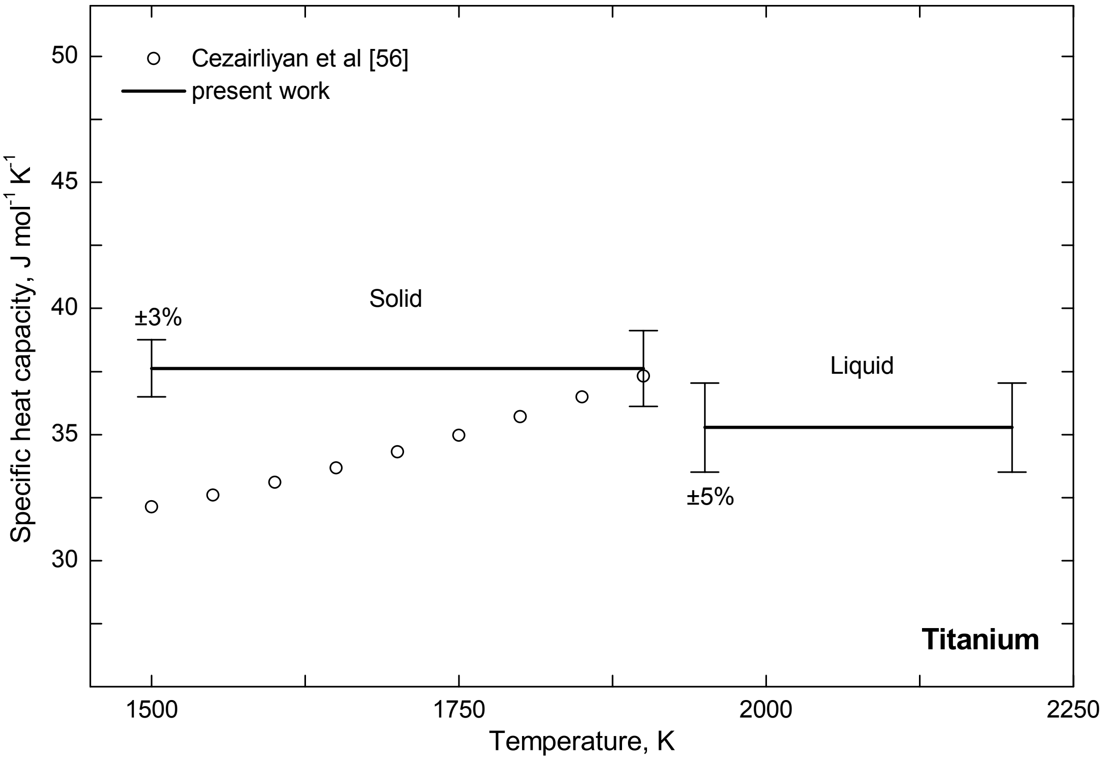

Fig. 6.12: Specific heat capacity of titanium as a function of temperature.

6.2.5 Thermal conductivity

Using the corrected resistivity data, eq. (6.16), the thermal conductivity of liquid titanium was estimated, in the range of 1950 to 2200 K:

$$\lambda = 27.83 + 1.11\times10^{-2}(T - 1950) \qquad (6.17)$$

λ is expressed in W·m^{-1}·K^{-1} and the temperature T in K. A value of 2.45×10^{-8} W·Ω·K^{-2} was used for the Lorenz number L_0. Equation (6.17) is plotted in fig. (6.13).

6.2.6 Thermal diffusivity

The thermal diffusivity of liquid titanium, in the temperature range 1950 to 2200 K, was estimated from the measured resistivity (not corrected for thermal expansion) and specific heat capacity, using eq. (4.8):

$$\alpha = 9.10\times10^{-2} + 5.094\times10^{-5}(T - 1950) \qquad (6.18)$$

α is expressed in cm^2·s^{-1} and T in K. A value of 2.45×10^{-8} W·Ω·K^{-2} was used for the Lorenz number L_0.

Equation (6.18) is plotted in fig. (6.14).

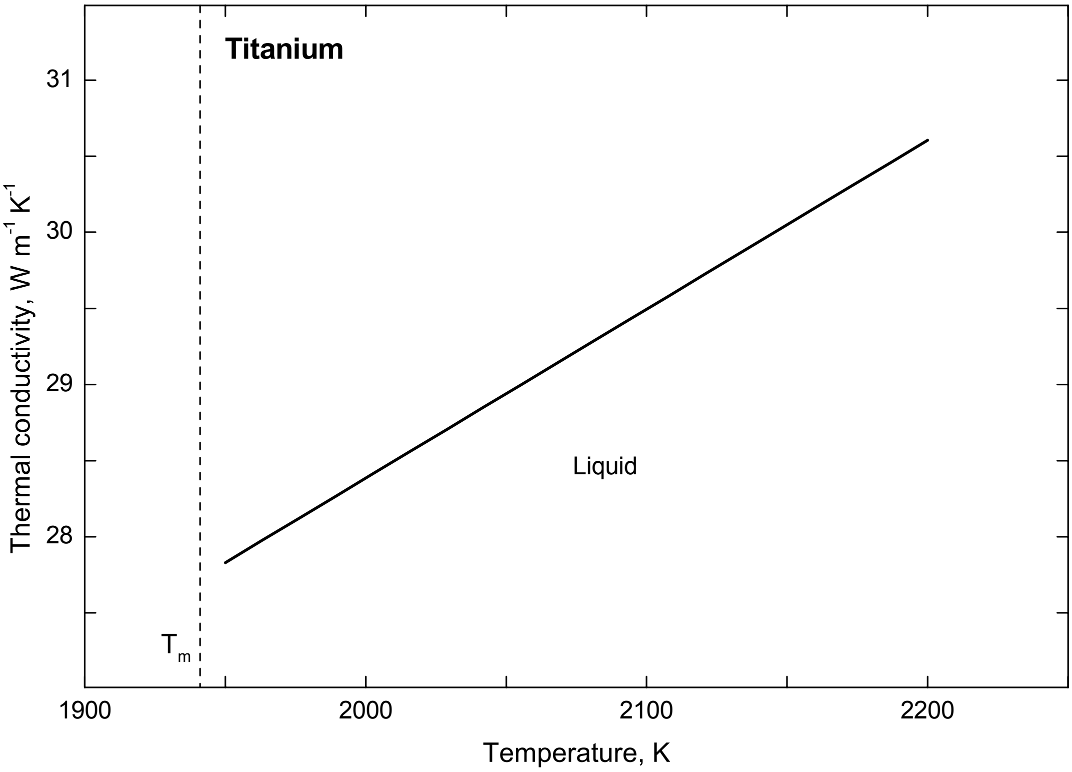

Fig. 6.13: Thermal conductivity of liquid titanium as a function of temperature, estimated from the corrected electrical resistivity data, using $L_0 = 2.45\times10^{-8}$ W·Ω·K^{-2}. T_m is the melting point of titanium, as measured in the present work.

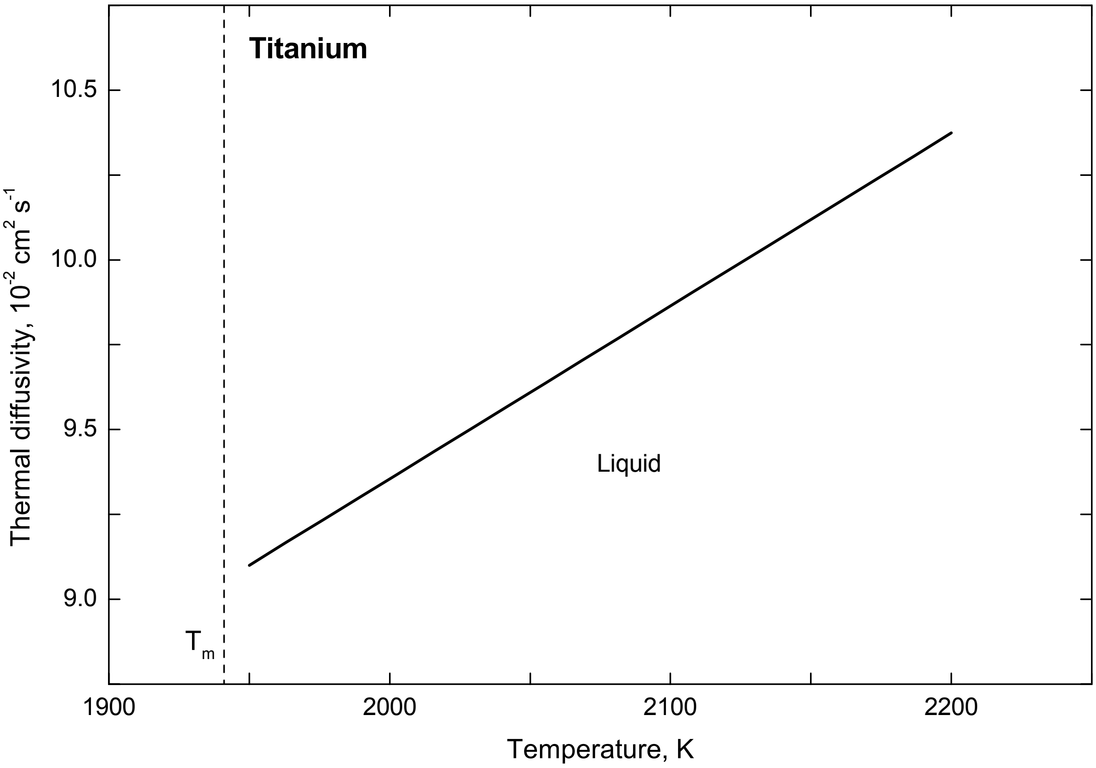

Fig. 6.14: Thermal diffusivity of liquid titanium as a function of temperature, computed from the estimated thermal conductivity data fig. (6.13). T_m is the melting point of titanium, as measured in the present work.

7 MEASUREMENT UNCERTAINTIES

In computing and reporting measurement uncertainties, an effort was made to comply, as closely as possible, with the guidelines outlined in [58] and [59]. In what is to follow, the symbol u will be used to denote standard uncertainties, which are estimated standard deviations. When an output quantity y is not measured directly but is derived from N input quantities, $x_1,\ldots,x_N$, through a functional relation, the standard uncertainty components, $u_{x_1}(y),\ldots,u_{x_N}(y)$ of the output quantity will be determined using the law of propagation of uncertainty. The symbol $u_c(y)$ will then be used to denote the combined standard uncertainty of y, computed as the square root of the sum-of-the-squares of these uncertainty components. The symbol U(y) will be used to denote the expanded uncertainty of y, which is obtained by multiplying $u_c(y)$ by a coverage factor k. In this work $k = 2$ was used, and thus expanded uncertainties represent two-standard-deviation estimates.

7.1 Radiance temperature

In order to estimate the uncertainty of the measured radiance temperature T_λ, eq. (3.11) was written in a simpler form, that was derived using the Wien approximation to Planck's law (eq. 2.16):

$$\frac{1}{T_\lambda} = \frac{1}{T_0} + \frac{n\cdot\lambda}{c_2}\ln\left(\frac{S_0}{S}\right) \qquad (7.1)$$

where T_0 denotes the calibration temperature, n the refraction index of air, λ the mean effective wavelength of the radiometer between T_0 and T_λ, S_0 the radiometer output signal during calibration (target at radiance temperature T_0), and S the signal during measurement (target at radiance temperature T_λ).

The (relative) uncertainty components of T_λ were obtained by forming the partial derivatives of $1/T_\lambda$ with respect to $1/T_0$, S_0, S, and λ:

$$u_{1/T_0}\left(\frac{1}{T_\lambda}\right) = u\left(\frac{1}{T_0}\right) \Leftrightarrow \frac{u_{T_0}(T_\lambda)}{T_\lambda} = \frac{T_\lambda}{T_0}\cdot\frac{u(T_0)}{T_0} \qquad (7.2)$$

$$u_{S_0}\left(\frac{1}{T_\lambda}\right) = \frac{n\cdot\lambda}{c_2}\cdot\frac{u(S_0)}{S_0} \Leftrightarrow \frac{u_{S_0}(T_\lambda)}{T_\lambda} = \frac{n\cdot\lambda\cdot T_\lambda}{c_2}\cdot\frac{u(S_0)}{S_0} \qquad (7.3)$$

$$u_S\left(\frac{1}{T_\lambda}\right) = \frac{n\cdot\lambda}{c_2}\cdot\frac{u(S)}{S} \Leftrightarrow \frac{u_S(T_\lambda)}{T_\lambda} = \frac{n\cdot\lambda\cdot T_\lambda}{c_2}\cdot\frac{u(S)}{S} \qquad (7.4)$$

$$u_\lambda\left(\frac{1}{T_\lambda}\right)=\frac{n}{c_2}\cdot\ln\left(\frac{S_0}{S}\right)\cdot u(\lambda) \quad\Leftrightarrow\quad \frac{u_\lambda(T_\lambda)}{T_\lambda}=\left|\frac{T_\lambda}{T_0}-1\right|\cdot\frac{u(\lambda)}{\lambda} \tag{7.5}$$

It is important to note that the first two (absolute) uncertainty components (eqs. 7.2 - 7.3) increase with temperature as T_λ^2. The third component (eq. 7.4) actually decreases with increasing temperature, because the signal S increases with temperature much faster[1] than T_λ^2. Finally, the uncertainty with which the mean effective wavelength is known gives rise to an uncertainty in T_λ that is exactly zero at the calibration temperature, and increases with $|T_\lambda\cdot(T_\lambda-T_0)|$ in both directions.

Uncertainty in the calibration temperature T_0

The calibration certificate for the tungsten-filament reference lamp that was used as the secondary standard stated that the expanded uncertainty in radiance temperature was 1.0 K at 2073.15 K (1800°C) and 1.3 K at 2373.15 K (2100°C). The expanded uncertainty due to drift, since the lamp was last calibrated by the NIST Optical Technology Division, did not exceed 1.5 K at 2073.15 K and 2.0 K at 2373.15 K. This estimate was based on the changes observed between periodic recalibrations of the lamp (its calibration history).

The current through the tungsten filament of the lamp, was computed from the voltage across a calibrated high-stability resistor, that was connected in series with the lamp. The voltage was measured using an 8½-digit multimeter. The auto-calibration feature of the digital multimeter was always used prior to performing a radiometer calibration. The expanded uncertainty of the lamp radiance temperature, stemming from the uncertainty in the measured lamp current (based on the multimeter manufacturer's specifications), was 0.6 K at 2073.15 K and 0.85 K at 2373.15 K.

Combined, these uncertainties yielded an expanded uncertainty in T_0 of 1.9 K for the calibration at 2073.15, and 2.5 K for the calibration at 2373.15 K.

No systematic correction was applied to account for the different mean effective wavelengths (by about 1 nm) of the NIST Photoelectric Pyrometer (PEP) [20], against which the reference

---

[1] The sensitivity of blackbody spectral radiance to temperature variations can be expressed as the fractional change in spectral radiance per fractional change in blackbody temperature (dL/T)/(dT/T) = Z(T). For small temperature changes the function Z(T) is approximately constant, Z(T)≈Z, and we may write $L\sim T^Z$. In the Wien approximation (accurate to better than 1% for $n\lambda T \leq 3100$ µm·K), $Z = c_2/n\lambda T$. Thus, at the lower limit of our measurement range (≈1500 K) L increases with temperature approximately as T^{15}, whereas at the highest temperatures (≈2850 K) it increases approximately as T^8. This holds for the radiometer signal S, as well, since S~L.

lamp was calibrated, and the microsecond pyrometer. Because of this difference, the radiance temperature of the reference lamp as seen by the microsecond-system pyrometer deviated somewhat from the certified radiance temperature. This probably introduced an error of about 0.4 to 0.6 K in T_0 [22].

No systematic correction was applied to account for the different field of views of the two pyrometers. Specifically, the microsecond-pyrometer accepted light from the lamp over a larger solid angle, as compared to the NIST PEP. Since the emittance of the tungsten strip varies with direction (it increases with angle from the normal), the radiance temperature of the lamp as seen by the microsecond radiometer was probably a little higher than the certified radiance temperature. The error in T_0 introduced by not applying a correction is estimated to be less than 1 K [22].

Furthermore, the NIST PEP measured the radiance emitted from a 0.8 mm × 0.6 mm rectangular area on the lamp filament, whereas the microsecond-pyrometer accepted radiance from a 9.8 mm × 0.5 mm area on the filament. Because the emittance of the tungsten filament is not uniformly constant over its entire area, and because of true-temperature gradients along the length of the filament, again, the radiance temperature of the lamp as seen by the microsecond-pyrometer differed from the certified radiance temperature. No correction was applied to account for this difference. However, in order to estimate the magnitude of the error introduced by not making a correction, the tungsten-filament was ‘scanned’ using a small-target pyrometer (circular target, 0.2 mm in diameter), with the lamp at a radiance temperature of 1973.15 K (1700°C). It was found that the lamp radiance temperature as seen by the microsecond-pyrometer was lower by about 1.2 K than that seen by the small-target (∅ 0.2 mm) pyrometer.

Uncertainty in S_0 and S

Two of the uncertainty sources in the recorded signals were the noise from the radiometer electronics and the digitization by the analog-to-digital converter. Their combined effect on the signals was determined by computing the standard deviation of individual digitized samples from the mean of a thousand samples taken when the radiometer was focused on a steady radiance source (the tungsten-filament lamp). This standard deviation was found to be independent of the signal level, which indicated that the uncertainty in radiance temperature due to noise and digitization rapidly increased with decreasing temperature.

To compensate for any drift in the radiometer amplifiers with time and room temperature, the signal was always computed as the difference between a ‘bright’ signal, with the radiometer viewing the target, and a ‘dark’ signal, with the radiometer aperture blocked. Hence, the noise and digitization errors entered the computation twice.

The (relative) expanded uncertainty in S_0, due to noise and digitization, was 0.015% for the calibration at 2073.15 K, and 0.006% for the calibration at 2373.15 K. The expanded uncertainty in S was 19 mV for the high-gain-low-temperature radiometer channel (used for the titanium measurements) and 3.2 mV for the low-gain-high-temperature radiometer channel (used for the niobium experiments).

In the case of S_0, there was an additional uncertainty caused by the combined effect of the angular alignment of the reference-lamp and the positional alignment of the radiometer on the tungsten strip during calibration. The corresponding (relative) expanded uncertainty of S_0 was 0.2%, based on the difference in S_0 after each of several realignments of the lamp and the radiometer.

In the case of the signal S, some uncertainty was introduced by the fact that the experiment chamber window during measurement was different than the window that was interposed between the reference lamp and the radiometer during calibration. In addition, the chamber window was replaced after each experiment (§3.2). Allowing for a variation (expanded uncertainty) of 1% in the transmittance of the individual windows around the transmittance of the calibration window, we obtain an expanded uncertainty of about 1 K at 1500 K radiance temperature and about 3.6 K at 2800 K radiance temperature.

No correction was applied to the measured signals to account for possible non-linearities in the radiometer amplifiers and/or the data acquisition cards.

Effective wavelength

The expanded uncertainty in the determined mean effective wavelength of the radiometer, arising from sources such as errors in the spectral transmission measurement and drift of the interference filters, was estimated at 2 nm.

As explained in §(3.7.3), no correction was applied for the variation of the mean effective wavelength with temperature. The error introduced in the measured radiance temperature was estimated to be less than 0.2 K over most of the measurement range.

Scattered light

As described in §(6.1.1), the size-of-source effect probably caused the measured radiance temperatures to be too low by a few degrees. If the difference in the melting radiance temperature of the preheated niobium specimens from that measured in the slower millisecond-system were entirely attributable to the size-of-source effect (-6 K at 2422 K), then the error, caused by scattered light, would be approximately -2.4 K at 1500 K and -8.2 K at 2800 K. However, since the radiometer was not actually characterized with respect to the size-of-source effect, no systematic correction was applied.

Table (7-1) gives a summary of expanded uncertainty components of T_λ, as well as its (total) expanded uncertainty, at three temperatures, for each of the two radiometer output signals (high-gain-low-temperature and low-gain-high-temperature). It is important to keep in mind, that this expanded uncertainty of T_λ is rather optimistic, considering that probably significant uncertainty components were not taken into account, because of the incomplete characterization of the instrument.

Table 7-1: Uncertainty components in the measurement of radiance temperature using the microsecond-resolution radiation thermometer.

Amplifier gain		10			1		
Calibration at		2073.15 K			2373.15 K		
		Expanded uncertainties of T_λ (in K) at					
		1500 K	1800 K	2150 K	1600 K	2400 K	2800 K
Uncertainty components	uncertainty of T_0 (B)[a]	1.0	1.4	2.0	1.1	2.6	3.5
	noise and digitization of S_0 (A)[a]	0.02	0.02	0.03	0.01	0.02	0.02
	alignment during calibration (B)[a]	0.21	0.3	0.42	0.23	0.53	0.72
	noise and digitization of S (A)[a]	18	2.3	0.45	12	0.33	0.12
	mean eff. wavelength (B)[a]	1.3	0.72	0.24	1.6	0.1	1.5
	window transmittance (B)[a]	1.0	1.5	2.1	1.2	2.6	3.6
	Expanded uncertainty: $U(T_\lambda)$ =	18	3	3	12	4	5

[a] The uncertainty components may be grouped into two categories according to the method used to estimate their numerical values:

A. those which are evaluated by statistical methods,

B. those which are evaluated by other means.

7.2 Thermodynamic temperature

The uncertainty in thermodynamic temperature T was determined from the uncertainty in the radiance temperature T_λ and the uncertainty in the measured normal spectral emittance ε of the specimen. Again, using Wien's approximation to Planck's law, eq. (4.1) may be written in the simpler form:

$$\frac{1}{T} = \frac{1}{T_\lambda} + \frac{n \cdot \lambda}{c_2} \ln \varepsilon(T) \tag{7.6}$$

As outlined in §(4.1), λ should strictly be the mean effective wavelength between T_λ and T. However, the error introduced by using the m.e. wavelength between T_0 and T_λ instead, is negligible compared to the other uncertainties (see fig. 4.2).

Equation (7.6) is identical to eq. (7.1), if T is replaced by T_λ, T_λ by T_0, and ε by S_0/S. Hence, the (relative) uncertainty components of T were obtained in the same fashion

$$\frac{u_{T_\lambda}(T)}{T} = \frac{T}{T_\lambda} \cdot \frac{u(T_\lambda)}{T_\lambda} \tag{7.7}$$

$$\frac{u_\varepsilon(T)}{T} = \frac{n \cdot \lambda \cdot T}{c_2} \cdot \frac{u(\varepsilon)}{\varepsilon} \tag{7.8}$$

The component arising from the uncertainty in λ has already been taken into account in $u(T_\lambda)$.

The largest contributions to the uncertainty of the measured normal spectral emittance come from signal noise, alignment of the PSD, and specimen movement. This uncertainty was estimated from the standard deviation of the normal spectral emittance at the melting point of niobium and titanium from its mean value.

With an expanded relative uncertainty of 7% in ε, and using the expanded uncertainty in T_λ from the previous section, we obtain an expanded uncertainty in the reported melting temperatures of 25 K, in the case of niobium, and 13 K, in the case of titanium.

7.3 Resistivity

A detailed discussion of uncertainties associated with the measurement of current and voltage can be found in [60]. Specific items in the error analysis were recomputed when the present conditions differed from those in the earlier publication.

A summary of uncertainty components contributing to the expanded uncertainty of ρ_{el} is given in the following table.

Table 7-2: Uncertainty components of the measured resistivity (not corrected for thermal expansion).

Source of uncertainty	Expanded relative uncertainty component
Voltage measurement (B)	2%
Current measurement (B)	2%
Linear specimen density (B)	0.4%
Volume density (B)	0.4%
Effective specimen length (B)	1%
Expanded relative uncertainty: $U_r(\rho_{el})$ =	3%

The uncertainty in the linear density was computed from the uncertainties of the weight measurement and the measurement of the total specimen length, and was rounded upwards. According to the scale manufacturer's specifications for the range that was used, the uncertainty in the measured total weight of the specimens was 0.042% for the niobium specimens and 0.084% for the titanium specimens. The uncertainty in the measurement of the total specimen length, using the traveling microscope, was estimated at 0.15%.

The uncertainty in the reported resistivity-vs.-temperature functions was computed from the uncertainty in ρ_{el}, the uncertainty in the determination of thermodynamic temperature, and the standard deviation of the mean resistivity values from all experiments that were computed every 50 K (§4.2). A summary of the magnitudes of the various uncertainty components is given in Table (7-3).

Table 7-3: Uncertainty components of the linear functions of temperature representing the measured electrical resistivity of niobium and titanium.

		Expanded relative uncertainty components of the $\rho_{el}(T)$ functions			
		niobium		titanium	
		solid	liquid	solid	liquid
Uncertainty sources	uncertainty in ρ_{el} (B)	3%	3%	3%	3%
	uncertainty in T (B)	1.0%	0.2%	0.2%	0.1%
	uncertainty in the mean resistivity values from all experiments (A)	0.8%	0.8%	0.3%	0.2%
	Expanded relative uncertainty: $U_r[\rho_{el}(T)]$ =	3%	3%	3%	3%

7.4 Heat of fusion

The uncertainty in the computed heat of fusion was determined from the uncertainty in specific enthalpy, the uncertainty in the determination of thermodynamic temperature, and the standard deviation of the mean value from all experiments. The uncertainty in specific enthalpy was, in turn, determined from the combined uncertainties in the imparted power (product of voltage and current), the effective specimen length, and the linear density of the specimens. A summary of the magnitudes of the various uncertainty components is given in Table (7-4).

7.5 Specific heat capacity

The uncertainty in the computed specific heat capacity was determined from the uncertainty in specific enthalpy, the uncertainty in the determination of thermodynamic temperature, and the standard deviation of the mean value from all experiments at each temperature. A summary of the magnitudes of the various uncertainty components is given in Table (7-5).

Table 7-4: Uncertainty components of the computed heat of fusion of niobium and titanium.

		Expanded relative uncertainty components	
		niobium	titanium
Uncertainty sources	imparted power (B)	2.8%	2.8%
	effective specimen length (B)	1%	1%
	linear specimen density (B)	0.4%	0.4%
	temperature measurement (B)	2%	0.5%
	uncertainty in the mean value from all experiments (A)	4%	6%
	Expanded relative uncertainty: $U_r(h_F)$ =	5%	7%

Table 7-5: Uncertainty components of the computed specific heat capacity of niobium and titanium.

		Expanded relative uncertainty components					
		niobium				titanium	
		1600 K	2200 K	3200 K	liquid	solid	liquid
Uncertainty sources	specific enthalpy (B)	3%	3%	3%	3%	3%	3%
	temperature measurement (B)	6.6%	0.2%	13%	1.8%	0.22%	0.12%
	uncertainty in the mean value from all experiments (A)	2.6%	1%	4.8%	6.6%	1.4%	4%
	Expanded rel. uncertainty:	8%	3%	14%	7%	3%	5%

8 DISCUSSION AND OUTLOOK

The present work proved the applicability of the laser polarimetric technique to the measurement of thermophysical properties of metals using a microsecond-resolution pulse-heating technique. The obtained data were in reasonable agreement with data that had been obtained in the past at NIST, using both the millisecond and microsecond systems. For the first time, it was possible to measure the normal spectral emittance of the pulse-heated specimens at such speeds. This allowed the determination of their thermodynamic temperature over a wide range that, in the case of niobium, extended some five hundred degrees into the liquid phase. The technique has the potential to provide accurate thermophysical property data up to much higher temperatures. Assumptions about the behavior of the normal spectral emittance of liquid metals will no longer be necessary.

In the course of this work some interesting observations were made, concerning the dependence of the radiance temperature at the melting point of niobium on the treatment that the specimens had received prior to being pulse-heated in the microsecond system. Whereas in slower millisecond-resolution pulse-heating experiments it is well established that the melting-point radiance temperature of pure metals is highly reproducible, irrespective of the initial surface condition of the specimen, the opposite was found to be true at the higher heating rates of the microsecond system. In the case of titanium, the radiance temperature at the melting point was significantly higher than the value obtained with slower experiments. Even more importantly, its normal spectral emittance was found to decrease upon completion of the melting transition, down to a value that was approximately equal to that at the melting point of titanium when measured with the slower pulse-heating technique. This would have led to a significant error in thermodynamic temperature, had the assumption been made of a constant emittance in the liquid phase, and effectively demonstrated the advantage of an in-situ measurement of the normal spectral emittance, simultaneously with the radiance temperature measurement.

A possible explanation for these differences in melting behavior, as compared to the slower technique, could be residual roughness at the melting point and even in the first stages of the liquid phase. This raises questions about the use of a polarimeter on surfaces that are not ideally smooth. Apparently, the instrument has some tolerance to surface roughness, at least within its accuracy. Nevertheless, more work, on an experimental as well as a theoretical level, is required to understand its response to roughness.

Future work involving this microsecond-resolution pulse-heating technique will undoubtedly have to focus on alloys instead of pure metals. On one hand, thermophysical properties of industrially significant alloys in their liquid phase are of great interest in many applications related to high-temperature technologies, particularly in the casting industry. On the other hand, such measurements on complicated systems can provide important insight into the physics of high-speed melting of alloys. A study on the effect of heating rate and grain size on the melting behavior of a relatively simple binary alloy, Nb-47 mass% Ti, was recently conducted at NIST, using the slower millisecond-resolution system [61]. In this study the heating rate was varied in the range of 100 to 10000 $K \cdot s^{-1}$, and the observed melting behavior was successfully explained by a model that included diffusion in the solid coupled with a heat balance during the melting process. This model predicted that T_0 (diffusionless) melting would take place at significantly higher heating rates, at a temperature between the solidus and liquidus temperatures of the alloy. Preliminary experiments with this alloy in the microsecond system, showed that heating rates up to 10^8 $K \cdot s^{-1}$ were not high enough to achieve T_0 melting. It would be interesting to modify the capacitor-discharge circuit and/or use specimens of smaller diameter to heat the alloy even faster. Ideally, the circuit could be modified to cover a much wider range of heating rates, for instance by using inductive coils to slow it down, in order to close the gap between the slower millisecond and the faster microsecond systems.

In the case of alloys, it will also be very interesting to study the effect of composition on the normal spectral emittance. If there is such an effect, it will probably be difficult to model. However, even some sort of an empirical law might prove very helpful for the high-temperature alloy industry. The question here is, can an expression be found, reasonably accurate for industrial applications, that relates the normal spectral emittance of an alloy to that of its major constituents, via the alloy composition?

ACKNOWLEDGMENTS

Two people made it possible for me to carry out this work; my thesis advisor at the Technische Universität Graz in Austria, Dr. Gernot Pottlacher, who first mentioned the possibility of going to the United States, and the late Dr. Ared Cezairliyan who accepted to have me as a guest researcher at the Metallurgy Division of the National Institute of Standards and Technology (NIST), Gaithersburg, MD. I will always be indebted to them.

For their help and support, I would like to express my gratitude to the Division Chief and all members of the Metallurgical Processing Group of the Metallurgy Division. In particular, Dr. Debasis Basak, Mr. John McCLure, and Dr. Archie Miiller (of the Pressure and Vacuum Group of the Process Measurements Division)for their invaluable help and friendship during my years at NIST. Dr. William Boettinger and Dr. Daniel Josell, for their advice and guidance.

Dr. Shankar Krishnan of Containerless Research Inc., Evanston, IL, USA, for his support in my work with the polarimeter.

At my ‘home base’ in Graz, Austria, I would like to thank Mr. (very soon Dr.) Achim Seifter and Dr. Erhard Kaschnitz, for the many fruitful discussions.

This work was supported in part by the Microgravity Science and Applications Division of the National Air and Space Administration (NASA).

REFERENCES

[1] A. Cezairliyan, “Design and operational characteristics of a high-speed (millisecond) system for the measurement of thermophysical properties at high temperatures”, *J. Res. Nat. Bur. Stand.* **75C**:7 (1970).

[2] F. Righini, A. Rosso, and G. Ruffino, “System for fast high-temperature measurements”, *High Temp.-High Press.* **4**:597 (1972).

[3] F. Righini, J. Spišiak, and G. C. Bussolino, “Normal spectral emissivity of niobium (at 900 nm) by a pulse-heating reflectometric technique”, *Int. J. Thermophys.* **20**:1095 (1999).

[4] A. Cezairliyan, S. Krishnan, and J. L. McClure, “Simultaneous measurements of normal spectral emissivity by spectral radiometry and laser polarimetry at high temperatures in millisecond-resolution pulse-heating experiments: application to molybdenum and tungsten”, *Int. J. Thermophys.* **17**:1455 (1996).

[5] F. E. Nicodemus (editor), “Self-study manual on optical radiation measurements”, *NBS Technical Note 910-1* (1976), Chapters 1-3.

[6] H. Preston-Thomas, “The International Temperature Scale of 1990 (ITS-90)”, *Metrologia* **27**:3 (1990), **27**:107 (1990).

[7] F. E. Nicodemus (editor), “Self-study manual on optical radiation measurements”, *NBS Technical Note 910-2* (1976), Chapters 4-5.

[8] D. P. DeWitt and G. D. Nutter (editors), *Theory and practice of radiation thermometry* (Wiley, 1988), Chapter 4.

[9] H. J. Kostkowski and R. D. Lee, “Theory and Methods of Optical Pyrometry”, in *Temperature, Its Measurement and Control in Science and Industry* (Reinhold Publishing Co., 1962), Vol 3, Part 1, p. 449.

[10] F. Righini, F. Rosso, and G. Ruffino, “Temperature dependence of effective wavelength in optical pyrometry”, in *Temperature, Its Measurement and Control in Science and Industry* (Instrument Society of America, 1972), Vol 4, Part 1, p. 413.

[11] R. M. A. Azzam and N. M. Bashara, *Ellipsometry and polarized light* (North Holland, 1977), Chapter 1.

[12] M. Born and E. Wolf, *Principles of Optics* (Pergamon Press, 1975), Chapter 10.

[13] D. S. Kliger, J. W. Lewis, and C. E. Randall, *Polarized light in optics and spectroscopy* (Academic Press, 1990), Chapter 4.

[14] R. M. A. Azzam and N. M. Bashara, *Ellipsometry and polarized light* (North Holland, 1977), Chapter 2.

[15] M. Born and E. Wolf, *Principles of Optics* (Pergamon Press, 1975), Chapter 13.

[16] R. M. A. Azzam and N. M. Bashara, *Ellipsometry and polarized light* (North Holland, 1977), Chapter 4.

[17] M. Born and E. Wolf, *Principles of Optics* (Pergamon Press, 1975), Chapter 1.

[18] F. W. Grover, *Inductance calculations working formulas and tables* (Dover, 1946), Chapters 5 and 16.

[19] R. Gallob, "Bestimmung thermophysikalischer Daten von flüssigem Niob bis in den Überhitzungsbereich", Dissertation, Technische Universität Graz (1982).

[20] C. E. Gibson, B. K. Tsai, and A. C. Parr, "Radiance temperature calibrations", *NIST Special Publication 250-43* (1998).

[21] W. R. Waters, J. H. Walker, and A. T. Hattenburg, "Radiance temperature calibrations", *NIST Special Publication 250-7* (1987), Appendix C.

[22] A. Cezairliyan, G. M. Foley, M. S. Morse, and A. P. Miiller, "Six-wavelength millisecond-resolution pyrometer", in *Temperature, Its Measurement and Control in Science and Industry* (Am. Inst. of Physics, 1992), Vol 6, Part 2, p. 757.

[23] F. E. Nicodemus (editor), "Self-study manual on optical radiation measurements", *NBS Technical Note 910-4* (1976), Chapter 7.

[24] Operator's manual, Jarell-Ash Monospec 27 Monochromator/Spectrograph (1985).

[25] R. M. A. Azzam, "Division-of-amplitude photopolarimeter (DOAP) for the simultaneous measurement of all four Stokes parameters of light", *Opt. Acta* **29**:685 (1982).

[26] S. Krishnan, “Apparatus for spectral emissivity measurements on pulse-heated materials”, Dep. of Commerce SBIR Phase II Final Report (1998).

[27] R. M. A. Azzam and N. M. Bashara, *Ellipsometry and polarized light* (North Holland, 1977), Appendix.

[28] S. Krishnan and P. C. Nordine, “Mueller-matrix ellipsometry using the division-of-amplitude photopolarimeter: a study of depolarization effects”, *Appl. Opt.* **33**:4184 (1994).

[29] S. Krishnan, “Mueller-matrix ellipsometry on electroformed rough surfaces”, *J. Mod. Opt.* **42**:1695 (1995).

[30] R. M. A. Azzam and A. G. Lopez, “Accurate calibration of the four-detector photopolarimeter with imperfect polarizing optical elements”, *J. Opt. Soc. Am A* **6**:1513 (1989).

[31] R. M. A. Azzam, “Stationary property of normal-incidence reflection from isotropic surfaces”, *J. Opt. Soc. Am A* **72**:1187 (1982).

[32] R. M. A. Azzam, E. Masetti, I. M. Elminyawi, and F. G. Grosz, “Construction, calibration, and testing of a four-detector photopolarimeter”, *Rev. Sci. Instr.* **59**:84 (1988).

[33] R. M. A. Azzam, “Instrument matrix of the four-detector photopolarimeter: physical meaning of its rows and columns and constraints on its elements”, *J. Opt. Soc. Am A* **7**:87 (1990).

[34] R. M. A. Azzam, “Measurement of the Stokes parameters of light: A unified analysis of Fourier photopolarimetry”, *Optik* **52**:253 (1979).

[35] S. Krishnan, “Calibration, properties, and applications of the division-of-amplitude photopolarimeter at 632.8 and 1523 nm”, *J. Opt. Soc. Am A* **9**:1615 (1992).

[36] E. Kaschnitz, “Bestimmung thermophysikalischer Daten verschiedener Metalle bei ohmscher Pulsaufheizung im Mikrosekundenbereich”, Dissertation, Technische Universität Graz (1992).

[37] K. C. Mills, B. J. Monaghan, and B. J. Keene, "Thermal conductivities of molten metals, Part 1: Pure Metals", NPL Report CMMT(A) 53.

[38] T. Matsumoto and A. Cezairliyan, "A combined transient and brief steady-state technique for measuring hemispherical total emissivity of electrical conductors at high temperatures: application to tantalum", *Int. J. Thermophys.* **18**:1539 (1997).

[39] A. Cezairliyan and A. P. Miiller, "Radiance temperatures (in the wavelength range 522-906 nm) of niobium at its melting point by a pulse-heating technique", *Int. J. Thermophys.* **13**:39 (1992).

[40] A. Cezairliyan and A. P. Miiller, "Thermodynamic study of the α→β phase transformation in titanium by a pulse heating method", *J. Res. Nat. Bur. Stand.* **83**:127 (1978).

[41] A. Cezairliyan, A. P. Miiller, F. Righini, and A. Rosso, "Radiance temperature of metals at their melting points as possible high temperature secondary reference points", in *Temperature, Its Measurement and Control in Science and Industry* (Am. Inst. of Physics, 1982), Vol 5, Part 2, p. 377.

[42] A. Cezairliyan, A. P. Miiller, F. Righini, and A. Rosso, "Radiance temperature and normal spectral emissivity of metals at their melting point as possible reference values", in *Temperature, Its Measurement and Control in Science and Industry* (Am. Inst. of Physics, 1992), Vol 6, Part 1, p. 377.

[43] A. Cezairliyan and F. Righini, "Issues in high-speed pyrometry", *Metrologia* **33**:299 (1996).

[44] M. G. Natrella, "Experimental statistics", *NBS Handbook 91* (reprint of 1966), Chapter 3.

[45] D. P. DeWitt and G. D. Nutter (editors), *Theory and practice of radiation thermometry* (Wiley, 1988), Chapter 18.

[46] A. Cezairliyan, "Measurement of melting point, normal spectral emittance (at melting point), and electrical resistivity (above 2650 K) of niobium by a pulse heating method", *High Temp.-High Press.* **4**:453 (1972).

[47] A. P. Miiller and A. Cezairliyan, “Thermal expansion of niobium in the range 1500-2700 K by a transient interferometric technique”, *Int. J. Thermophys.* **9**:195 (1988).

[48] A. Cezairliyan, “High-speed (subsecond) measurement of heat capacity, electrical resistivity, and thermal radiation properties of niobium in the range 1500 to 2700 K”, *J. Res. Nat. Bur. Stand.* **75A**:565 (1971).

[49] A. Cezairliyan and J. L. McClure, “Heat capacity and electrical resistivity of liquid niobium near its melting temperature”, *Int. J. Thermophys.* **8**:803 (1987).

[50] A. Cezairliyan and A. P. Miiller, “A transient (subsecond) technique for measuring heat of fusion of metals”, *Int. J. Thermophys.* **1**:195 (1980).

[51] A. Cezairliyan and J. L. McClure, “A microsecond-resolution transient technique for measuring the heat of fusion of metals: niobium”, *Int. J. Thermophys.* **8**:577 (1987).

[52] A. Seifter, “Bestimmung des normalen spektralen Emissionskoeffizienten von flüssigen pulsgeheizten Metallen mittels eines schnellen Photopolarimeters”, Dissertation, Technische Universität Graz (2001).

[53] F. Righini, A. Rosso, L. Coslovi, A. Cezairliyan, and J. L. McClure, “Radiance temperature of titanium at its melting point”, *Proceedings of the 7th Symposium on Thermophysical Properties* (1977).

[54] A. Cezairliyan and A. P. Miiller, “Melting point, normal spectral emittance (at the melting point), and electrical resistivity (above 1900 K) of titanium by a pulse heating method”, *J. Res. Nat. Bur. Stand.* **82**:119 (1977).

[55] U. Seydel, W. Fucke, and H. Wadle, *Die Bestimmung thermophysikalischer Daten flüssiger hochschmelzender Metalle mit schnellen Pulsaufheizexperimenten* (Verlag Dr. Peter Mannhold, 1980).

[56] A. Cezairliyan and A. P. Miiller, “Heat capacity and electric resistivity of titanium in the range 1500 to 1900 K by a pulse heating method”, *High Temp.-High Press.* **9**:319 (1977).

[57] J. L. McClure and A. Cezairliyan, “Measurement of the heat of fusion of titanium and a titanium alloy (90Ti-6Al-4V) by a microsecond-resolution transient technique”, *Int. J. Thermophys.* **13**:75 (1992).

[58] ISO, *Guide to the expression of uncertainty in measurement* (International Organization for Standardization, 1993).

[59] B. N. Taylor and C. E. Kuyatt, “Guidelines for evaluating and expressing the uncertainty of NIST measurement results”, *NIST Technical Note 1297* (1994).

[60] J. L. McClure and A. Cezairliyan, “Microsecond-resolution electrical measurements in high-current discharges”, *Int. J. Thermophys.* **11**:739 (1990).

[61] D. Basak, W. J. Boettinger, D. Josell, S. R. Coriell, J. L. McClure, S. Krishnan, and A. Cezairliyan, “Effect of heating rate and grain size on the melting behavior of the alloy Nb-47 mass% Ti in pulse-heating experiments”, *Acta mater.* **47**:3147 (1999).